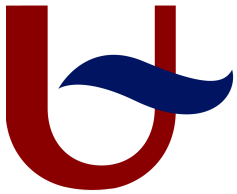

UNIVERSITEIT ANTWERPEN
Faculteit Wetenschappen
Departement Fysica

Dynamica van Wisselwerkinde Clusters in Laag-dimensionale Supergeleiders

---

Dynamics of Interacting Clusters in Low-dimensional Superconductors

Proefschrift voorgelegd tot het behalen van de graad van
doctor in de wetenschappen
aan de Universiteit Antwerpen te verdedigen door

Nansheng Lin

Promotoren: Dr. Vyacheslav R. Misko
Prof. dr. François M. Peeters

Antwerpen
Nov. 2012

Members of the Jury:
Chairman
Prof. dr. A. Bogaerts

Secretary
Prof. dr. J. Tempère

Promoters
Dr. V. R. Misko
Prof. dr. F. M. Peeters

Other Members
Prof. dr. D. Lamoen
Prof. dr. A. V. Silhanek (Université de Liège)
Prof. dr. W. V. Pogosov (Russian Academy of Sciences)

ABSTRACT

The last decade has been marked by fast development of the nanotechnology, and, as a result, devices reached mesoscopic and nanoscale size. Low-dimensional devices and materials have attracted a considerable interest. New properties of low-dimensional nanostructure materials are revealed and these materials can be used as fundamental building blocks for nano-scale science and technology, ranging from chemical and biological sensors, field effect transistors to logic circuits [1].

Meanwhile, superconductivity has been revealed for a hundred years and some applications, such as Maglev (magnetic levitation) train in Japan, have been developed. Considering the zero electronic resistance in superconductors, it is a smart way to avoid energy waste by using superconductors instead of metal wires, specially at room temperature if possible. In the Bardeen-Cooper–Schrieffer (BCS) theory (which has well explained the mechanism of conventional superconductors in microscopy), there are attracting electron pairs (called Cooper pairs). The Cooper pairs are condensed in the ground state, reduce the system energy, and thus result in superconductivity. As well known, most of superconductors with high critical magnetic field are type-II superconductors, *i. e.*, the vortex state can be found during the transition of superconductors from the superconducting state to the normal state. The energy dissipation due to the movement of vortices will limit the application of type-II superconductors. These are good motivations to investigate the dynamics of single vortices and their clusters, particularly in low-dimensional system. We have studied the dynamics of vortices in mesoscopic superconducting Corbino disks (Chapter 3) and circular Rachet channels (Chapter 4), and we also use the electron-hole symmetry to study the clusters of Cooper pairs in ultra small superconducting grains (Chapter 5).

The structure of this thesis is as follows. First, an introduction to superconductivity and backgrounds of different systems such as “Corbino disks" are given. Then, we will discuss the details of numerical simulations in Chapter 2.

In Chapter 3, we will present the study of the dynamics of vortex shells in mesoscopic superconducting Corbino disks, where

vortex clusters consisting of concentric vortex shells were recently observed in micrometer-sized Nb disks. In such a system, there is a competition among the vortex-vortex interaction, the gradient Lorentz force and the (in)commensurability between the numbers of vortices in shells. The dynamical process becomes complex and different scenarios of angular melting of vortex-shells have been observed. It can start either from the center of the disk (where the shear stress is maximum) or from its boundary (where the shear stress is minimum) depending on the specific vortex configuration. Furthermore, we found that two kinds of defects can exist in such vortex-shell structures: intrashell and intershell defects. An intrashell defect may lead to an inverse dynamic behavior, *i.e.*, one of the vortex shells under a stronger driving force can rotate slower than the adjacent shell that is driven by a weaker Lorentz force. An intershell defect always locks more than two shells until the gradient of the Lorentz force becomes strong enough to break the rigid-body rotation of the locked shells. Such a lock-unlock process leads to hysteresis in the angular velocities of the shells.

An asymmetric potential may rectify the motion of particles (*e.g.*, vortices) and induce a net flow without any unbiased external drive, which is called “ratchet effect". In Chapter 4, we will study the motion of vortices in a circular ratchet channel. First, we will show that the net flow of vortices strongly depends on vortex density and frequency of the driving current. Depending on the density, we distinguish a “single-vortex" rectification regime (for low density, when each vortex is rectified individually) determined by the potential-energy landscape inside each cell of the channel (*i.e.*, “hard" and “easy" directions) and “multi-vortex," or “collective," rectification (high-density case) when the inter-vortex interaction becomes important. Then, we analyze the average angular velocity ω of vortices as a function of the current I and study commensurability effects between the numbers of vortices and cells in the channel and the role of frequency of the applied ac current. We have shown that the commensurability effect results in a stepwise $\omega - I$ curve. Besides the “integer" steps, *i.e.*, the large steps found in the single-vortex case, we also found “fractional" steps corresponding to fractional ratios between the numbers of vortices and triangular cells. Also, the result of preliminary measurements on a device containing a single weak-pinning circular ratchet channel in a Corbino geometry will be discussed and a substantial asymmetric vortex response has been observed.

In Chapter 5, we will analyze the electron-hole symmetry of the BCS Hamiltonian for the case of an equally-spaced model and suggest a general analytical expression of the ground state energy for the arbitrary number of pairs and interaction constant. In order to explore the applicability range of our result, we numerically solve Richardson equations, which provide an exact solution of the problem. Comparing with the exact numerical solution, a high accuracy of our expression is demonstrated, while the usual grand canonical BCS approach fails in fluctuation-dominated regime.

ABSTRACT (NL)

Het laatste decennium wordt gekenmerkt door een snelle ontwikkeling van de nanotechnologie en bijgevolg hebben allerlei systemen een mesoscopische of nanoscopische schaal bereikt. Laagdimensionale systemen en materialen hebben veel aandacht getrokken. Nieuwe eigenschappen van laagdimensionale nanostructuren werden onthuld en deze materialen kunnen gebruikt worden als basisstructuren voor wetenschap en technologie op nanoschaal van chemische en biologische sensoren tot veld-effect-transistoren en logische circuits.

Ondertussen werd supergeleiding al honderd jaar geleden ontdekt en werden er al enkele toepassingen ontwikkeld, zoals een Maglev- (magnetische levitatie) trein in Japan. Door de afwezigheid van elektrische weerstand in supergeleiders, lijkt het een slimme manier om energieverlies tegen te gaan door supergeleiders te gebruiken i.p.v. metalen draden, indien mogelijk bij kamertemperatuur. In de Bardeen-Cooper-Schrieffer (BCS) theorie (die een goede verklaring geeft voor het microscopisch mechanisme van conventionele supergeleiders), zijn er aantrekkende elektronenparen (Cooper-paren genaamd). The Cooper-paren zijn gecondenseerd in de grondtoestand, verminderen de energie van het systeem, en resulteren bijgevolg in supergeleiding. Zoals welbekend zijn de meeste supergeleiders met hoge kritische magnetische velden type-II supergeleiders. De energiedissipatie door het bewegen van vortices begrenst de toepassing van type-II supergeleiders. Dit vormt een goede motivatie om de dynamica te bestuderen van enkele vortices en hun clusters, vooral in laagdimensionale systemen. We hebben de dynamica bestudeerd van vortices in mesoscopische supergeleidende Corbino-schijven (hoofdstuk 3) en cirkelvormige ratchet-kanalen (hoofdstuk 4), en we gebruiken ook de elektron-gaten-symmetrie om clusters van Cooper-paren te onderzoeken in ultrakleine supergeleidende korrels (hoofdstuk 5).

De structuur van deze thesis is als volgt. Eerst wordt er een inleiding gegeven over supergeleiding en de achtergrond van verschillende systemen zoals “Corbino-schijven". Dan bespreken we de details van de numerieke simulaties in hoofdstuk 2. In hoofdstuk 3 presenteren we de studie van de dynamica van vortexschillen in

mesoscopische supergeleidende Corbino-schijven, waar vortexclusters bestaande uit concentrische vortexschillen recent geobserveerd werden in Nb schijven met micrometer grootte. In zo'n systeem is er een competitie tussen vortex-vortex-interactie, de Lorentz-kracht en de (in)commensurabiliteit tussen de aantallen vortices in de schillen. Het dynamische proces wordt complex en verschillende scenarios van angulair smelten van de vortexshillen werden waargenomen. Het kan zowel vanuit het centrum van de schijf (waar de schuifspanning het grootst is) als vanaf de rand (waar de schuifspanning minimaal is) starten, afhankelijk van de specifieke vortexconfiguratie. Bovendien vonden we dat er twee soorten defecten kunnen bestaan in zulke vortexschilstructuren. Een intraschil defect kan leiden tot een omgekeerd dynamisch karakter, t.t.z. een van de vortexschillen die onder een sterkere aandrijfkracht staat, kan trager roteren dan een naburige schil die wordt gedreven door een kleinere Lorentzkracht. Een interschil defect blokkeert altijd meer dan twee schillen totdat de Lorentz-kracht sterk genoeg wordt om de rigide rotatie van de geblokkeerde schillen te breken. Zo'n blokkeerproces leidt tot hysteresis in de angulaire snelheid van de schillen.

Een asymmetrische potentiaal kan de beweging van deeltjes (zoals vortices) gelijkrichten en een netto stroom veroorzaken zonder enige externe spanning, wat het "ratchet-effect" genoemd wordt. In hoofdstuk 4 bestuderen we de beweging van vortices in een circulair ratchet-kanaal. Eerst tonen we aan dat de netto stroom van vortices afhangt van de vortexdichtheid en de frequentie van de aandrijfstroom. Afhankelijk van de dichtheid onderscheiden we het "enkele vortex" rectificatieregime (voor lage dichtheid, wanneer elke vortex individueel gerectificeerd wordt) dat bepaald wordt door het potentiaal/energie-landschap in elke cel van het kanaal (dus "moeilijke" en "gemakkelijke" richtingen), en een ąřmultivortexąś of ąřcollectieveąś rectificatie (in het geval van hoge dichtheden) wanneer de intervortexinteractie belangrijk wordt. Dan analyseren we de gemiddelde angulaire snelheid ω van de vortices als functie van de stroom I en bestuderen we de commensurabiliteitseffecten tussen de aantallen vortices en cellen in het kanaal en de frequentie van de aangelegde ac spanning. We hebben aangetoond dat het commensurabiliteitseffect resulteert in een stapsgewijze $\omega - I$ curve. Naast de "gehele" stappen, t.t.z. de grote stappen die gevonden worden in het geval van enkele vortices, vonden we ook "fractionele" stappen, corresponderend met de fractionele verhoudingen tussen het aantal vortices en de triangulaire cellen. We bespreken ook het resultaat van een voorlopige meting aan een sample dat één

enkel zwak-gepind circulair ratchet-kanaal bevat in een Corbino-geometrie waarbij een substantiële asymmetrische vortexrespons waargenomen werd.

In hoofdstuk 5 analyseren we de elektron-gatensymmetrie van de BCS-Hamiltoniaan voor het geval van een gelijk gevormd model en suggereren een algemene analytische oplossing voor de grond-toestandsenergie voor een willekeurig aantal paren en interactieconstanten. Om de toepasbaarheid van ons resultaat te onderzoeken, lossen we numeriek Richardson-vergelijkingen op die een exacte oplossing van het probleem opleveren. Vergeleken met de volledige numerieke oplossing van de Richardson-vergelijkingen, werd een hoge nauwkeurigheid van onze uitdrukking aangetoond, terwijl de standaard groot-canonische BCS-benadering faalt in het regime waar fluctuaties domineren.

“大学之道，在明明德，在新民，在止于至善。”
”The Way of the Great Learning involves manifesting virtue, renewing the people, and resting in supreme goodness.”
格物、致知、诚意、正心、修身、齐家、治国、平天下。

—-《礼记 • 大学》

ACKNOWLEDGMENTS

Because of the supports and encouragements from many people, I can reach the step to present the work in this thesis. It is time to thank them who helped me, guided me and encouraged me.

Foremost, I wish to express my sincere gratitude to my promoters Dr. Vyacheslav Misko and Prof. Francois Peeters. They have provided me an opportunity to study on interesting research topics and their guidance, motivation and support have been essential for my works.

Besides my promoters, I would like to thank the rest of the professors (Prof. J. Tempère, Prof. D. Lamoen *etc*) who have taught me and laid the foundations for my PhD research. My special thanks to the people I collaborated with, particularly, Prof. W. V. Pogosov for his guidance and discussions. Also I would like to acknowledgement the rest of my thesis committee: Prof. A. Bogaerts and Prof. A. V. Silhanek, for their encouragement and insightful comments, which have been helpful.

Many thanks to all my colleagues in the CMT group. Particular thanks to my (pre-)office mates: Azamat, Dorberk, Mohammad, Davoud and Natalia. Also a big thank to Roeland and Ortwin for helping me a lot.

非常感谢在比利时的老师和朋友们陪我度过了难忘的国外生活。感谢安大的张老师和陶医生，感谢物理系和安特的朋友们：贲哥、姗姗、周志辉、张亮、小麦、海军、老谭、李斌晓丹夫妇、亚江海燕夫妇、老王、番茄、卢博杜阳夫妇、田博张宇夫妇、刘超宇、梁灵智、张凌峰、石慧、凌云、林枫祥艳夫妇、梅春萍、王晨、廖金宝、老吕、朱灿、李凯、老何、赵淑霞、颜元、李爽、杨智、唐正夫妇、管章华、周城、潘菊富、马成、郭佳等，是你们让我的生活变得丰富精彩！

还要特别感谢女友马敏，感谢你一直以来陪伴左右关心照顾和鼓励我，让我在他乡有个温馨的家。感谢我弟南章对我的鼓励和对家里的付出。最后，无法言谢的，是我父母辛勤劳作，一直以来为我默默的付出，你们成为我求学之路最坚实的后盾。

Nansheng Lin
Antwerpen, 2012

CONTENTS

1

INTRODUCTION TO SUPERCONDUCTIVITY

1.1 HISTORY OF SUPERCONDUCTIVITY

In 1911, H. Kamerlingh Onnes discovered that the resistivity of the mercury (Hg) drops abruptly to zero when temperature decreases to 4.2K. Later, similar property has been obtained with other material elements and alloys. The phenomenon of exactly zero electrical resistance is called superconductivity. The temperature T_c when a superconductor transits from the normal state to the superconducting state, *e.g.*, $T_c = 4.2K$ for Hg, is named "critical temperature". Besides a zero electrical resistance, another important property has been obtained by W. Meissner and R. Ochsenfeld in 1933. The magnetic field is expelled from a superconductor when it is placed in a weak external magnetic field H below T_c, which is known as Meissner effect. Several theories has been developed in the last century. In 1935, F. and H. London developed a phenomenological theory (called London theory) and showed that the minimization of the electromagnetic free energy carried by superconducting current could lead to the Meissner effect. Another phenomenological theory of superconductivity, *i.e.*, Ginzburg-Landau theory, was devised by Landau and Ginzburg in 1950. They combined the theory of second-order phase transitions with a Schrödinger-like wave equation in their theory and had great success in explaining the macroscopic properties of superconductors. In 1957, Abrikosov predicted the division of superconductors into the two groups, *i.e.*, Type I and Type II superconductors, by applying Ginzburg-Landau theory. The properties of conventional superconductors were modeled successfully in microscopic by John Bardeen, Leon Cooper, and Robert Schrieffer, whose theory is commonly called the BCS theory. However, a new generation of superconductors (oxide based ceramic materials) has been discovered in 1986. Then a cuprate superconductor functioning above 77K, *i.e.*, boiling point

Heike Kamerlingh Onnes was the Nobel Prize winner in 1913.

Abrikosov and Ginzburg were awarded the Nobel Prize in 2003.

John Bardeen, Leon Cooper, and Robert Schrieffer won the Nobel Prize in 1972.

of liquid nitrogen, has been found in early 1997. The new superconductors *i. e.*, high-T_c superconductors, cannot be well explained by BCS theory. Besides the high-T_c copper-oxides, an iron-based family of high-T_c superconductors was also discovered in 2008. The theory of superconductor in high-T_c superconductors is one of the most outstanding challenges in physics.

Superconductors have many unique properties. Two important properties are zero electrical resistance to direct current (DC) and the Meissner effect (completely expel magnetic field). Superconductors have a major impact on electronic power transmission based on zero resistance and the high sensitivity of superconductors to magnetic field provides a unique sensing capability, in many cases much better than conventional measurement technology.

1.2 THEORIES OF SUPERCONDUCTIVITY

1.2.1 *London theory*

Since the discovery of superconductivity, physicists have devoted great efforts to understanding of superconductivity. London theory is the first phenomenological theory of superconductivity. As mentioned above, the Meissner effect is one of the most important properties of superconductors. The remarkable result of the London theory is its ability to explain the Meissner effect. Before describing the London theory, we first discuss the Meissner effect, which is the crucial difference between perfect conductivity (*i. e.*, conductors with zero resistance) and superconductivity. In a type-I superconductor, the magnetic field will be completely zero inside superconductor no matter whether the magnetic field is applied before or after the transition from normal state to superconductor state. However, the magnetic field inside a perfect conductor depends on the original field before the transition. In the London theory, we have

$$\frac{\partial}{\partial t}\mathbf{j_s} = \frac{1}{\mu_0 \lambda_L^2}\mathbf{E} \tag{1.1}$$

$$\nabla \times \mathbf{j_s} = -\frac{1}{\mu_0 \lambda_L^2}\mathbf{B}, \tag{1.2}$$

with the magnetic field penetration depth

$$\lambda_L = \sqrt{\frac{m}{\mu_0 n_s e^2}}, \tag{1.3}$$

where j_s is the superconducting current density, E and B are respectively the electric and magnetic fields within the superconductor, e is the charge of an electron or proton, m is electron mass, and n_s is the density of superconducting electrons. The order of λ_L is $\sim 10^{-8}$ meter in conventional superconductors and $\sim 10^{-7}$ meter in high-T_c superconductors [2]. Eq. 1.1 shows the zero resistance property of superconductors and Eq. 1.2 describes the Meissner effect. Combining with the Maxwell equations,

$$\begin{cases} \nabla \cdot \mathbf{E} &= \frac{\rho}{\varepsilon_0} \\ \nabla \cdot \mathbf{B} &= 0 \\ \nabla \times \mathbf{E} &= -\frac{\partial \mathbf{B}}{\partial t} \\ \nabla \times \mathbf{B} &= \mu_0 \mathbf{j} + \mu_0 \varepsilon_0 \frac{\partial \mathbf{E}}{\partial t} \end{cases} \tag{1.4}$$

we can obtain the equation for $\mathbf{B}$:

$$\nabla^2 \mathbf{B} = \frac{1}{\lambda_L^2} \mathbf{B}. \tag{1.5}$$

The London theory successfully describes a descending magnetic field from the surface of superconductors (in the characterized length λ_L) and also predicts the skin effect in superconductors. However, it always results in a negative energy of superconducting-normal interfaces, *i. e.*, making an interface will release energy due to the negative interface energy. Therefore, a superconductor always tends to produce interfaces as large as possible, which is not true in experiments. The reason is that Eq. 1.2 only gives a localized relationship between current density $\mathbf{j}$ and vector potential $\mathbf{A}$ ($\nabla \times \mathbf{A} = \mathbf{B}$), *i. e.*, the potential $\mathbf{A}(\mathbf{r})$ in a position $\mathbf{r}$ is only linearly dependent on $\mathbf{j}(\mathbf{r})$ in that position. Therefore, the London theory is only applicable in a relatively weak magnetic field $H \ll H_c$, where $\mathbf{j}$ and $\mathbf{A}$ perform an approximately linear behavior.

Skin effect is the tendency of an electric current to become distributed within a conductor such that the current density is largest close to the surface of the conductor, and decreases inside.

1.2.2 *Ginzburg-Landau (G-L) theory*

Landau proposed a theory of the second-order phase transition and introduced an order parameter Ψ in 1937 [3, 4, 5],

$\Psi^2 = n_s^* = n_s/2$, *where* n_s^* *is the density of Cooper pairs.*

$$F_s(0) = F_n(0) + \alpha|\Psi|^2 + \frac{\beta}{2}|\Psi|^4. \tag{1.6}$$

Here, $F_s(0)$ and $F_n(0)$ are the density of the free energy of superconducting and normal states at zero magnetic field, respectively. In the Landau theory, the order parameter Ψ is constant in a superconductor no matter how the geometry of the superconductor changes. In 1950, Ginzburg and Landau constructed an advanced theory [6] where Ψ is a space function $\Psi(\mathbf{r})$, *i. e.*, the order parameter varies in space. Thus, a term of the free energy due to the space variation of the order parameter,

$$\frac{1}{2m^*}|-i\hbar\boldsymbol{\nabla}\Psi|^2, \tag{1.7}$$

is added to Eq. 1.6. Considering an external magnetic field, we can rewrite term 1.7 by

Experimental data turned out to be fitted better if $e^* \approx 2e$, and the microscopic pairing theory of superconductivity (see Sec. 1.2.3) makes it unambiguous that $e^* = 2e$ and $m^* = 2m$ exactly.

$$\frac{1}{2m^*}\left|\left(-i\hbar\boldsymbol{\nabla} - \frac{e^*}{c}\mathbf{A}\right)\Psi\right|^2. \tag{1.8}$$

Therefore, the density of the free energy in a superconductor is

$$F_s = F_n(0) + \alpha|\Psi|^2 + \frac{\beta}{2}|\Psi|^4 + \frac{1}{2m^*}\left|-(i\hbar\boldsymbol{\nabla} + \frac{e^*}{c}\mathbf{A})\Psi\right|^2 + \frac{\mathbf{h}^2}{8\pi}, \tag{1.9}$$

where $\mathbf{h} = \boldsymbol{\nabla}\times\mathbf{A}$ is the internal magnetic field of the superconductor, and the free energy of a superconductor is

$$\mathfrak{F}_s = \int_v F_s\, d^3x. \tag{1.10}$$

1.2.2.1 *G-L equations*

Obviously, F_s is a functional of A and Ψ (see Eq. 1.10). In order to minimize the free energy F_s, the variational condition results in two equations as follows:

$$\frac{1}{2m^*}\left(-i\hbar\boldsymbol{\nabla} - \frac{e^*}{c}\mathbf{A}\right)^2\Psi + \alpha\Psi + \beta|\Psi|^2\Psi = 0, \tag{1.11}$$

$$\frac{e^*\hbar}{2m^*i}(\Psi^*\boldsymbol{\nabla}\Psi - \Psi\boldsymbol{\nabla}\Psi^*) - \frac{e^{*2}}{m^*c}|\Psi|^2\mathbf{A} = \mathbf{j}_s, \tag{1.12}$$

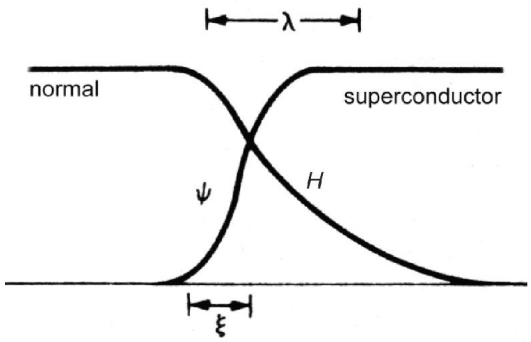

Figure 1.1: The spatial distribution of the order parameter ψ and the magnetic field H at the superconducting/normal surface boundary (Ref. [7]).

with the boundary condition

$$\mathbf{n} \cdot \left(-i\hbar\boldsymbol{\nabla} - \frac{e^*}{c}\mathbf{A} \right) \Psi = 0. \tag{1.13}$$

The boundary condition Eq. 1.13 is appropriate at an insulating surface [7].

Here $\mathbf{j_s}$ is the density of the superconcucting current and $\mathbf{n}$ is the unit vector normal to the interface. The nonlinear differential Eq. 1.11 and Eq. 1.12 are named Ginzburg-Landau (G-L) equations. In principle, we can find the values of Ψ and A in a superconductor with varying magnetic field by solving G-L equations and Maxwell equations. However, there are only a few situations where the G-L equations are analytically solved.

1.2.2.2 *G-L Parameter*

In the G-L theory, the order parameter Ψ and the internal magnetic field h both depend on coordinate. The coherence length ξ and the magnetic field penetration depth λ can be derived from the G-L equations 1.11 and 1.12 in the homogeneous case [7]:

$$\xi = \frac{\hbar}{\sqrt{2m^*\alpha}}, \tag{1.14}$$

$$\lambda = \sqrt{\frac{m^*}{\mu_0 n_s^* (e^*)^2}}, \tag{1.15}$$

Note: $n_s^* = |\Psi|^2$. In the weak magnetic field limit ($H \ll H_c$), $n_s^* \simeq n_{s0}$ and λ is the same as the result of the London theory λ_L, so it is also named "London penetration depth".

which characterize the variations of Ψ and $\mathbf{H}$, respectively (see

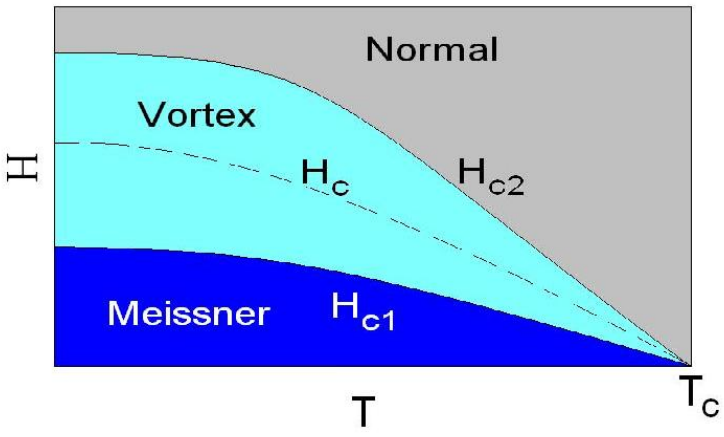

Figure 1.2: The phase diagram of a type-II superconductor.

Fig. 1.1). An important parameter, called G-L parameter, is defined as a ratio of the two characteristic lengths:

$$\kappa = \frac{\lambda}{\xi}. \tag{1.16}$$

If $\kappa < \frac{1}{\sqrt{2}}$ (type-I superconductor), the energy of the interface $\sigma_{ns} > 0$, *i.e.*, the system tends to minimize the normal-superconducting interface; if $\kappa > \frac{1}{\sqrt{2}}$ (type-II superconductor), the energy of the interface $\sigma_{ns} < 0$, *i.e.*, the system tends to maximize the normal-superconducting interface. Therefore, two types of superconductors are distinguished by κ. A type-I superconductor can be either in the normal state or the superconducting state, *i.e.*, the Meissner state. Abrikosov investigated the effect of a large Ginzburg-Landau (GL) parameter κ in the GL theory in 1957 [8]. He found a completely different magnetic-field behavior for materials with $\kappa > 1/\sqrt{2}$, *i.e.*, type-II superconductors. A Meissner phase is also present in these materials below a certain lower critical field H_{c1}. However, instead of a discontinuous transition to the normal state, at H_{c1} the magnetic flux starts to penetrate in the form of flux tubes surrounded by screening currents, which is called vortex state (see. Fig. 1.2). The superconductor becomes normal after the magnetic field reaching a higher critical value H_{c2}. Therefore, a type-II superconductor normally has a larger critical value of the magnetic field (H_{c2}) than a type-I superconductor (*e.g.*, see Fig. 1.3).

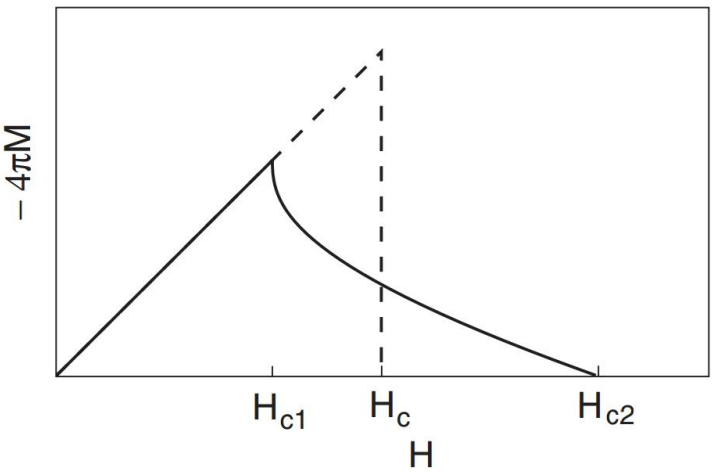

Figure 1.3: The magnetization of type-I (dashed line) and type-II (full line) superconductors.

1.2.3 *BCS theory*

Previous section presents the GL theory, which originated in 1950. Although it is a phenomenological theory, it has been successful to explain many of the principal properties of superconductors. However, it still has limitations because it does not explain the microscopic origins of superconductivity. In 1957 Bardeen, Cooper, and Schrieffer (BCS) proposed a microscopic theory of superconductivity [9] that predicts quantitatively many of the properties of elemental superconductors. In 1959, the GL equations have been derived from the BCS theory by Gor'kov [10].

Now let us present the general ideas and methods of the microscopic theory of superconductivity (*i. e.*, the BCS theory). The main point of this theory is the formation of bound states or pairs of electrons due to their interaction. However, in normal conditions, electron-electron interaction is repulsive (*i. e.*, the Coulomb interaction). How to create a bound states of electrons? Obviously, to create a bound state the interaction must be attractive, which lead us to the problem of the origin of such an attraction.

In 1956, before the publication of the BCS theory, Cooper [11] demonstrated that the normal ground state of an electron gas is unstable with respect to the formation of bound electron pairs in the Fermi sea. Cooper supposed that a weak attractive interaction exists between the electrons, and showed that an arbitrarily small

attraction between electrons in a metal can cause a paired state of electrons to have a lower energy than the Fermi energy (E_F), *i.e.*, the pair of electrons is bound. In conventional superconductors, this attraction is due to the electron-phonon interaction. In the BCS theory, the Cooper pair state is responsible for superconductivity. In the way of classical explanation, due to the Coulomb interaction, an electron is repelled from other electrons and attracts the positive ions that make up the rigid lattice of the metal. The attraction distorts the ion lattice, moving the ions slightly toward the electron. Therefore, the positive charge density of the lattice in the vicinity is increased, which attract other electrons. This kind of attraction between electrons due to the displaced ions can overcome the repulsion of electrons and cause them to pair up. This effect is resulted by electron-phonon interactions, which can be explained by the rigorous quantum mechanical derivation. Here only the main results will be derived and discussed.

In the normal ground state all one-electron orbitals with momenta $k < k_F$ are occupied, and all the rest are empty. As mentioned, there is an attraction between paired electrons. The interaction will scatter electrons from states with initial momenta (k_1, k_2) to states with momenta (k_1', k_2'), where the final momenta (k_1', k_2') must be above the Fermi momenta k_F because all states below the Fermi surface are occupied. Now, let us consider the Schrödinger equation for two electrons interacting via the potential V:

$$\left[-\frac{\hbar^2}{2m}(\nabla_1^2+\nabla_2^2)+V(\mathbf{r_1}-\mathbf{r_2})\right]\Psi(\mathbf{r_1},\mathbf{r_2})=(\epsilon+2E_F)\Psi(\mathbf{r_1},\mathbf{r_2}), \tag{1.17}$$

where $\Psi(\mathbf{r_1},\mathbf{r_2})$ is the wavefunction, ϵ is the eigenvalue of the energy and E_F is the Fermi energy. The spin part is factored out in Eq. 1.17. Let us introduce the center of mass coordinate,

$$\mathbf{R}=(\mathbf{r_1}+\mathbf{r_2})/2, \tag{1.18}$$

and the relative coordinate,

$$\mathbf{r}=(\mathbf{r_1}-\mathbf{r_2}). \tag{1.19}$$

Therefore, Eq. 1.17 can be rewritten as

$$\left[-\frac{\hbar^2}{4m}\nabla_R^2-2\frac{\hbar^2}{2m}\nabla_r^2+V(\mathbf{r})\right]\Psi(\mathbf{R},\mathbf{r})=(\epsilon+2E_F)\Psi(\mathbf{R},\mathbf{r}). \tag{1.20}$$

Separating two coordinates $\mathbf{R}$ and r, *i.e.*, writing

$$\Psi(\mathbf{R}, \mathbf{r}) = \Phi(\mathbf{R})\Psi(\mathbf{r}), \tag{1.21}$$

we can find $\Phi(R)$ is a plane wave,

$$\Phi(\mathbf{R}) = e^{ik\cdot\mathbf{R}}, \tag{1.22}$$

and for $\Psi(\mathbf{r})$ we have

$$\left[-2\frac{\hbar^2}{2m}\nabla_r^2 + V(\mathbf{r})\right]\Psi(\mathbf{r}) = \left(\epsilon + 2E_F - \frac{\hbar^2 k^2}{4m}\right)\Psi(\mathbf{r}). \tag{1.23}$$

Now, we express $\Psi(\mathbf{r})$ as a sum over states with momenta $p > k_F$,

$$\Psi(\mathbf{r}) = \frac{1}{\sqrt{V}}\sum_{\mathbf{p}>\mathbf{k}_F} a(\mathbf{p})e^{i\mathbf{p}\cdot\mathbf{r}}. \tag{1.24}$$

Substituting 1.24 into 1.23, we then obtain the Schrödinger equation in momentum space,

$$[2(E_p - E_F) - \epsilon]a(p) + \sum_{p'>k_F} V(p,p')a(p') = 0, \tag{1.25}$$

with

$$E_p = \frac{\hbar^2 p^2}{2m} \tag{1.26}$$

$$V(p,p') = \frac{1}{V}\int e^{-i(p-p')\cdot r}V(r)d^3r. \tag{1.27}$$

In order to simplify the solution, we assume that

$$V(p,p') = \begin{cases} -V_0 & |E_p - E_F| \leqslant \hbar\omega_D,\ |E_{p'} - E_F| \leqslant \hbar\omega_D \\ 0 & \text{otherwise.} \end{cases} \tag{1.28}$$

Here, $\hbar\omega_D$ is a typical phonon energy. With the potential described in 1.28, the interaction term in 1.25 becomes

$$\sum_{p'>k_F} V(p,p')a(p') = -V_0 K\Theta(\hbar\omega_D - E_F - E_p), \tag{1.29}$$

where $\Theta(x)$ is the step function and $K = \sum_{p>k_F} a(p)$ is a constant. Therefore, from Eq. 1.25 we can get the solution for $a(p)$,

$$a(p) = \frac{V_0 K}{2(E_p - E_F) - \epsilon}\Theta(\hbar\omega_D - E_F - E_p). \tag{1.30}$$

By combining with the equation $K = \sum_{p>k_F} a(p)$, we can obtain a self-consistent equation. If we assume that $K \neq 0$ and then use the density of states at the Fermi surface $D(E_F)$ to approximate the value inside the integral $E_F \pm \hbar\omega_D$, the solution of the eigenvalue ϵ can be found,

$$\epsilon = -\frac{2\hbar\omega_D}{\exp\left[\frac{2}{V_0 D(E_F)}\right] - 1}. \tag{1.31}$$

This energy is also called binding energy of a Cooper pair. It tells us that the pair state will always have a lower energy than the normal ground state no matter how small the interaction V_0. Pairs of electrons (Cooper pairs) can behave very differently from single electrons. Cooper pairs act more like bosons and they can condense into the same energy level (*e. g.*, ground state). The electron pairs have a slightly lower energy and leave an energy gap above them which inhibits the kind of collision interactions which lead to ordinary resistivity. When the thermal energy is less than the band gap, the material exhibits zero resistivity. Therefore, the main properties of superconductors have been explained by BCS theory. For the details of the caculations of the energy gap, the ground state energy *etc*, see *e. g.*, Ref. [7, 12].

1.2.3.1 *Richardson equations*

Exactly solvable models have played a major role in helping to elucidate the physics of strongly correlated quantum systems. Examples of their extraordinary success can be found throughout the fields of condensed matter physics and nuclear physics [13].

Superconductivity is typically described by assuming a pairing Hamiltonian and treating it at the level of the BCS approximation [9], an approximation that explicitly violates particle number conservation [13]. The effect of the BCS approximation is negligible for macroscopic systems. However, when dealing with small or ultrasmall systems, significant errors can result from the BCS approximation. Since the fluctuations of the particle number in BCS are of the order of the square root of the number of particles

($\sqrt{N}$), improvements of the BCS theory are required for systems with $N \sim 100$ particles. In 1964, the number-projected BCS approximation [14] was developed. It has been used in nuclear physics for a long time and applied in studies of ultrasmall superconducting grains rencently [15]. In the latter, in order to properly describe the crossover from the superconducting regime to the pairing fluctuation regime, it is necessary to resort to the exact solution [16], which goes beyond the projected BCS approximation. Therefore, the exact numerical solution of the pairing model, published in a series of papers in the 1960s by Richardson [17, 18, 19, 20, 21, 22], was rediscovered and applied successfully to small metallic grains [23] and nanoshells [24, 25]. However, the exact Richardson solution was scarcely used until recently, although it has been presented in the nuclear physics literature since the 1960s.

Soon after the initial application of the exact solution of the pairing model to ultrasmall superconducting grains, it became clear that there is an intimate connection between Richardson's solution and a different family of exactly solvable models known as the Gaudin magnet [26]. Following their initial discussion of these exactly solvable quantum models, an exact mapping between these models and a two-dimensional classical electrostatic problem was proposed [27]. By exploiting this analogy, people are able to derive the thermodynamic limit of the exact solution, demonstrating that it corresponds precisely to the BCS solution.

These models has been widely applied, to ultrasmall superconducting grains [23, 28], to interacting boson models of nuclear structure [29], to electrons in a two-dimensional lattice [30], to confined Bose systems [31], and to a multielectron bubble in liquid helium [32]. The Richardson equations will be further discussed in Chapter 5.

1.3 VORTEX-VORTEX INTERACTION IN THE LONDON LIMIT

1.3.1 *Infinite type-II superconductors*

Let us consider a strong type-II superconductor, *i. e.*, the Ginzburg-Landau parameter $\kappa \gg 1$. It means the density of Cooper pairs becomes a constant in a short distance near the normal-superconducting interface. We can use the London approximation that the density is uniform in the superconductor except the core region of vortex and the fluxoid for around one vortex should be a flux quantum Φ_0, *i. e.*,

the flux in the core region with area of ξ^2 is Φ_0. Thus, we obtain the modified London equation

$$-\lambda^2\nabla^2\mathbf{H}+\mathbf{H}=\Phi_0\sum_i\delta(\boldsymbol{\rho}-\boldsymbol{\rho}_i)\hat{z} \tag{1.32}$$

where $\hat{z}$ is a unit vector along the vortex and $\boldsymbol{\rho}_i$ is the superposition of vortex.

If we consider only one vortex in an infinite superconductor, the equation is written as follow:

$$-\lambda^2\nabla^2\mathbf{H}+\mathbf{H}=\Phi_0\delta(\boldsymbol{\rho})\hat{z}. \tag{1.33}$$

The exact solution of Eq. (1.33) is:

$$H(\rho)=\frac{\Phi_0}{2\pi\lambda^2}K_0\left(\frac{\rho}{\lambda}\right), \tag{1.34}$$

where K_0 is the zeroth order Hankel function of imaginary argument. The free energy per unit volume in the London case is given by

$$F=\frac{\mathfrak{F}}{V}=\frac{1}{8\pi A}\int d^2\rho(H^2-\lambda^2|\boldsymbol{\nabla}\times\mathbf{H}|^2). \tag{1.35}$$

Then it is easy to find the interaction energy between two vortices in the high-κ approximation. We use superposition of vortices and calculate the magnetic field by

$$\mathbf{H}=\mathbf{H}_1(\boldsymbol{\rho})+\mathbf{H}_2(\boldsymbol{\rho})=[H(|\boldsymbol{\rho}-\boldsymbol{\rho}_1|)+H(|\boldsymbol{\rho}-\boldsymbol{\rho}_2|)]\hat{z} \tag{1.36}$$

where $\boldsymbol{\rho}_1$ and $\boldsymbol{\rho}_2$ are the superpositions of the two vortices and $H(\rho)$ is given by (1.34). The total free energy increasing per unit length is due to two parts: the individual energy and the interaction energy. Thus, the interaction energy is found as following

$$\epsilon_{12}=\frac{\Phi_0}{4\pi}H_1(\rho_{12})=\frac{\Phi_0^2}{8\pi^2\lambda^2}K_0\left(\frac{\rho_{12}}{\lambda}\right), \tag{1.37}$$

where $\rho_{12}=|\boldsymbol{\rho}_2-\boldsymbol{\rho}_1|$. The function $K_0(\rho_{12}/\lambda)$ decays as $\rho_{12}^{1/2}e^{-\rho_{12}/\lambda}$ at large distances and varies logarithmically when $\rho_{12}\to 0$. By taking a derivative of F_{12}, the interaction force between two vortices is given by

$$\mathbf{f}_{12}^{vv}=\frac{\Phi_0^2}{8\pi^2\lambda^3}K_1(\rho_{12}/\lambda)\hat{\rho}_{12}, \tag{1.38}$$

where $\hat{\rho}_{12} = (\boldsymbol{\rho}_2 - \boldsymbol{\rho}_1)/\rho_{12}$ is the unit vector from 'vortex 1' pointing to 'vortex 2'.

1.3.2 *Thin mesoscopic superconducting disks*

We can treat vortices as quasi-particles with interaction f^{vv} given by (3.10) in an infinite superconductor. However, in mesoscopic disks vortices interact with the boundary. Following the outline of Refs. [33, 34], we can obtain the free energy for the vortex state. In the London limit, considering a mesoscopic thin disk with thickness d and radius R in an external magnetic field H_0 such that $d \ll \xi \ll R \ll \Lambda = \lambda^2/d$, we can write the free energy as [34, 35, 36]

$$\mathfrak{F} = \sum_{i=1}^{L} \left(\epsilon_i^s + \sum_{j=1}^{i-1} \epsilon_{ij} \right) + \epsilon^{core} + \epsilon^{field}, \tag{1.39}$$

where

$$\epsilon^{core} = (2/R)^2 L \ln(R/a) \tag{1.40}$$

$$\epsilon^{field} = R^2 H_0^2/4 \tag{1.41}$$

Here a is a cut-off radius and we take $a = \xi/2$ instead of $a = \xi$. This yielded better defined transitions and results which are in better accordance with those obtained within the nonlinear Ginzburg-Landau theory at low fields [34].

are the energies associated with the vortex cores and the external magnetic field, and ϵ_{ij} is the interaction energy between vortices i and j [35, 36]:

$$\epsilon_{ij} = \left(\frac{2}{R}\right)^2 \ln\left[\frac{(r_i r_j)^2 - 2\mathbf{r}_i \cdot \mathbf{r}_j + 1}{r_i^2 - 2\mathbf{r}_i \cdot \mathbf{r}_j + r_j^2}\right]. \tag{1.42}$$

Here $\mathbf{r}_i = \boldsymbol{\rho}_i/R$ is the normalized distance to the vortex i. In Eq. 1.39, the potential energy of vortex confinement ϵ_i^s consists of the interaction energy between the vortex and the radial boundary

$$\epsilon_i^{self} = \left(\frac{2}{R}\right)^2 \ln(1 - r_i^2), \tag{1.43}$$

and the interaction energy between the vortex and the shielding currents

$$\epsilon_i^{shield} = -2H_0(1 - r_i^2). \tag{1.44}$$

Then one can obtain the force from the gradient of the energy:

$$\begin{aligned} \mathbf{f}_i &= -\boldsymbol{\nabla}_{\mathbf{r}_i} \mathfrak{F}(\mathbf{r}_1, \cdots, \mathbf{r}_L) \\ &= -\boldsymbol{\nabla}_{\mathbf{r}_i} \left(\sum_{j=1, j\neq i}^{L} \epsilon_{ij} + \epsilon_i^{self} + \epsilon_i^{shield} \right). \end{aligned} \tag{1.45}$$

1.4 SUPERCONDUCTING CORBINO DISKS

The dynamics of vortex matter in mesoscopic and nano-structured superconductors has attracted an increasing interest of researchers studying the fundamental properties of vortex matter and its practical applications in superconducting devices. Over the last decade, the dynamics of vortices in superconducting disks has been actively studied by using a Corbino geometry [37, 38, 39, 40, 41, 42, 43, 44]. In a Corbino geometry (see Fig. 1.4), a superconducting disk is placed in an external perpendicular magnetic field H_0 with a radial driving current I, which is injected at the center of the disk and removed from its edge. The density of the current j decays as $1/\rho$ along the radius [37, 38, 42, 43, 44, 46], so the driving force (*i. e.*, the Lorentz force) $\mathbf{f}^d$ that acts on a vortex near the center of the disk is larger than that close to the edge. This natural gradient of the driving force allows a direct examination of the elastic moduli of the vortex lattice, *e. g.*, the shear modulus.

The Corbino geometry has also been studied in (semi-)conductors, e. g., *most recently in bilayergraphene [45].*

1.4.1 *Vortex shells in mesoscopic disks*

In infinite superconductors and in thin films, vortices form a triangular Abrikosov lattice [8] as a consequence of the isotropic repulsive vortex-vortex interaction. Therefore in large disks most of vortices are packed in a triangular lattice except those near the interface (*e. g.*, see Ref. [43]). However, in mesoscopic superconducting disks, they are also affected strongly by the circular boundary. The competition between the vortex-vortex interaction and boundary effect results in different configurations of vortices. Due to the interaction between the vortices and the edge, the configuration of vortices in mesoscopic disks experiences a transition from vortex shells to the Abrikosov lattice with increasing size of the system [35]. Vortices obey specific rules for filling shells in small disks (*e. g.*, see Fig. 1.5), which have been found in numerical simulations [34, 47]

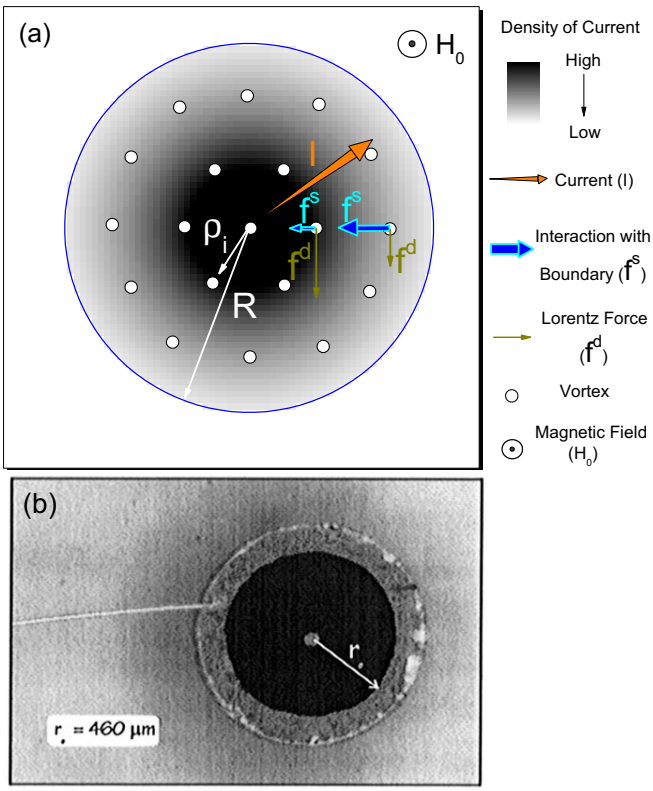

Figure 1.4: a) Schematic plot of a Corbino disk: a current is injected at the center of the disk and flows radially to the edge in the presence of an external perpendicular magnetic field H_0. b) The experimental setup of a macroscopic Corbino disk (after Ref. [37]). The vortex is driven by the gradient Lorentz force due to the inhomogeneous density of the current along the radius.

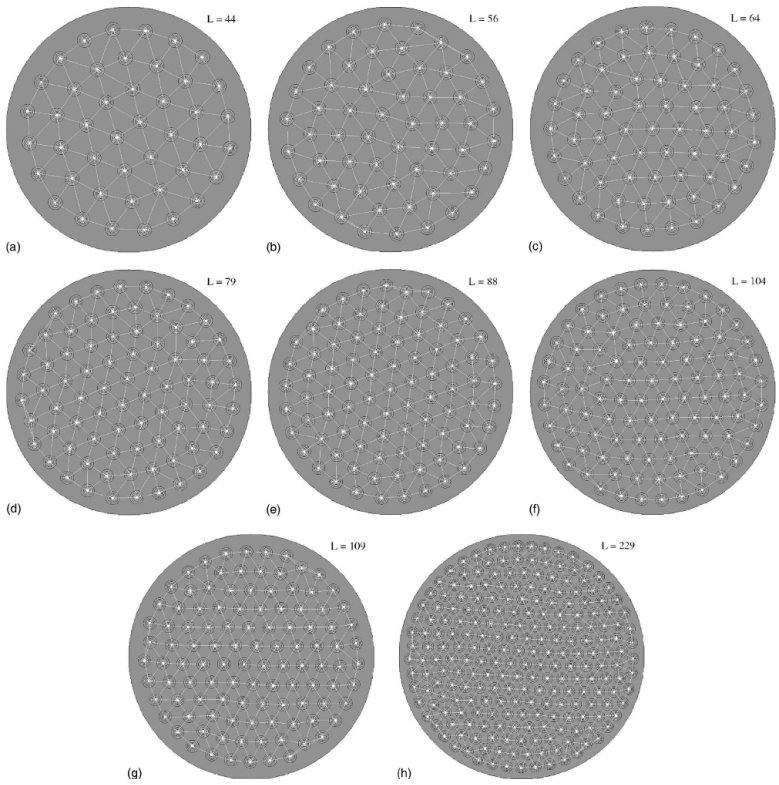

Figure 1.5: Superconducting electron density for L = 44, 56, 64, 79, 88, 104, 109, and 229 obtained at $H_0 = 0.04$, 0.05, 0.06, 0.07, 0.08, 0.09, 0.10, and 0.20, respectively. The white lines depict the Delaunay triangulation for the vortex core positions (Ref. [35]).

and were recently observed in experiments by using the Bitter decoration technique (see Fig. 1.6) [48, 49].

1.4.2 *Dynamics of vortices in disks*

The transition from elastic (*i. e.*, vortex lattice under elastic deformations) to plastic (*i. e.*, vortex liquid) vortex motion in large Corbino disks has been investigated in Refs. [40, 42, 43, 50]. Two sharp jumps of the global resistance at two critical current values in large disks have been found [43]. The system transits from rigid body motion to plastic flow motion and proceeds from plastic motion to laminar motion at those two jumps, respectively. Laminar flow can occur both in sheared liquid and crystalline vortex matter phases [50]. In experiments, Okuma *et al.*found a formation of rotating vortex rings composed of triangular-lattice arrays by using measurements of a

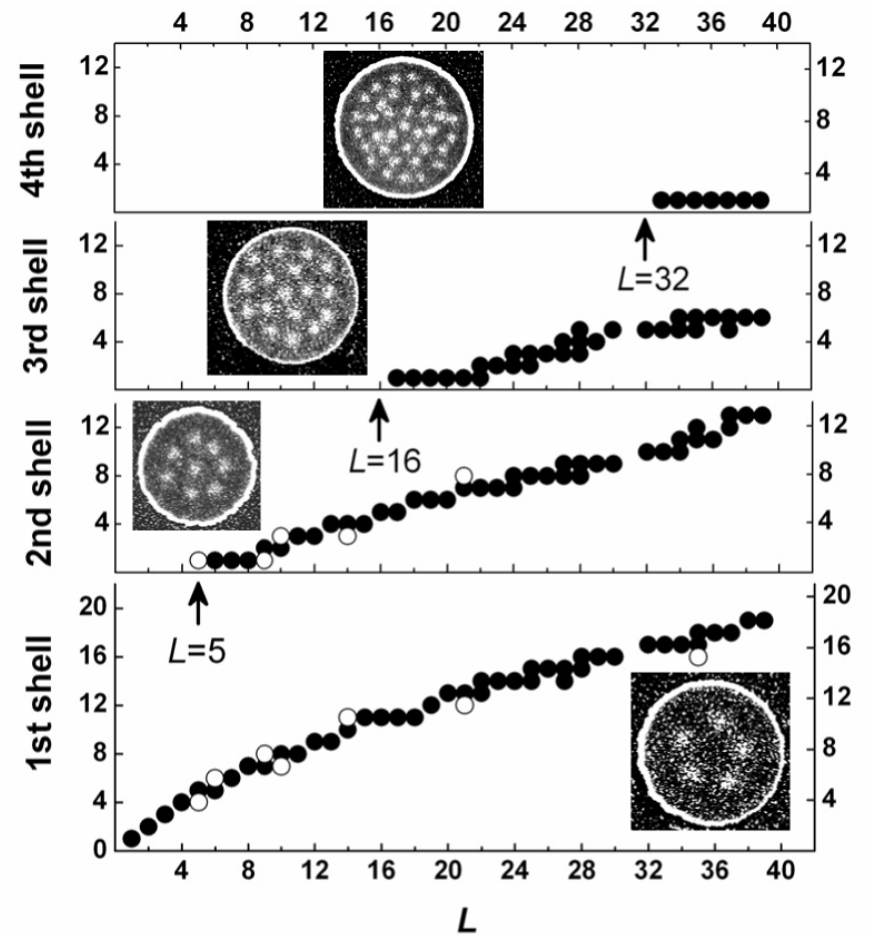

Figure 1.6: Number of vortices populating different shells as a function of L. Two or more different states were found for some vorticities, *e.g.*, (1, 7, 14) and (2, 7, 13) for L = 22, (1, 5, 12, 17), (1, 5, 11, 18), (1, 6, 11, 17), and (1, 6, 12, 16) for L = 35, *etc*. Open circles show numbers of vortices in a shell corresponding to the configurations that could be clearly identified as metastable. Arrows indicate magic numbers, *i.e.*, L corresponding to closed shell configurations, just before the appearance of the 2nd, 3rd, and 4th shell. The first magic number, L = 5, corresponds to the stable state (5) rather than the metastable state (1, 4). Insets: SEM images of vortex states with different numbers of shells: 1-shell state (5) [L = 5]; 2-shell state (1, 7) [L = 8]; 3-shell state (1, 5, 11) [L = 17]; 4-shell state (1, 5, 11, 18) [L = 35] (Ref. [48]).

mode-locking resonance [51]. The vortices near the center are first depinned and do the plastic-flow rotation. With increasing driving current I, it gradually approaches a laminar flow at large I [51].

The dynamics of vortex shells in small mesoscopic Corbino disks, having only two or three shells, was investigated by Misko and Peeters [44]. By applying an increasing external current I_0 to such a system, the vortex shells unlock at a critical value of the current I_c and start to rotate with different angular velocities (which is called "angular melting" [44, 52, 53, 54, 55]), while for $I_0 < I_c$ all the vortices rotate as a rigid body. With increasing magnetic field, a "structural transition" was revealed when a vortex jumped from the outer shell to the inner shell [44], similar to the Coster-Kronig transition in hollow atoms [56]. A two-step angular melting was found in a three-shell system with increasing temperature when the driving current is below the depinning threshold, which was similar to what was found in experiments [37, 38].

An experiment using large disks ($\sim 700\mu m$) was presented in Ref. [37, 38]. Untwinned crystals of $YBa_2Cu_3O_{7-\delta}$ were cleaved into two pieces-one piece carefully polished into a disk shape and the other into a rectangular geometry commonly used in four-probe resistivity measurements. Current was injected via a gold contact at the center and removed from a ring-like contact at the edge of the superconducting disks. A series of voltage contacts was evaporated along a radius to spatially resolve the radial dependence of the vortex velocity [37, 38]. However, in our simulations in Chapter 3, the size of disks is 50ξ. Therefore, the size of the contact at the center should small enough for experimental measurements because the first shell is located at $r = 5\xi$. One can introduce artificial channels in large disks and possibly measure that the angular melting process of artificial vortex shells (due to the confinement of the channels).

1.5 RATCHET EFFECT

A net flow of particles under unbiased external fluctuations/drive due to an asymmetric potential, which is called ratchet effect, has received much attention during the last decades. The transport and dynamical properties of particles on asymmetric potential have been widely studied, *e. g.*, in physics and biology [57, 58, 59, 60, 61, 62, 63, 64, 65]. The random motion of particles can be rectified in such an asymmetric system, which can be used for, *e. g.*, controlling

particle motion, separating different types of particles (*i. e.*, molecular sieves), for both underdamped and overdamped particles [62] and for molecular motors [61]. Vortices in a type II superconductor often (*e. g.*, for magnetic field close to H_{c1}) can be treated as classical overdamped "particles". Most of the experiments on vortex motion rectification used arrays of asymmetric pinning sites (*e. g.*, nanoengineered antidots or triangular magnetic dots/inpurties) to create an asymmetric potential, which rectifies the motion of vortices [65, 66, 67, 68, 69, 70, 71, 72, 73]. The rectified vortex motion was directly observed in experiments by imaging vortices via Lorentz microscopy [74]. Periodic arrangement of point defects of a gradual density or periodic square array of ferromagnetic dots of decreasing size, *i. e.*, varying the density of pinning sites or the size of pinning sites, were shown to result in a ratchet potential [75, 76]. When vortices are trapped by pinning sites, the repulsive vortex-vortex interaction creates a higher energy barrier near the area with higher density of pinning sites. Therefore, an asymmetric potential can be created by the gradient of the density of pinning sites [75]. Even without spatial asymmetry (*i. e.*, without any asymmetric walls/boundaries or asymmetric pinning sites), the motion of vortices still can be controlled by time-asymmetric driving force [77, 78, 79]. Due to the possibility of controlling their motion, the dynamical behavior of vortices in such systems has attracted considerable interest. A series of elastic and plastic vortex flow phases were found [47, 80, 81, 82, 83, 84]. Besides the liquid-like and solid lattice phase, vortex motion also revealed a jamming behavior [84, 85]. When the density of vortices is changed, the vortex flowing direction can change to the opposite [66, 67, 76, 86], which means vortices can drift in either the "hard" direction or the "easy" direction of the ratchet, depending on the vortex density (*e. g.*, see Fig. 1.7). By controlling the motion of vortices, it is possible to remove vortices or reduce the vortex density by using a combination of two opposite oriented ratchet arrays [87]. The order of vortices and commensurability between vortices and cells also play an important role in vortex dynamics [71, 76, 84, 86]. In two-dimensional (2D) ratchets, the dynamics in the transverse ratchet was was first predicted theoretically in Ref. [88] and then further studied in theory [62, 89] and in experiments [90, 91].

For studies of vortex matter in confined geometries, nanoscale channels for guiding vortices through superconducting films with a minimal influence from pinning have been developed, including

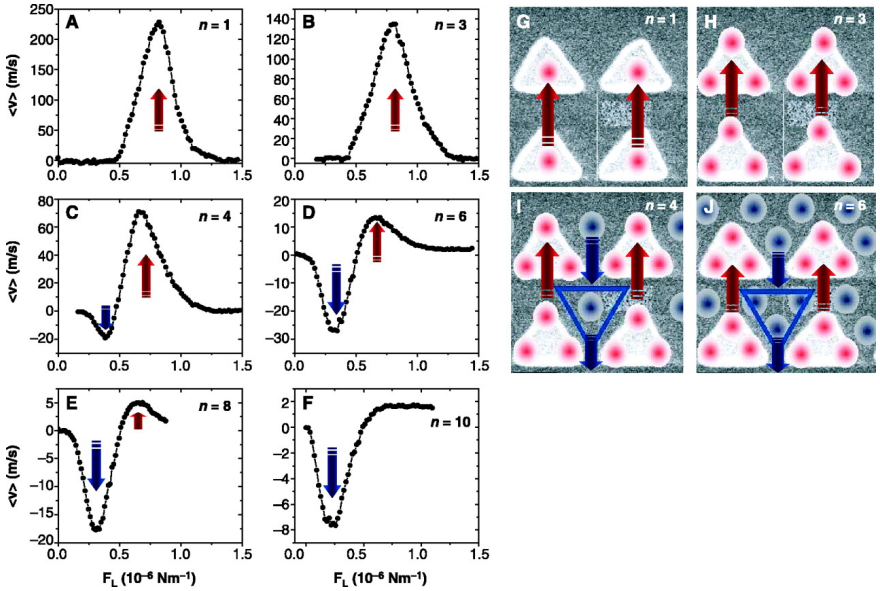

Figure 1.7: (A)-(C) The calculated net dc velocity $\langle v \rangle$ versus ac amplitude F obtained for different effective asymmetry values $\eta = F_{max}/F_{onset}$ with a simple model that describes the mixture of pinned and interstitial vortices. Red curves show velocities at T = 0 and green curves at $T/(lFmax) = 0.0085$, with $l = 1$ and $F_{max} = 0.85$ corresponding to pinned vortices and $n = 1$. The values of F_{max} and F_{onset} are (A) 0.85 and 0.45 for pinned vortices, (B) 0.7 and 0.5 for pinned vortices and 0.3 and 0.15 for interstitial vortices, and (C) 0.6 and 0.5 for pinned vortices and 0.3 and 0.2 for interstitial vortices. (D) The pinned vortices move on the asymmetric potential $U^{pv}(y)$ (top), whereas the interstitial vortices feel the potential $U^{iv}(y)$ (bottom). The latter potential is weaker, inverted, and originates from the interaction of the interstitial vortices with the pinned vortices. Here, η is taken to be 10^{-3} (Ref. [67]).

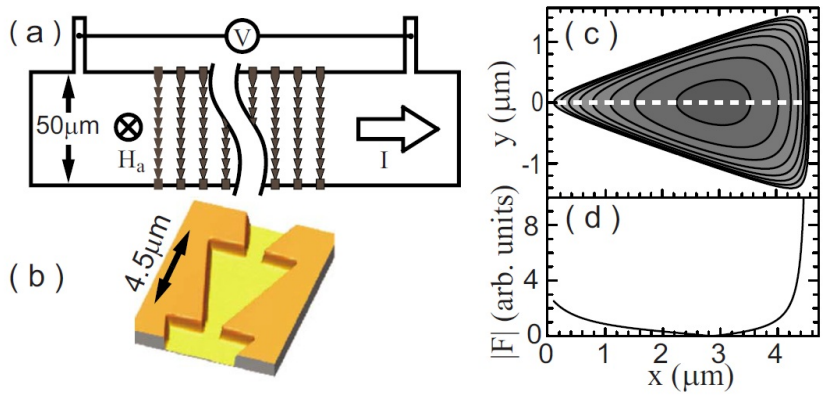

Figure 1.8: (a) Schematic of strip with ratchet channels; channel spacing is 10 μm. (b) AFM image of one ratchet cell; channel depth is 88 nm. (c) Contour plot of the model potential for a vortex interacting with ratchet cell walls. (d) Magnitude of the corresponding force along the center of the channel (Ref. [63]).

experiments on melting [92], commensurability [93], mode-locking [94], and ratchet effect [63].

Such channels are fabricated from bilayer films of an extremely weak-pinning superconductor and a relatively strong pinning superconductor, (*i. e.*, amorphous-NbGe and NbN). A reactive ion etching process removes NbN from regions as narrow as 100 nm, defined with electron-beam lithography, to produce weak-pinning channels for vortices to move through easily, while vortices trapped in the NbN banks outside of the channels remain strongly pinned. *E. g.*, in the experimental group of Plourde [63], they have fabricated weak-pinning channels with 200nm thick films of a-NbGe and 50nm thick films of NbN on a Si substrate, and many of the channels such that the walls have an asymmetric sawtooth pattern has been designed (see Fig. 1.8). Such channels are fabricated from bilayer films of amorphous-NbGe, an extremely weak-pinning superconductor, and NbN, with relatively strong pinning.

1.6 EXPERIMENTAL METHODS

There are several experimental techniques that can be used to measure the positions of vortices in a superconductor and to analyse the motion of vortices, *e. g.*, Bitter decoration technique, scanning tunneling microscopy (STM), Lorentz microscopy and even by super-

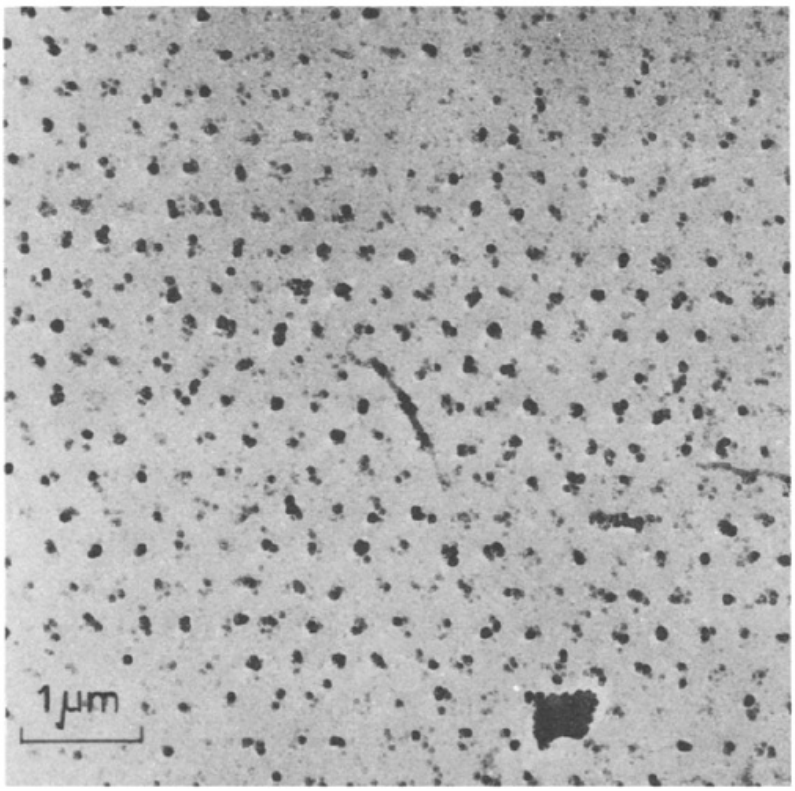

Figure 1.9: "Perfect" triangular lattice of flux lines on the surface of a superconductor at l.lK. The black dots consist of small cobalt particles which have been stripped from the surface with a carbon-replica (Ref. [96]).

conducting quantum interference device (SQUID). We will give a brief introduction to these techniques in the following.

After the mixed state was first predicted by Abrikosov [8], Träuble and Essmann [95, 96] observed the flux lines (*i. e.*, vortices) form a triangular lattice in an anisotropic and defect-free superconductor with the help of the Bitter decoration technique (see Fig. 1.9). The main idea of the decoration technique is to use small ferromagnetic material powders (particles) to sense the magnetic field on the surface of superconductors [98]. Due to the effect of the inhomogeneous magnetic field, particles drift to the sample surface and preferentially locate on the region with a magnetic field and form patterns. The regions with high density of particles are the normal core of vortices in the superconductor so the configuration of vortices can be visualised with the help of the ferromagnetic powders. However, there are a few difficulties to decorate in experiments.

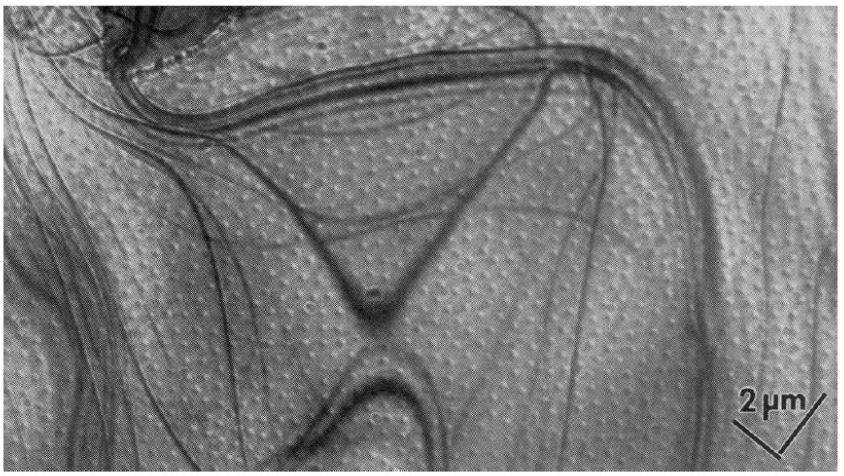

Figure 1.10: Lorentz micrograph of a Nb thin film. A magnetic field of 100G is applied to the film in the superconducting state at 4.5K. Vortices are observed as small globules, each with black and white contrast. The magnification differs in the two directions by $\sqrt{2}$, because the film is tilted by 45°. The dark lines are bend contours (Ref. [97]).

First, the size of the particles must be small enough (much smaller than the normal core of the vortices $\xi \sim 10$nm). Then, the particles should not stick to each other during drifting to the surface. Last, their kinetic energy should not be too high. These requirements are met by evaporating a ferromagnetic material (Fe, Ni, or CO) at a small distance from the superconducting sample, in a background of helium gas. After the decoration, the superconductor is warmed up to room temperature and the resultant distribution of magnetic particles, which represent the configuration of vortices, is examined in a scanning electron microscope (SEM). Although the Bitter decoration technique provided a wealth of information about static vortex structures in type-II superconductors, it becomes difficult to image vortices in high temperature or in high magnetic field. Since the typical time of decoration is 1-2 s and typical vortex velocities are 10-10^3 m/s, it is also hard to directly observe the motion of vertices in large areas.

Experiments in which vortex movements were registered by microscopic Hall probes [99, 100] have shown that the vortices (in thin films of Pb) move in bundles of 10-20 vortices, even though the static correlation length ξ was of the order of one vortex spacing.

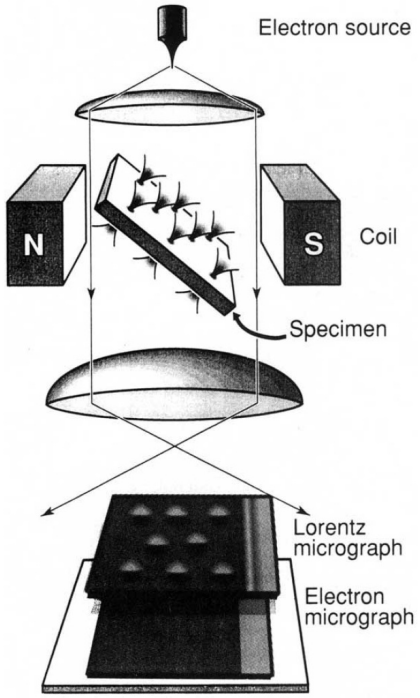

Figure 1.11: Schematic diagram of vortex-lattice observation (Ref. [97]).

The Lorentz microscopy (a technique based on electron microscopy) was first used to do the real-time observation of vortex lattice by Harada *et al.* [97]. Comparing with the Bitter decoration technique, by which it is hard to image vortices in high magnetic field, Lorentz microscopy can be applied to observe the real-time image of vortices in high magnetic field (*e. g.*, see Fig. 1.10). As shown in Fig. 1.11, the sample was positioned on a low-temperature stage and tilted at 45° to the vertically incident electron beam, so that the electrons could sense the vortex magnetic fields penetrating the sample perpendicularly to its surface; the penetrating field was applied horizontally due to an external magnetic field. The objective lens was turned off to remove its vertical magnetic field and the intermediate lens was used instead for focusing. Considering the advantage of the real-time observation, the rectified vortex motion was also directly observed (see Fig. 1.13) by imaging vortices via Lorentz microscopy [74].

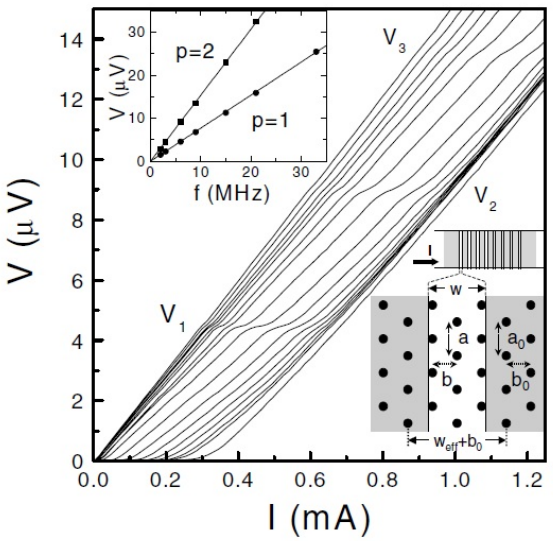

Figure 1.12: Main panel: dc-IV curves at 60 mT measured with superimposed 6 MHz rf currents (amplitude 4.7, 3.8, 3.0, 2.4, 1.9, 1.5, 1.2, 0.94, 0.75, 0.59, 0.47, 0.38, 0.30, 0.24, 0.19, 0.15, and 0 mA, from left to right). Interference voltages V_p are indicated. Upper inset: frequency dependence of the lowest two interference voltages. Lower inset: schematic geometry of the sample and a single channel. Strong pinning channel edges are marked in gray. The (local) vortex lattice parameters and (effective) channel width are indicated (Ref. [94]).

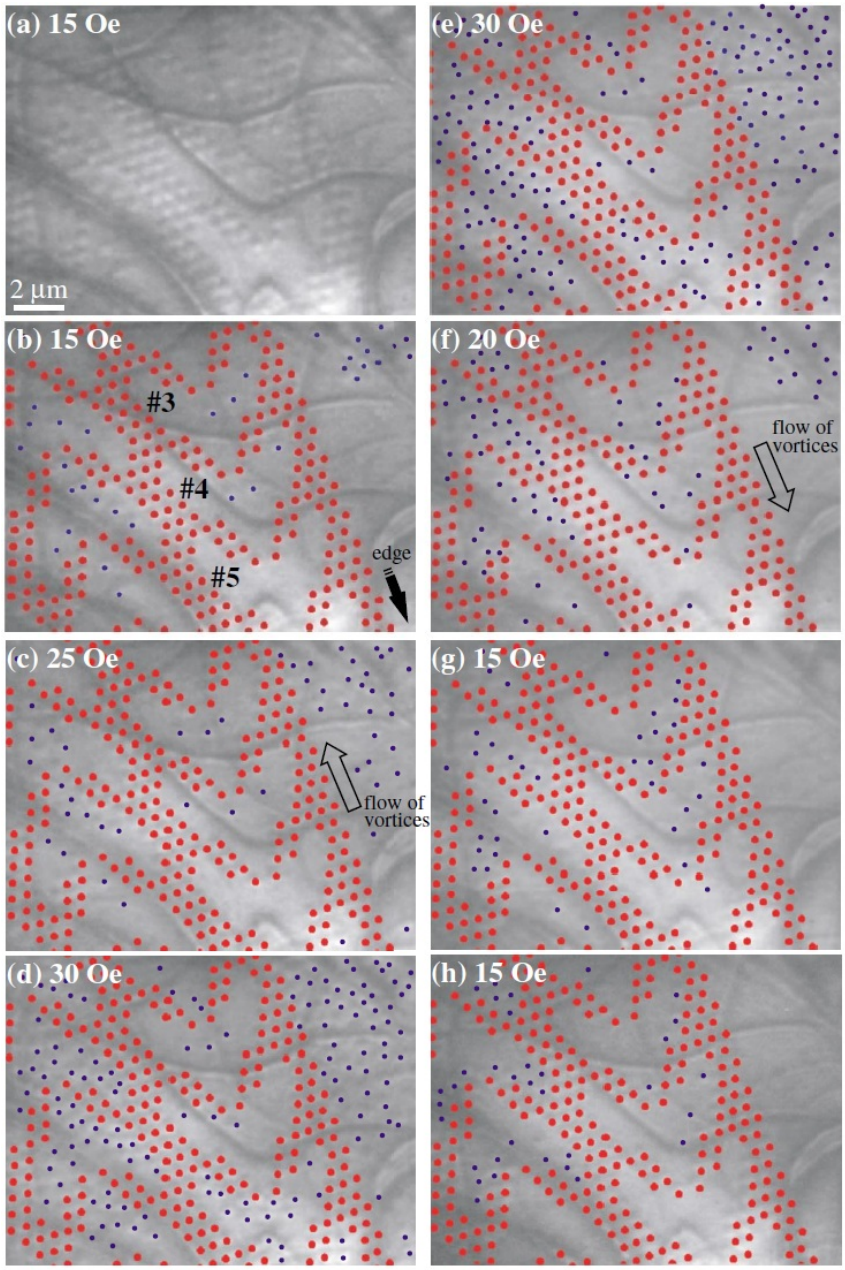

Figure 1.13: Sequence of Lorentz image snapshots of moving vortices in a period of the ac applied magnetic field at 6.9 K. Pinned and unpinned vortices are represented by red and blue circles, respectively, in (b)-(h). (a) and (b) are the same snapshot. (b)-(d) With increasing magnetic field H, vortices flow upward; (e)-(g) With decreasing magnetic field H, vortices flow downward. Arrows indicate the directions toward the edge of the sample, and the flow of vortices (Ref. [74]).

2

NUMERICAL APPROACHES

There are several numerical approaches to solve different problems of physics, such as numerical diagonalization, finite element and finite differential, Monte Carlo etc. For those problems that cannot be solved analytically, numerical simulations have be proved to be a valuable tool, particularly for providing results for specific parameters which otherwise are not obtained at all.

The simulations used to study many-body systems can be ordered from stochastic to deterministic [101]. The Monte Carlo method can be adopted for solving high dimensional integrals, however, in that kind of simulations the statistical mechanics ensemble average for a property is interesting and calculated. In the simulation of many-body systems, particle positions are altered by random trial moves which are conditionally accepted. Depending on the previous configuration, the new configuration is found by moving a particle over a small distance which is generated by a random number generator and determined by strict condition(s). Therefore, the configurations are obtained stochastically. The obvious advantage of molecular dynamics method over the Monte Carlo method is that it gives a route to dynamical properties of the system [102].

Molecular dynamics method determines particles positions by integrating equation of motion, *e. g.*, Newton's equation. For N particles with a set of positions $\mathbf{r}_i$, the Newton's equations solved are

$$m_i \frac{d^2\mathbf{r}_i}{dt^2} = \mathbf{f}_i(\mathbf{r}_1, \ldots, \mathbf{r}_N, \frac{d\mathbf{r}_1}{dt}, \ldots, \frac{d\mathbf{r}_N}{dt}, t) \tag{2.1}$$

with $i = 1, \ldots, N$. Here m_i is the mass of ith particle and $\mathbf{f}_i$ is the total force acting on the particle. Langevin-type dynamics is also one of developed molecular dynamics methods. This method is used to study (quasi-)particles immersed in a continuum, *e. g.*, a fluid. Let us first introduce the Langevin equation of motion.

The Langevin equation was first proposed to describe the motion of Brownian particles with mass m_i. Particles and their interactions with the continuum are investigated instead of considering all microscopic interactions of all particles establishing the fluid. There are forces due to the continuum that a particle experiences. One is a viscous force $-\eta\frac{d\mathbf{r}_i}{dt}$, and the other one is a random force $\zeta(t)$ with a zero average. The corresponding stochastic dynamics is described by the following (Langevin) equation [61]

$$m_i\frac{d^2\mathbf{r}_i}{dt^2} = -\eta\frac{d\mathbf{r}_i}{dt} + \zeta(t) + \mathbf{f}_i^{other} \tag{2.2}$$

where $\mathbf{f}_i^{other}$ represents rest forces, *e. g.*, confinement force. If the fluctuations of the random force are faster than any other process, *i. e.*, the system-bath interaction is Markovian, thermal fluctuations ξ satisfy

$$\langle\zeta(t)\rangle = 0 \tag{2.3}$$

and

$$\langle\zeta(t)\zeta(t')\rangle = 2D\delta(t-t'). \tag{2.4}$$

The momentum-diffusion strength $D = \eta k_B T$ with the Boltzmannn constant k_B and the temperature of an equilibrium heat bath T.

The friction can be strong enough that the velocities of the system reach a steady state before any other process is observed. In this case, inertial effects are small and negligible, and we can set the mass to zero, *i. e.*, the inertial term $m_i\frac{d^2\mathbf{r}_i}{dt^2}$ is dropped altogether with respect to the friction term $-\eta\frac{d\mathbf{r}_i}{dt}$ (the Smoluchowski approximation) [61] so that the differential equations are reduced from second order to first order and the modified Langevin equation is described by [61, 103]

$$\eta\frac{d\mathbf{r}_i}{dt} = \zeta(t) + \mathbf{f}_i^{other}. \tag{2.5}$$

Because the absent inertial term corresponding to the overdamped motion, the equation is also referred to as the “overdamped" Langevin equation of motion. In the overdamped limit, the particle spends more time at a given position and the effect of collisions is to cause diffusion.

2.2 SIMULATION OF THE VORTEX STATE

The vortex states are simulated by using several methods, the most direct one of that is numerically solving the Ginzburg-Landau equations to obtain the complex valued order parameter ψ and the magnetic vector potential. In this case, the set of coupled non-linear partial differential equations are solved, *e. g.*, on a discrete grid [104, 105, 106]. This approach does not simplify the physical situation. However, it demands a lot of computational resources because many grid points are required even for a single vortex.

Another way to start simulations is that we treat the vortex as a structureless point object. The point represents the center of vortex core where the order parameter ψ drops to zero and the superconductor is at normal state in the core, *i. e.*, in the London approximation. We can model the interaction between vortices by an effective interaction potential [107] and consider vortices as classical particles. The disadvantage is that the small length scale ξ is lost, thus the phenomena as vortex-antivortex creation or flux getting into the system does not intrinsically come with the model. However, the computational complexity is well decreased and some physical amounts are easily calculated, *e. g.*, velocities of vortices. We can use the Monte Carlo method to study the static state (*e. g.*, [108]) but in order to study the dynamics of vortices, a Langevin-type equation has to be applied and the molecular dynamics is required (*e. g.*, [44, 109]). In most of our works (mentioned in Chapter 3 and 4), we followed the Langevin-type molecular dynamics approach and studied the static and dynamic behavior of vortices. Other methods except those mentioned above are also able to simulate the physics of vortex states, *e. g.*, investigating a disordered array of Josphson junction.

In the London approximation, vortices are modeled as normal cores with flux.

This approach is not limited to vortex state simulations. It can also apply to general particle simulations with modifying, e. g., the interaction force.

2.3 FORCES EXERT ON VORTICES

The Langevin equation has been introduced in Sec. 2.1. For a vortex state of superconductors, we can specify the other force $\mathbf{f}_i^{other}$ and express the overdamped Eq. 2.5 as following:

$$-\eta \frac{d\mathbf{r}_i}{dt} = \mathbf{f}_i^{vv} + \mathbf{f}_i^{d} + \mathbf{f}_i^{T} + \mathbf{f}_i^{pin} + \mathbf{f}_i^{B}. \tag{2.6}$$

where f_i^{vv}, f_i^d, f_i^T, f_i^{pin}, f_i^B are the vortex-vortex interaction, the driving force, the thermal force (the same as previous ζ), the pinning force, and the force due to the boundary, respectively.

2.3.1 *Viscosity*

For an ideal homogeneous material, Bardeen and Stephen showed that the viscous drag force is $-\eta v$ and the viscosity coefficent η per unit volume is given by [110]

$$\eta = B^2/\rho_v \tag{2.7}$$
$$\rho_v = \rho_n B/B_{c2}, \tag{2.8}$$

with the magnetic field B and the upper critical value of magnetic field B_{c2}. Here ρ_v and ρ_n are repectively the flux flow resistivity and normal state resistivity of material. Eq. 2.7 has been confirmed in experiments [111]. Because the unpaired normal electrons experience the local electric fields induced by moving vortices, the normal state resistivity enters the expression. When vortices move, the system has dissipation and the energy comes from the external applied current. This results a voltage across the material and thus the material is not without resistance anymore.

2.3.2 *Interaction*

The isolated vortex-vortex interaction has been introduced in Sec. 1.3. For simulations, we have three relevant expressions of the interaction energy: ln, K_0 and Pearl's solution (for isolated thin films of high-T_c superconductors).

Let us first review the solution to the interaction potential in a large sample (Eq. 1.37). The modified Bessel function of second kind

$$K_0(x) \approx \begin{cases} -\ln(x/2) - \gamma & x \ll 1 \\ \sqrt{\frac{\pi}{2x}} e^{-x} & x \gg 1 \end{cases} . \tag{2.9}$$

In large size of superconductor, we have to use the Bessel function. However, in small size of typical type-II superconductor, where $R \ll \lambda$ and $\xi \ll \lambda$ the solution can be modelled by a logarithmic potential,which gives the derivative

$$K_1(x) \approx 1/x. \tag{2.10}$$

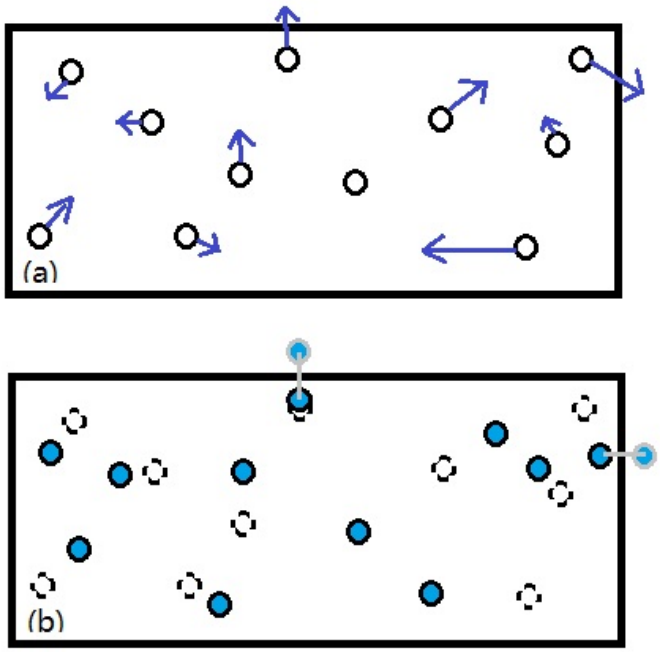

Figure 2.1: Hard-wall boundary conditions. When the particle (vortex) meets the boundary, the perpendicular movement is forced to be opposite so that particles (vortices) are always in the simulation sample. The gray circles in (b) show the positions without boundary.

Therefore, the vortex-vortex interaction per length becomes

$$\mathbf{f}_{ij}^{vv} = f_0 \frac{1}{|\mathbf{r}_i - \mathbf{r}_j|} \frac{\mathbf{r}_i - \mathbf{r}_j}{|\mathbf{r}_i - \mathbf{r}_j|} = f_0 \frac{\mathbf{r}_i - \mathbf{r}_j}{|\mathbf{r}_i - \mathbf{r}_j|^2}, \quad i \neq j. \tag{2.11}$$

where f_0 is the unit of force and $r_{i(j)} = \rho_{i(j)}/R$ is dimensionless distance. Antisymmetry of the interaction force can be used to optimise its computation. In mesoscopic disks, an additional term (see Eq. 3.10) due to the image of vortices are included in the interaction force because of the disk geometry. Appropriate boundary conditions are necessary to perform simulations.

2.3.3 *Boundary Conditions*

In simulations of vortex states, the boundary conditions are also important and must be correctly chosen. One simple way to model the boundary is "hard wall" boundary condition (*e. g.*, see Fig. 2.1). The

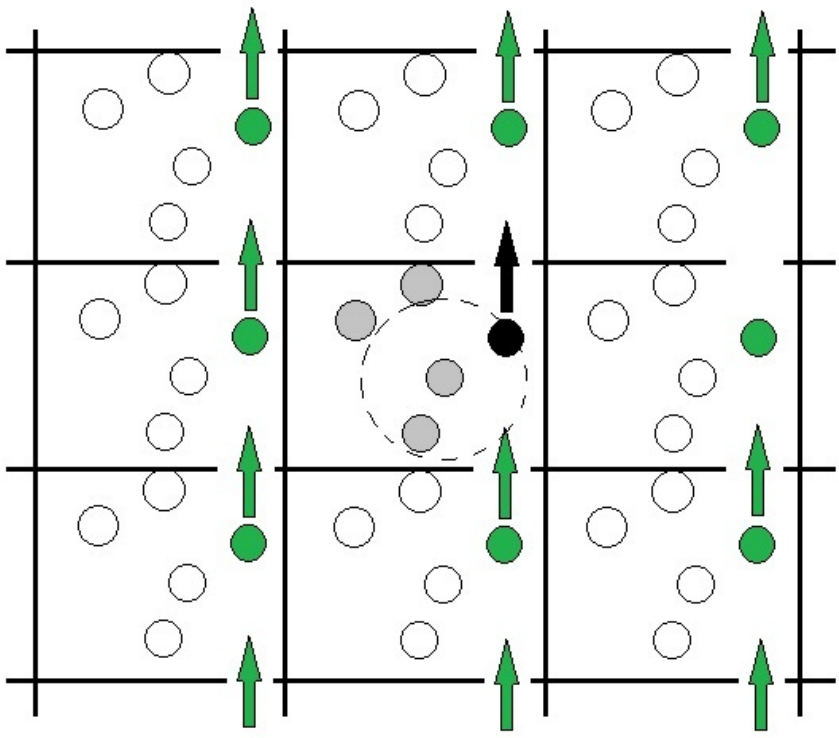

Figure 2.2: Periodic boundary conditions. When a particle (vortex) moves out of the simulation sample (the small square at the center), an image particle (in another square) moves in to replace it. Therefore, the number of particles (the vorticity) keeps the same. In calculating particle interactions within the cutoff range (the dash circle), both real (solid circles) and image (empty circles) neighbours inside the range are included.

vortices are just confined inside the sample and are not allowed to move across the boundary. However, this kind of boundary condition may lead to unstable configurations, and because the absence of the repulsion from the boundary, the majority of vortices moves to the boundary because of the repulsive interaction force. Therefore, an appropriate boundary condition should relax the vortices and results an approximately constant vortex density.

One approach to avoid the influence of surfaces on the system is to use periodic boundary condition (*e. g.*, see Fig. 2.2). Therefore, an infinite size of system is simulated by a periodic array of imaging samples. However, it must find a good way to cut-off while dealing with the interaction, particularly, across the boarder of the sample.

In our simulations of mesoscopic Corbino disks (Chapter 3), we modelled a confined boundary condition, *i. e.*, the current in the

sample can not flow in the perpendicular direction at the boundary and an external magnetic filed can penetrate into the sample. Therefore, we have the additional term in the interaction force and the confined force, the force due to the vortex interaction with the shielding currents and the edge $\mathbf{f}_i^s$ is [44, 33, 34]:

$$\mathbf{f}_i^s = f_0 \left(\frac{1}{1 - r_i^2} - h \right) \mathbf{r}_i \tag{2.12}$$

with the dimensionless applied magnetic field h.

3

DYNAMICS OF VORTEX SHELLS IN MESOSCOPIC CORBINO DISKS

Vortex shells in superconducting disks have been obtained both in simulations and in experiments. The dynamics of vortices in relatively large SC disks as well as in small mesoscopic disks have been studied. However, in large disks vortices form lattice instead of shell structures, as mentioned in Section 1.4.

In this chapter, we are interested in *large mesoscopic* disks that contain *several* vortex shells, *i.e.*, the intermediate case between small mesoscopic disks and macroscopic disks where vortices form a lattice [55, 112, 113]. In view of the interplay between the vortex-vortex interaction and the confinement, our findings will lead to a better understanding of the rich dynamics of multi-shell systems. The possibility of unusual ("unconventional") dynamics and melting of shells in mesoscopic Corbino disks is demonstrated. We analyze the free energy and the statistics of different vortex states, discuss the mechanism of inter-shell "friction" in commensurate and incommensurate shells, and systematically investigate the dynamics of vortex shells by considering many different vortex configurations. Two different types of defects is classified and the propagation of a "compression-decompression wave", induced by defects, is the reason that results in "unconventional" dynamics of vortex shells. Now, let us first mention some details about the simulations and our model.

3.1 MODEL AND SIMULATION

In a typical type-II superconductor when the magnetic field is weak enough so that vortices are well separated (*i.e.*, in London limit). Then we can treat vortices as classical "particles". In order to study the dynamics of vortices driven by the Lorentz force that is induced by the external current, we perform Langevin-type molecu-

The Langevin equation has been discussed in Section 2.1.

lar dynamics (MD) simulations and numerically integrate the overdamped equations of motion [34, 44, 47, 49, 55, 80, 81, 114]:

$$\eta \frac{d\mathbf{r}_i}{dt} = \mathbf{f}_i \tag{3.1}$$

with

$$\mathbf{f}_i = \mathbf{f}_i^{vv} + \mathbf{f}_i^{T} + \mathbf{f}_i^{d} + \mathbf{f}_i^{s}, \tag{3.2}$$

where η is the viscosity coefficient which is set here to unity, and the total force $\mathbf{f}_i$ is the combination of the vortex-vortex interaction force $\mathbf{f}_i^{vv}$, the annealing force $\mathbf{f}_i^{T}$, the driving force (Lorentz force) $\mathbf{f}_i^{d}$ and the force due to the shielding currents and the edge $\mathbf{f}_i^{s}$ [44, 47, 49, 80, 81, 82]. Note that the disorder (*i. e.*, due to the intrinsic pinning) results in the overdamped regime of vortex motion. At the same time, disks are assumed to be free of artificial inclusions or holes (*i. e.*, artificial pinning centra) and thus the vortex-pin interaction has not been explicitly included in the equation of motion, Eq. (3.1) (cp. Refs. [80, 81, 82, 83, 47, 115, 116]). The thermal force $\mathbf{f}_i^{T}$ obeys the following conditions:

In our simulations, the thermal force is only used during the annealing process when the system relaxes to the ground state. When studying the dynamics, the temperature is set to zero.

$$\langle \mathbf{f}_i^{T}(t) \rangle = 0, \tag{3.3}$$

and

$$\langle \mathbf{f}_i^{T}(t) \mathbf{f}_j^{T}(t') \rangle = 2\eta k_B T \delta_{ij} \delta(t - t'). \tag{3.4}$$

An applied current flows from the center of the disk to the edge (see Fig. 1.4), and thus the density of the current is inversely proportional to the radius ρ:

$$J(\rho) = \frac{I}{2\pi\rho d}, \tag{3.5}$$

where d is the thickness of the superconducting disk. Therefore, the Lorentz force acting on the outer vortex, *i. e.*, near the boundary, is much weaker than that acting on the inner one, *i. e.*, close to the center. To avoid divergency of the current density at the center, we introduced a cut-off radius $\rho_0 = 10^{-3} R$ (see Fig. 3.2(a)). Inside of the cut-off radius, the density of the current was assumed to be

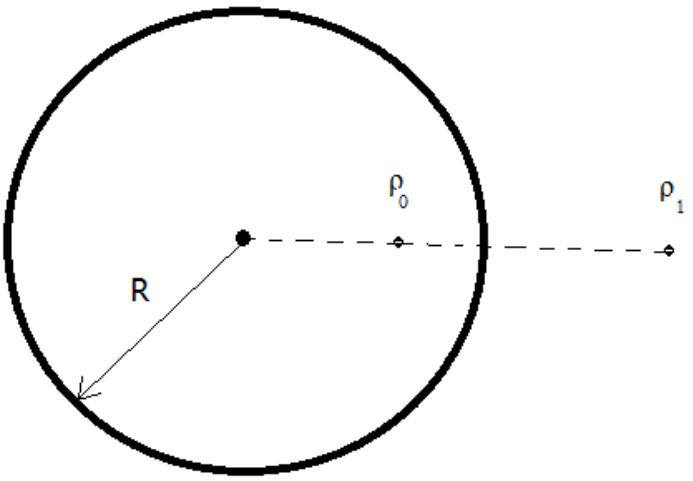

Figure 3.1: Vortex and its image. $\rho_1 = R^2/\rho_0$.

constant: $J_0 = J(\rho_0)$. The driving force (per unit length) due to the radial current is

$$\mathbf{f}_i^d = \frac{\Phi_0 I}{2\pi\rho_i d}\,\hat{\theta} = \frac{f_0 I_0}{r_i}\,\hat{\theta}, \tag{3.6}$$

where $r_i = \rho_i/R$ is the dimensionless distance from the center, $\hat{\theta}$ is the unit vector in the azimuthal direction in the disk plane,

$$f_0 = \Phi_0^2/(2\pi\mu_0 R\lambda^2) = 4\pi\mu_0\xi^2 H_c^2/R \tag{3.7}$$

is the unit of force, and

$$I_0 = \mu_0\lambda^2 I/(\Phi_0 d) = \mu_0\Lambda I/\Phi_0 \tag{3.8}$$

is the dimensionless driving current, *e.g.*, the dimensional value of the current $I = 0.1\mathrm{mA/m}$ is corresponding to $I_0 \approx 0.01$ in our simulations. Here R is the radius of the disk. We treat vortices as massless classical particles and assume that the motion of the vortices does not influence the distribution of the applied current density. Therefore, the driving force is always applied in the azimuthal direction, and thus no Hall effect is taken into account.

In a thin superconductor such that $\Lambda = \lambda^2/d \gg R \gg \xi \gg d$, the vortex-vortex interaction force $\mathbf{f}_{ik}^{vv}$ can be modeled by:

$$\mathbf{f}_{ik}^{vv} = f_0 \left(\frac{\mathbf{r}_i - \mathbf{r}_k}{|\mathbf{r}_i - \mathbf{r}_k|^2} - r_k^2 \frac{r_k^2 \mathbf{r}_i - \mathbf{r}_k}{|r_k^2 \mathbf{r}_i - \mathbf{r}_k|^2} \right). \tag{3.9}$$

where the first term on the right hand side (RHS) is the interaction between vortex i and vortex k and the second term on RHS is the interaction between vortex i and the image of vortex k which locates at position R^2/ρ_j ($1/r_j$ in dimensionless units) from the center of the disk. The image vortex (shown in Fig. 3.1) is used to fulfill the boundary conditions for the superconducting current. Then, the sum of all the vortex-vortex interaction forces exert on vortex i gives the total interaction force $\mathbf{f}_i^{vv}$ [33, 34, 44]:

$$\mathbf{f}_i^{vv} = f_0 \sum_k^L \left(\frac{\mathbf{r}_i - \mathbf{r}_k}{|\mathbf{r}_i - \mathbf{r}_k|^2} - r_k^2 \frac{r_k^2 \mathbf{r}_i - \mathbf{r}_k}{|r_k^2 \mathbf{r}_i - \mathbf{r}_k|^2} \right), \tag{3.10}$$

See the Appendix. A for details of the calculation.

and the force due to the vortex interaction with the shielding currents and the edge $\mathbf{f}_i^s$ is [33, 34, 44]:

$$\mathbf{f}_i^s = f_0 \left(\frac{1}{1 - r_i^2} - h \right) \mathbf{r}_i \tag{3.11}$$

with the dimensionless applied magnetic field $h = \pi R^2 \mu_0 H_0/\Phi_0 = (H_0/2H_{c2})(R/\xi)^2$. Here the first term on the RHS of Eq. 3.11 is due to the interaction between vortex i and its image outside of the disk, and the second term on RHS is due to the penetration of the magnetic field.

We use the term "ground state" in this work to denote the classical state with the lowest free energy following the previous papers, e. g., see Refs. [117, 118].

In our simulations, we first set $T > 0$, when no current is applied, and then gradually decrease temperature to let the system relax to the ground state (see Fig. 3.2(b)). In this way, we simulated the stimulated annealing process similar to that in annealing experiments [119, 120]. Then, we set $T = 0$ and apply the current to study the dynamics of the system of vortices.

3.2 VORTEX CONFIGURATIONS AND THEIR STABILITY

The system of many interacting vortices in a disk has many local minima corresponding to metastable states. We analyze the stability of different vortex configurations by calculating their free energy and probability of appearance.

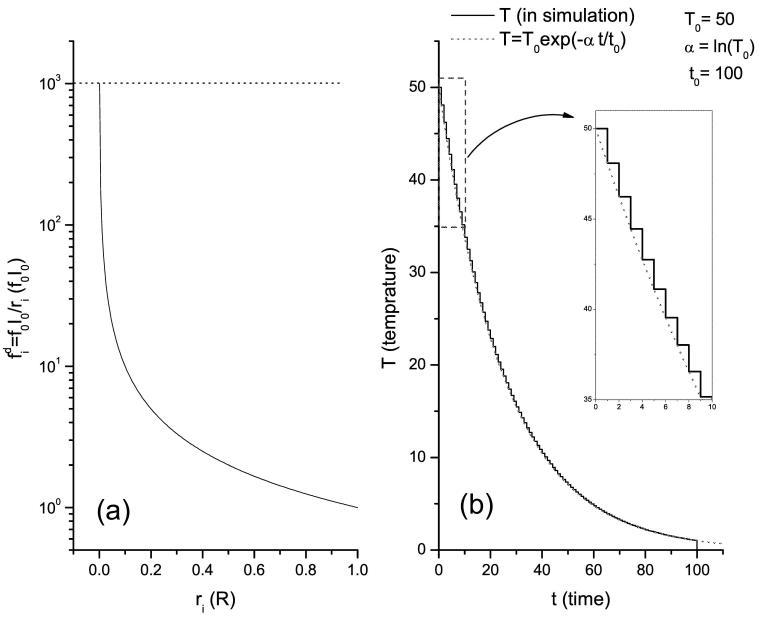

Figure 3.2: (a) The driving force with cut off close to the center; (b) The annealing process in our simulation. The total time of the annealing process is $t_0 = 100$ (*i.e.*, 100 MD steps).

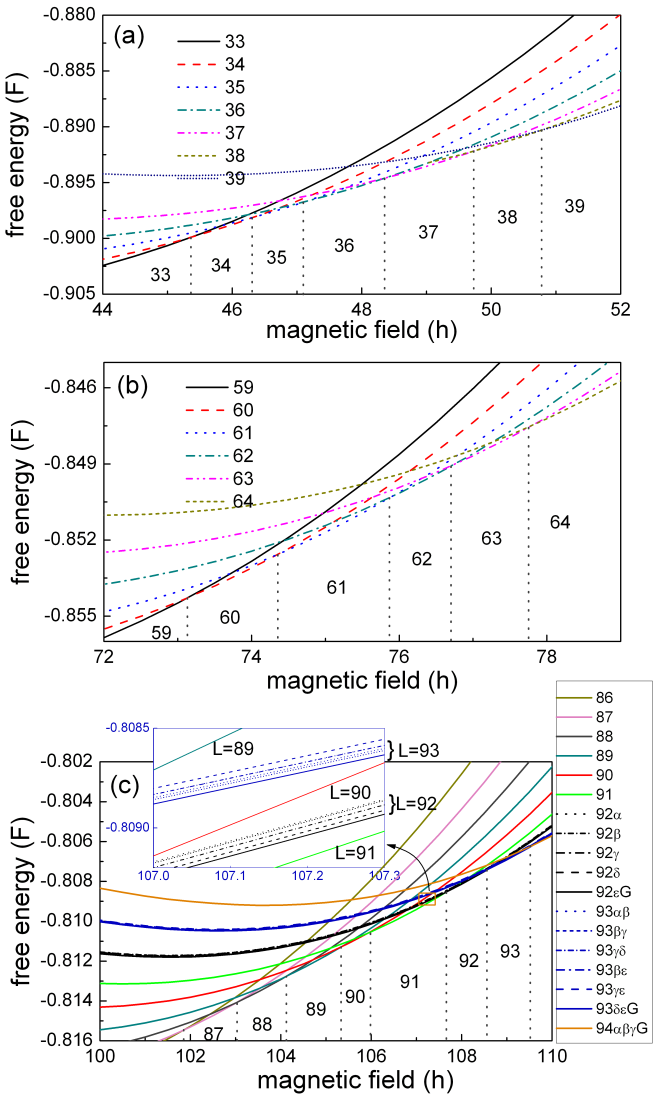

Figure 3.3: The energies of different vortex configurations with vorticities: a) $L = 33 - 39$; b) $L = 59 - 64$; c) $L = 86 - 94$. The ground state is denoted by the letter 'G' if there are several different configurations with the same L in (c) and these configurations are distinguished by using Greek letters 'α'($i = 1$), 'β'($i = 2$), 'γ'($i = 3$), 'δ'($i = 4$), 'ε'($i = 5$), which denote the ith shell with $6i + 1$ vortices (*i.e.*., shell S^i_{6i+1}) while the others have $6i$ vortices (*i.e.*, shell S^i_{6i}), respectively. Here S^i_j is introduced to denote the ith shell which contains j vortices. The difference in energy between two configurations with different vorticities L is much larger than that between two configurations with the same L as is illustrated by the inset of (c). The regions of magnetic field where the ground-state-energy configuration is provided by the same L are separated by vertical black dotted lines.

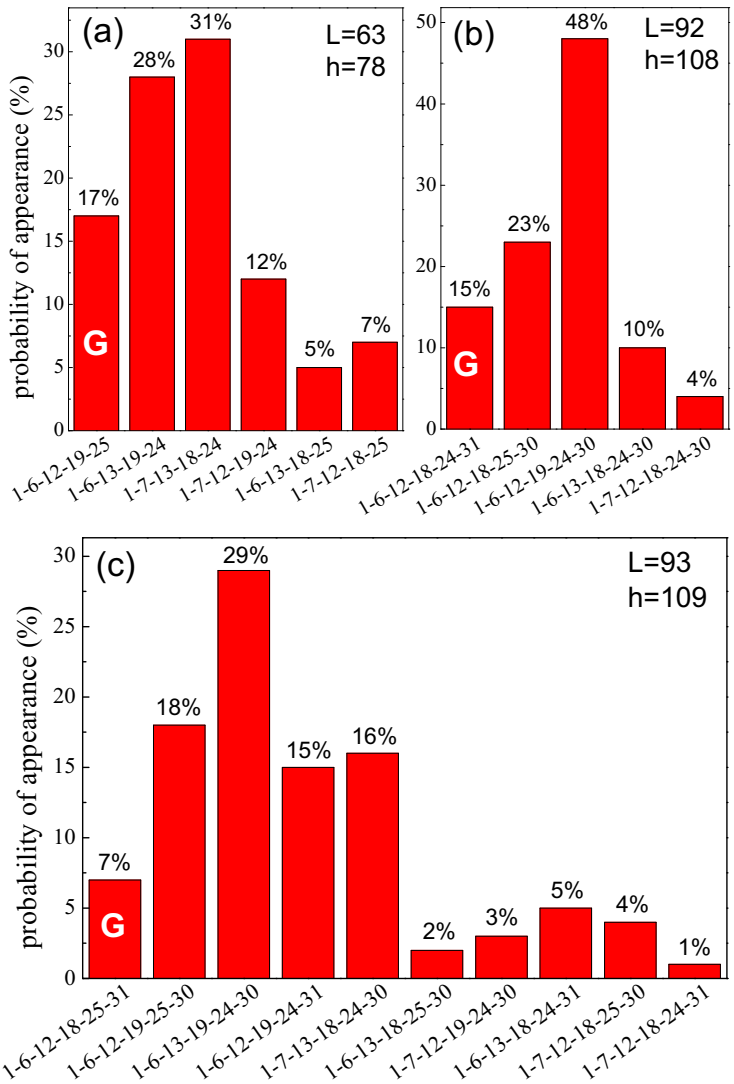

Figure 3.4: The probability of the appearance of different vortex configurations with vorticity L = 63 (a), L = 92 (b), and L = 93 (c). The most probable state is not always the ground state (denoted by "G") . For instance, for L = 63, the ground state is (1-6-12-19-25) with probability 17%, which is smaller than the probabilities of states (1-6-13-19-24) and (1-7-13-18-24).

For vorticity (*i. e.*, the number of vortices in a disk) $L > 5$, the ground state and metastable configurations of vortices in mesoscopic disks have been found both in simulations [34, 47] and in experiments [48]. To find the ground state at different magnetic field H_0, we calculated the improved London free energy [35]:

Note that the Gibbs free energy $\mathscr{F} = U - MB$ does not contain the entropic term TS because in our simulations $T = 0$.

$$\mathscr{F} = \mathscr{F}_L + \mathscr{F}_{core} \tag{3.12}$$

with

$$\mathscr{F}_L = \sum_{i=1}^{L} \left(\epsilon_i^{self} + \epsilon_i^{shield} + \sum_{j=1}^{i-1} \epsilon_{ij} \right) + \epsilon^{core} + \epsilon^{field}$$

$$\mathscr{F}_{core} \approx -1 + L\frac{3}{R^2} \tag{3.13}$$

where the energy is measured in units of $\frac{\Phi_0^2}{4\pi\mu_0\Lambda} \cdot \left(\frac{R}{2\xi}\right)^2 = H_c^2 V/2\mu_0$. For example, for $\Lambda = 100\mu m$, the energy in Fig. 3.3 is of the order of 100K. Therefore, the difference between various-L configurations would be of the order of the magnitude of 0.1K and the energy difference between same-L configurations would be around 0.01K. This London energy, Eq. (3.12), contains two parts. One is the usual London energy and the other one is related with the vortex cores contribution. When $\kappa \gg 1$, the vortex cores do not overlap and $\Lambda = \lambda^2/d \gg \xi, \gg d$, we obtain the usual London energy $\mathscr{F}_L$. However, the usual London limit neglects the spatial variation of $|\Psi^2|$. By introducing a function (which varies from 0 to 1 within the range $|\rho - \rho_i| \sim \xi$) to approximate the size of the vortex core, the contribution of the vortex cores have been taken into account. Assuming the vortex core has radius $\sqrt{2}\,\xi$, we obtain the contribution $\mathscr{F}_{core}$. Thus the improved London energy is the sum of these two contributions, which provide an agreement with the Ginzburg-Landau (GL) result as was shown in Ref. [35].

In our simulation, the radius of the disk is 50ξ, and the number of shells is not more than five. Therefore, roughly the distance between two vortices is larger than 8ξ, i. e., they are well separated.

Fig. 3.3 shows the free energy as a function of magnetic field in a disk with $R = 50\xi$. Note that the difference in the free energy between two states with different L is much larger than that between two different configurations with the same L (see the inset of Fig. 3.3(c)).

Analyzing the energies of different configurations with the same L, we find the range of magnetic field values in which the ground-state-energy configuration remains the same. For instance, the con-

figuration (1-6-12-19-25) with $L = 62$ has the lowest energy for $75.9 < h < 76.7$. Compared to the states of charged classical particles (CPs), the ground states (column "Ground-state(VC)") and the metastable states (column "MetaStable(VC)") with different L in disks with $R = 50\xi$, are listed in Table I.

Here we denote the configuration by linking the total vortex numbers in each shell with "-". E. g., 1-6-12-19-25 means that one vortex locates at the center and the 1st/2nd/3rd/4th shell has 6/12/19/25 vortices, respectively.

In order to find the probabilities of appearance of different meta-stable configurations, we performed a number (usually one hundred) simulations for the same L starting from different random initial vortex configurations. Although it may not cover all possible configurations, the statistic of one hundred simulations gives a rather representative sampling these stable configurations. In this way, the "most probable" vortex configuration (*i. e.*, the configuration with the highest probability of appearance) for a certain L is found. The probabilities are shown in Fig. 3.4 for different vortex states, for $L = 63$, 92, and 93. We find that the most probable configuration is *not* always the lowest energy state for given values of L. For instance, for $L = 92$, the state (1-6-12-19-24-30) is the most probable state (Fig. 3.4(b)) with 46% appearance, while the ground state (1-6-12-18-24-31) is found in only 15% of the cases. Previously similar results were found in the case of small disks [47] which was explained as due to the fact that the ground state is reached through a narrower minima in configuration space while the most probable state corresponded to a broader local minimum that is separated from the ground state by an energy barrier. Note that in principle, when the annealing is slow enough and the number of initial random realizations is large enough such that the *whole* configurational space (*i. e.*, all possible vortex configurations) is covered, the "lowest-energy" and the "most probable" states should coincide. However, in reality, this would require very extensive and thus very slow simulation runs for finding just initial vortex distributions. The fact that the "most probable" state does not coincide with the lowest-energy state means that this state is a metastable state with an energy very close to the energy of the ground state configuration. Importantly, this way of finding the initial vortex configuration has a direct experimental realization when a hundred (or two to three hundreds) identical disks are measured at the same conditions and then the statistics of different states is analyzed (see Refs. [48, 49]). Thus, by finding the most probable state we simulate the experimental conditions [48, 49].

We find that some of these most probable states exhibit interesting dynamical behavior which will be discussed in the following section.

Table 3.1: The ground-state and metastable vortex configurations (VC) in a disk with $R = 50\xi$, and the ground-state and metastable-state of classical particles (CPs) [52, 121]. A typical value of magnetic field h corresponding to the ground state is also given.

L	h	Ground-state(VC)	Metastable-state(VC)		Ground-state(CPs)*	Metastable-state(CPs)*		
33	45	5-11-17	1-5-11-16		1-6-11-15	1-5-11-16	1-6-10-16	
34	46	1-5-11-17	5-12-17	6-11-17	1-6-12-15	1-6-11-16	1-7-11-15	1-5-11-17
35	47	1-5-12-17	1-5-11-18		1-6-12-16	1-6-11-17	1-7-11-16	1-6-13-15
36	48	1-6-12-17	1-6-11-18	1-5-12-18	1-6-12-17	1-7-12-16	1-6-13-16	1-7-13-15
37	49	1-6-12-18			1-7-12-17	1-7-13-16	1-6-13-17	
38	50	1-6-12-19	1-6-13-18		1-7-13-17	2-7-13-16	2-7-12-17	1-7-14-16
39	51	1-6-13-19	1-7-12-19		2-7-13-17	1-7-13-18	1-7-14-17	2-7-14-16
61	75	1-6-12-18-24	1-7-12-18-23					
62	76	1-6-12-19-24	1-6-13-18-24	1-7-12-18-24				
63	77	1-6-12-19-25	1-6-13-19-24	1-7-13-18-24				
64	78	1-7-13-19-24	1-7-13-18-25					
90	106	1-6-12-18-24-29						
91	107	1-6-12-18-24-30						
92	108	1-6-12-18-24-31	1-6-12-18-25-30	1-6-12-19-24-30				
			1-6-13-18-24-30	1-7-12-18-24-30				
93	109	1-6-12-18-25-31	1-6-12-19-25-30	1-6-13-19-24-30				
			1-7-13-18-24-30	1-6-13-18-24-31				
94	110	1-7-13-19-24-30	1-6-13-19-25-30	1-6-13-19-24-31				

* Results of Refs. [52, 121].

We define the average velocity of all vortices in the ith shell as the "angular velocity of the ith shell", ω_i. The angular velocity of each shell $\{\omega_i | i = 1, 2, ...\}$ is calculated as a function of the applied current I_0, *i. e.*, $\omega(I_0)$ curves will be plotted.

Because the Lorentz force, *i. e.*, the driving force f^d, is maximum at the center of the disk and reduces as $1/\rho$ along the radius, one can expect that inner shells unlock first, *i. e.*, angular melting starts at the center and propagates towards the periphery. This behavior is indeed realized in macroscopic disks. However, in mesoscopic disks with a shell structure the process of angular melting is more complex due to commensurability/incommensurability between the shells resulting in different scenarios of angular melting. We discuss these different scenarios below.

This "angular melting," or consequent unlocking of vortex shells, can be induced either by temperature or by shear (i. e., *shear-induced plastic deformation). In the latter case, it is similar to the "shear-induced melting transition" in colloidal crystals.*

3.3.1 *Commensurability and angular melting*

The shells are called commensurate when the numbers of vortices in those shells are commensurate, *i. e.*, they have a common divisor [122]. Commensurate vortex shells usually contains $6i$ vortices where i is an integer. These shells are strongly locked because of a relatively larger energy barrier due to the interaction with the vortices in adjacent shell(s) resulting in a larger inter-shell "friction" , and thus a larger shear stress is required to unlock them than in the case of incommensurate shells which can easily slide with respect to each other (see Fig. 3.5). To illustrate the effect of commensurate and incommensurate shells, we consider here disks with vorticity $L = 38$, which represent typical configurations with small vorticity having both commensurate and incommensurate shells. We find three (meta)stable configurations for $L = 38$ which are (1-7-12-18), (1-6-13-18), and (1-6-12-19). We introduced S_j^i to denote the ith shell which contains j vortices. For example, shell S_7^1 of the configuration (1-7-12-18), shell S_{13}^2 of the configuration (1-6-13-18) and shell S_{19}^3 of the configuration (1-6-12-19) are incommensurate shells. By studying the angular velocities of shells, we find that incommensurate shells split off at lower driving force (shown in Fig. 3.6), as one intuitively expects.

Shell S_7^1 (Fig. 3.6(a)) splits off first due to both a larger gradient of the Lorentz force and a weaker friction (*i. e.*, a smaller energy barrier) with the incommensurate adjacent shell S_{12}^2. However, while

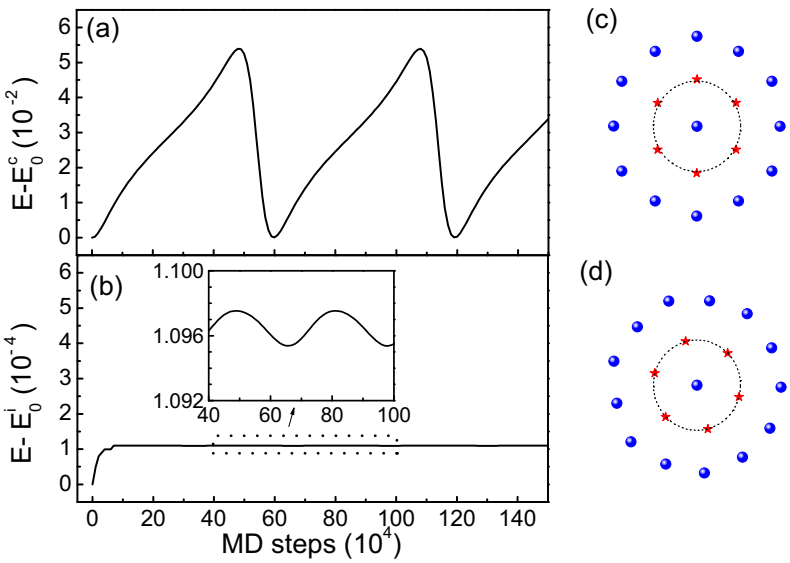

Figure 3.5: The energy barriers produced by vortices of the outer shell: a) in commensurate case and b) in incommensurate case. The configurations with two commensurate (*i. e.*, (1-6-12)) and incommensurate shells (*i. e.*, (1-6-13)) are shown in (c) and (d), respectively. All vortices of the inner shell (red stars) rotate with respect to the outer shell (blue balls) due to the driving force. The interaction energy between the inner shell and the outer shell E is calculated for both cases. Here $E_0^c(E_0^i)$ is the interaction energy of the ground state in the commensurate (incommensurate) case. The energy barrier in (a) is much larger than that in (b); notice also the factor 10^2 difference in scale. Therefore, when the shells are commensurate, the inner shell must overcome a larger "friction" (due to the energy barriers) to rotate individually.

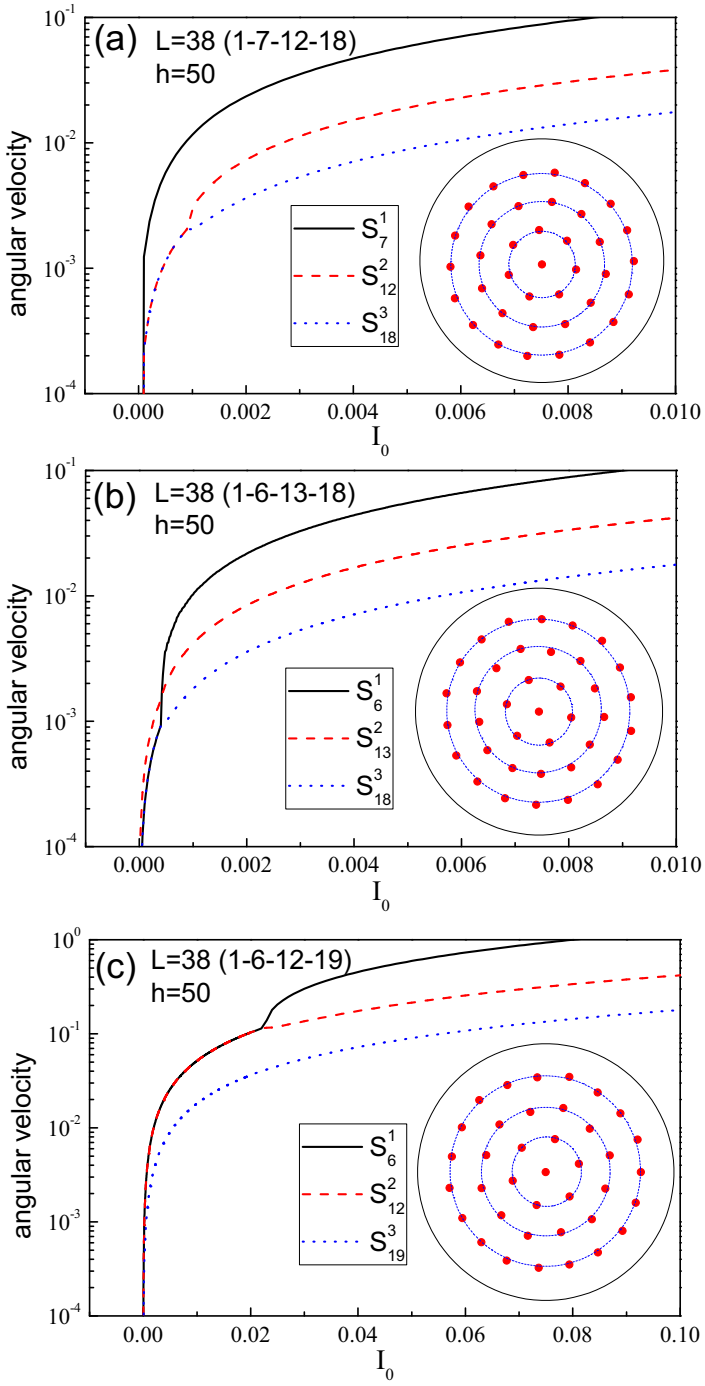

Figure 3.6: The angular velocities of shells in different configurations with L = 38: (1-7-12-18) (a); (1-6-13-18) (b); and (1-6-12-19) (c). The angular melting first occurs in the incommensurate shell due to a weaker friction. Different scenarios of angular melting, *i. e.*, the first unlocking of different shell occurs in: a) the innermost shell S_7^1, b) the middle shell S_{13}^2 or c) the outermost shell S_{19}^3.

shell S_6^1 (Fig. 3.6(c)) experiences a larger gradient of the Lorentz force, it also has a stronger friction due to the commensurate adjacent shell S_{12}^2. Therefore, there is a competition between the gradient driving force and the commensurability effect (which determines friction between adjacent shells). Our calculations show that often commensurability plays a more important role than the local gradient force, resulting in an unusual (unconventional) dynamical process. Angular melting can occur first in regions of *weaker* shear stress [55] because of a relatively weaker friction. The commensurability effects in multi-shell vortex structures display themselves in a more complex way than in the case of just two (in)commensurate shells (chains). This can be illustrated by the vortex configuration shown in the inset of Fig. 3.6(b). Part of the vortices of the incommensurate shell S_{13}^2 adjust themselves to the commensurate core and thus this shell actually contains a hexagon-like part which is characterized by a relatively stronger friction with adjacent shell(s). As a result, the local shear modulus of that incommensurate shell is inhomogeneous and turns out to be angle-dependent. In this case, the outer commensurate shell(s) could be locked to the core via the hexagon-like part of the incommensurate shell (as, *e.g.*, shell S_{19}^3 for $L = 62$ in Fig. 3.7(a); see also Ref. [55]) and thus rotates with the same angular velocity as the core until the current reaches a critical value and unlocks the shells. Therefore, the effect of commensurability can even involve remote shells. This makes the process of angular melting in multi-shell vortex structures with incommensurate shells more complex.

Commensurate shells which contain $6i$ (i is a positive integer) vortices tend to form locally a hexagonal arrangement of vortices similar to a triangular Abrikosov lattice. On the other hand, due to the circular confinement the outermost shell is forced into a shape close to a circle. There is a transition region from the triangular Abrikosov lattice at the center to the circle shell close to the boundary [123]. It is clear that two adjacent circle-like shells (or out of those shells at least one is circle-like) can slide much easier with respect to each other than two adjacent shells that are arranged in a hexagon-like configuration. This explains the above effect of unusual angular melting starting near the boundary and propagating towards the center with increasing applied current.

3.3.2 *Inverse angular velocities*

Due to the radially-decreasing driving force, outer shells are expected to rotate slower than inner ones, except in the rigid body regime where all shells rotate together with the same angular velocity. However, we found that for certain configurations and in specific ranges of current that the angular velocity becomes *inverse*, *i. e.*, a ith shell with radius r_i rotates with a larger angular velocity than the inner adjacent shell $i-1$ with radius $r_{i-1} < r_i$. For example, in case of $L = 38$ (1-6-13-18) shell S^2_{13} has the largest angular velocity when it unlocks while shells S^1_6 and S^3_{18} still rotate together (shown in Fig. 3.6(b)). Such unusual dynamical behavior is caused by the mismatch between shells along the azimuthal direction, in particular, when there are incommensurate shells (usually containing $6i+1$ vortices) between two commensurate shells, and we will call this an "intra-shell defect".

As compared to the configuration where all shells are commensurate (*i. e.*, the magic-number configuration (MNC) [52, 124, 122]), an intra-shell defect breaks up the six-fold symmetry of the shell and makes the part of the shell with defect "circle-like" (*e. g.*, the left part of shell S^3_{19} in Fig. 3.7(a)). The additional vortex shifts other vortices of the shell from their stable triangle-like-lattice positions. Fig. 3.7(a) shows the difference between $L = 62$ (1-6-12-19-24) and $L = 61$ (1-6-12-18-24), *i. e.*, configurations with and without defect, correspondingly. The angular velocity of each shell is shown in Fig. 3.7(b). Because of the incommensurability, shell S^3_{19} splits off first and rotates "individually" (shown in Fig. 3.7(c)) while all other shells rotate with the same angular velocity. With increasing current, the commensurate shells start to unlock one by one. Commensurability can still explain the above behavior: the friction between incommensurate shell S^1_{19} and the adjacent shells is weaker than that between other shells, and shell S^1_{19} can relatively easily slide with respect to the other shells.

For completeness we also calculated the angular velocities for disks which contain two or more defect-shells, *e. g.*, $L = 63$ (1-6-12-19-25) and $L = 93$ (1-6-12-19-25-30) which are shown in Fig. 3.8. Analyzing this unusual dynamical behavior, we concluded that it cannot be explained only by commensurability. Therefore, a two-step angular-melting process has to be invoked in order to explain the inverse angular velocity behavior for the transition from rigid-body rotation ($\nu \sim \rho$) to individual rotation of shells ($\nu \sim 1/\rho$). Hence, we define three regimes of vortex dynamics:

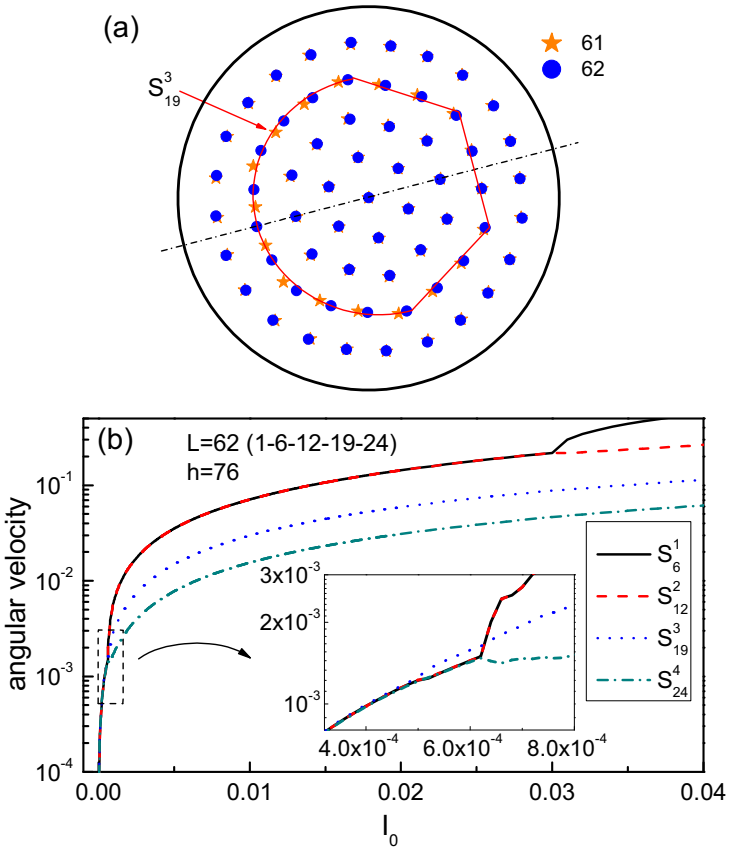

Figure 3.7: a) Comparison between the configurations L = 61 (1-6-12-18-24) and L = 62 (1-6-12-19-24); b) the angular velocities of shells for magnetic field h = 78 with L = 62 (1-6-12-19-24); c) the magnified image of (b). Because of an extra vortex in shell S^3_{19} (*i. e.*, shell S^3_{19} is incommensurate) the friction between the adjacent shells S^2_{12} and S^4_{24} is small. Therefore, shell S^3_{19} can easily slide between the adjacent shells.

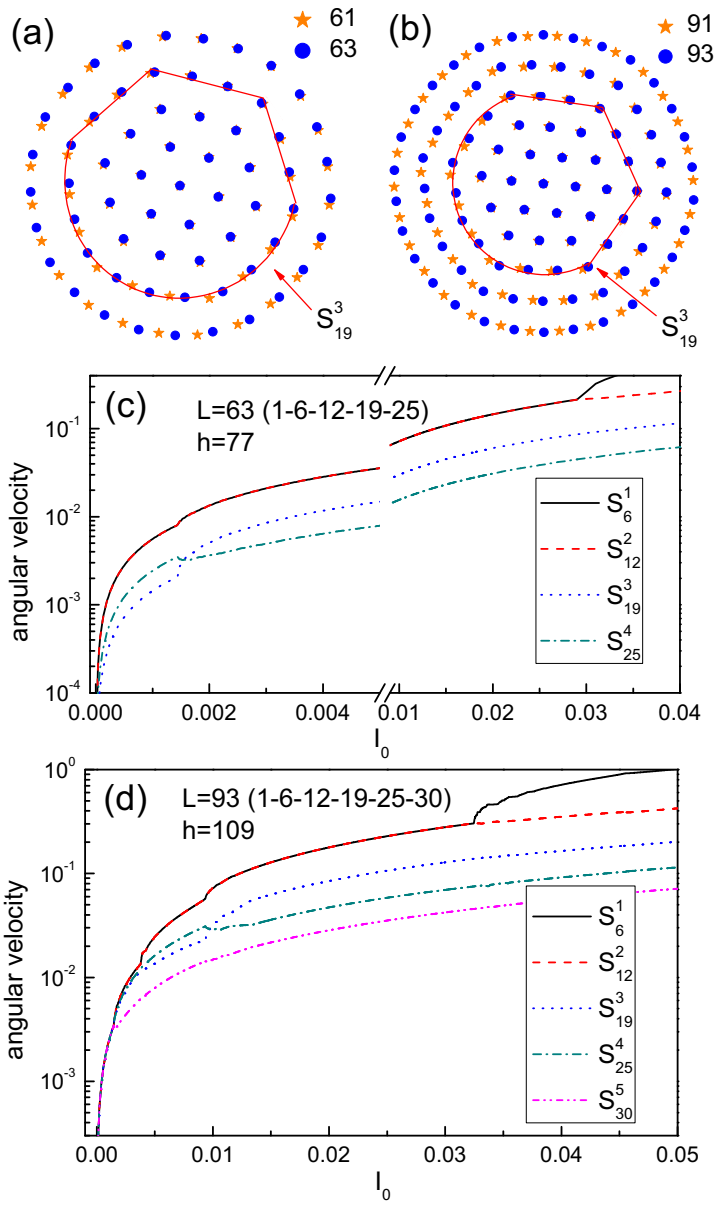

Figure 3.8: Comparison between the configurations: a) (1-6-12-18-24) for L = 61 and (1-6-12-19-25) for L = 63; b) (1-6-12-18-24-30) for L = 91 and (1-6-12-19-25-30) for L = 93, and the angular velocities of shells with c) (1-6-12-19-25) for L = 63 and d) (1-6-12-19-25-30) for L = 93. As shown here, the angular velocity of shell S^3_{19} is smaller than that of shell S^4_{25} when $I_0 < 0.0015$ (c) and when $0.005 < I_0 < 0.009$ (d). However, shell S^3_{19} experiences a larger Lorentz force than shell S^4_{25} in both cases. Thus, the angular velocities of shells S^3_{19} and S^4_{25} are opposite to the gradient of the Lorentz force in these regimes, *i.e.*, there is an inversion of the velocity of these two shells with respect to the usual case.

I. Rigid Body Motion. When the current is small, the gradient of the driving force is too small to overcome friction (due to the vortex-vortex interaction). All vortices rotate together as a rigid body.

II. Compression-decompression Motion. For a larger applied current, incommensurate shells slide with respect to the other shells. On the one hand, the local shear modulus of the circle-like part of the defect shell is too small to keep the outer shell(s) rotating together with the inner shells. On the other hand, the gradient of the driving force is not large enough to overcome the friction between the hexagon-like part of the defect shell and its adjacent commensurate shell. In this case, the incommensurate (defect) shell is *partly* angular melted. The vortices of the melted part participate in an inhomogeneous slow motion, which releases a part of the vortices in that shell from the circle-like positions to their triangular-lattice positions and pushes another part of vortices away from their lattice positions. Such kind of compression-decompression motion (see Fig. 3.9) modifies the local density of vortices in the defect shell and finally results in a longitudinal wave-like propagation in the defect shell.

III. Laminar Motion. The shells finally acquire "individual" velocities over a certain value of current when the Lorentz force can overcome the friction. It means that the vortex lattice is totally angular-melted. Note that the shells still remain well-distinguished, *i. e.*, vortices do not jump from one shell to the others. The latter would mean the onset of radial melting [44, 52, 53, 54].

The above regimes, except the second regime, have been discussed in previous subsections. Inversion of angular velocities only occurs when the shells display "compression-decompression motion". For instance, we consider the configuration (1-6-12-18-25-31) for $L = 93$. Shell S^4_{25} and shell S^5_{31} split off first as expected (shown in Fig. 3.10) because of incommensurability. However, shell S^4_{25} has the smallest angular velocity until the current reaches the value I^*_c. The motion of shell S^4_{25} and shell S^5_{31} is considered as the combination of the rigid body motion with the core (*i. e.*, the inner shells forming a rigid MNC) and the relative slow motion with respect to the core. The velocities of shells S^4_{25} and S^5_{31} can be expressed by the following formula:

$$v_i = \omega_i r_i = \omega_c r_i + \Delta v_i \quad (i = 4, 5), \tag{3.14}$$

where ω_c is the angular velocity of the core, r_i is the radius of the ith shell and Δv is the linear velocity of the compression-decompression

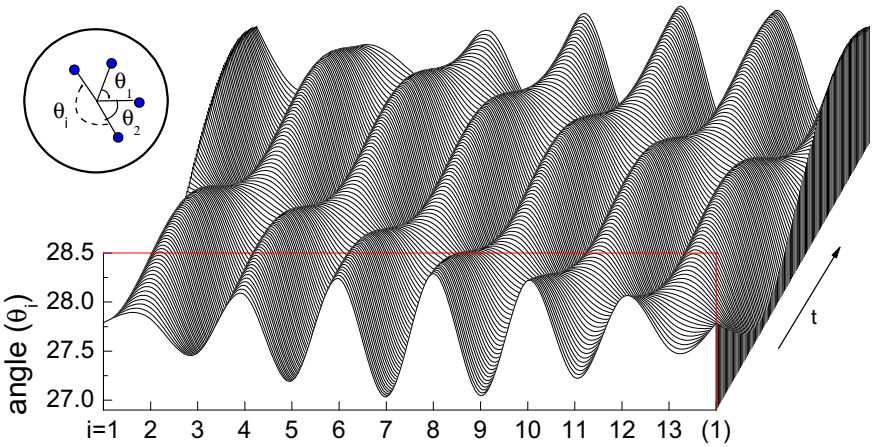

Figure 3.9: The evolution of the angle (θ_i) between two neighbor vortices in the incommensurate shell. The plot shows that the compression part (*i.e.*, characterized by a relatively smaller angle θ_i) propagates along the shell. The compression part is followed by the decompression part resulting in a propagating compression-decompression wave.

wave. The same linear velocity ($\Delta v_4 = \Delta v_5$) was found for shells S^4_{25} and S^5_{31} in the regime of "compression-decompression motion", which become different for $I > I^*_c$ (shown in the inset of Fig. 3.10). Even in the case of several defect shells and for defect shells which are near the center of the disk, we find that the vortices of defect shells have the same Δv in that regime (*e.g.*, $L = 94$ is shown in Fig. 3.11). The compression-decompression wave of those defective shells (S^4_{25}, S^5_{31}) have the same Δv. As seen from Fig. 3.12, the configuration shown by filled blue (dark gray) circles and the empty yellow (light gray) stars form the same configuration (1-6-12-18-25-31) rotated by 180°. The vortices of the two outer shells have to move only a small distance with respect to the core in order to restore the same initial configuration after rotation. The distance between two adjacent vortices d_0 is nearly the same and each vortex of the shells S^4_{25} and S^5_{31} has to slide over d_0 when the symmetry axis is rotated over 360°. Hence, we obtain nearly the same relative linear velocities of the shells until the current becomes large enough to make the shells move "individually".

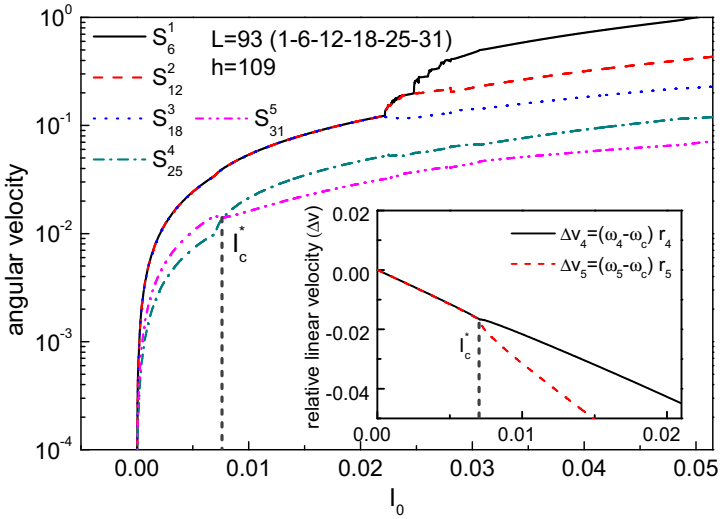

Figure 3.10: The evolution of angular velocities of shells with $L = 93$ (1-6-12-18-25-31). The inset shows the relative linear velocities of S^4_{25} and S^5_{31} (*i.e.*, the linear velocities of the relative backwards motion with respect to the core part of the vortex configuration). The relative linear velocities are nearly the same until the current reaches the critical value I^*_c.

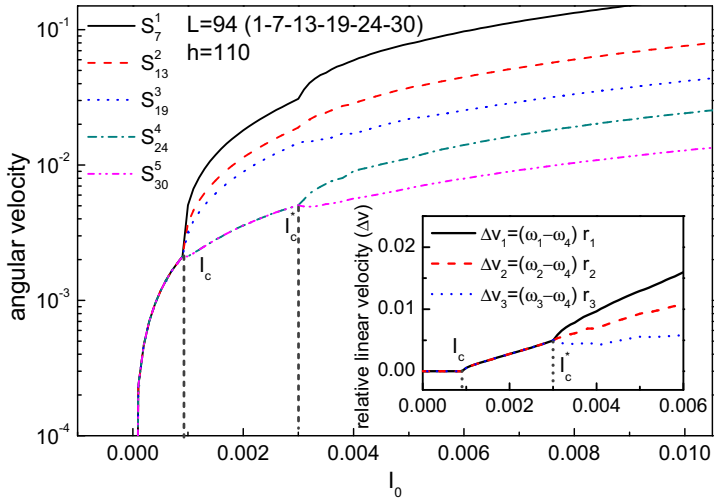

Figure 3.11: The evolution of angular velocities of shells with $L = 94$ (1-7-13-19-24-30). The inset shows that the relative linear velocities of S^1_7, S^2_{13} and S^3_{19} with respect to the outer shells are the same until the outer shells unlock.

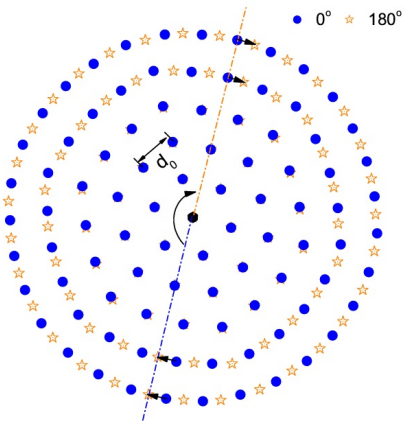

Figure 3.12: The filled blue (gray) circles and the empty yellow (light gray) stars show the locations of vortices before and after rotation over 180°, for L = 93 (1-6-12-18-25-31).

3.3.3 *Hysteresis effect*

We investigated also a very different configuration with several inter-shell vortices, for instance L = 89 (1-6-12-18=23=29) (see inset of Fig. 3.13). Here, we have another kind of defect, called "inter-shell defect", which always locks three or more shells, *e.g.*, shells S^3_{18}, S^4_{23} and S^5_{29} in configuration (1-6-12-18=23=29) are locked until $I_0 > 0.014$, where the locking of shells is represented by the symbol "=" instead of "-" . Once unlocked, all the shells rotate separately under the action of the applied current.

The configuration L = 89 in the absence of any applied current is shown in the inset of Fig. 3.13. It is nearly six-fold symmetric except for the outermost shell which is almost a circle due to the effect of the boundary. However, vortex rows become aligned along a straight line (shown by the blue (dark gray) lines in the inset of Fig. 3.13), *i.e.*, along one of the symmetry axes. One of these rows is longer than the others and locks the three outer shells for $I_0 < I_c$ and all the vortices rotate as a rigid body (shown in Fig. 3.14(a)). For $I_0 > I_c$, vortex 'D' (shown in the inset of Fig. 3.13) jumps to the middle shell (S^3_{17+D}) and the outermost vortex next to it is pushed into the outermost shell (S^5_{29}). These opposite radial movements of vortices in the row with a defect (Fig. 3.14(b)) finally rearrange the vortices into a well-defined shell-structure (*i.e.*, "dynamical ordering"). Although the gradient of the Lorentz force in the central part of the disk is not large enough to break the rigid-body motion of

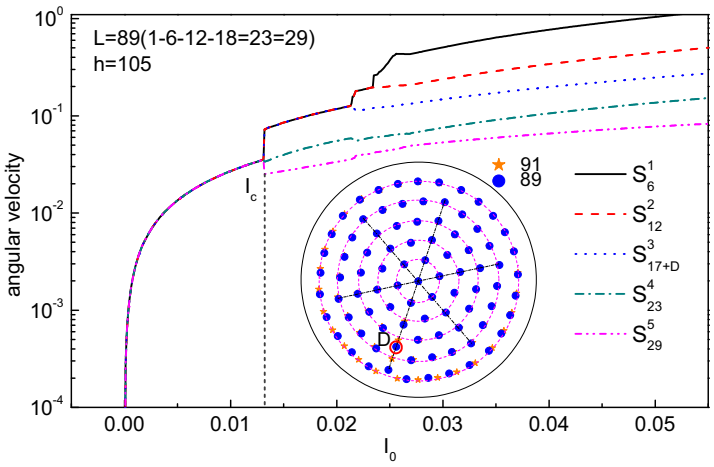

Figure 3.13: The average angular velocities of shells versus driving current I_0. When $I_0 > I_c$, the inter-shell vortex 'D' jumps into the middle shell (S_{17}^3).

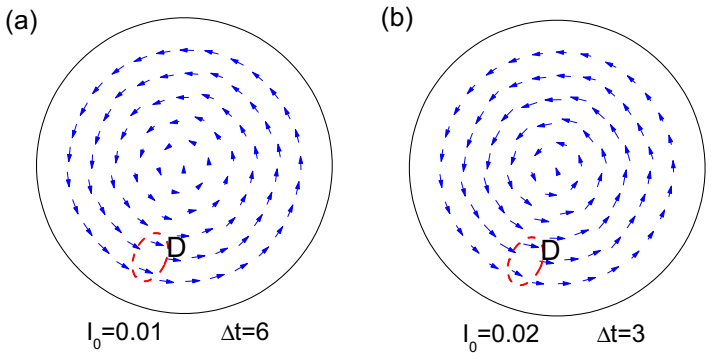

Figure 3.14: The vortex displacements with L = 89 for: a) driving current $I_0 = 0.01$, total time $\Delta t = 6$ (6000 MD steps), and b) driving current $I_0 = 0.02$, total time $\Delta t = 3$. When $I_0 < I_c$, the inter-shell vortex 'D' stays between two shells (S_{17}^3 and S_{23}^4). When $I_0 > I_c$, the inter-shell vortex 'D' jumps to the middle shell S_{17}^3.

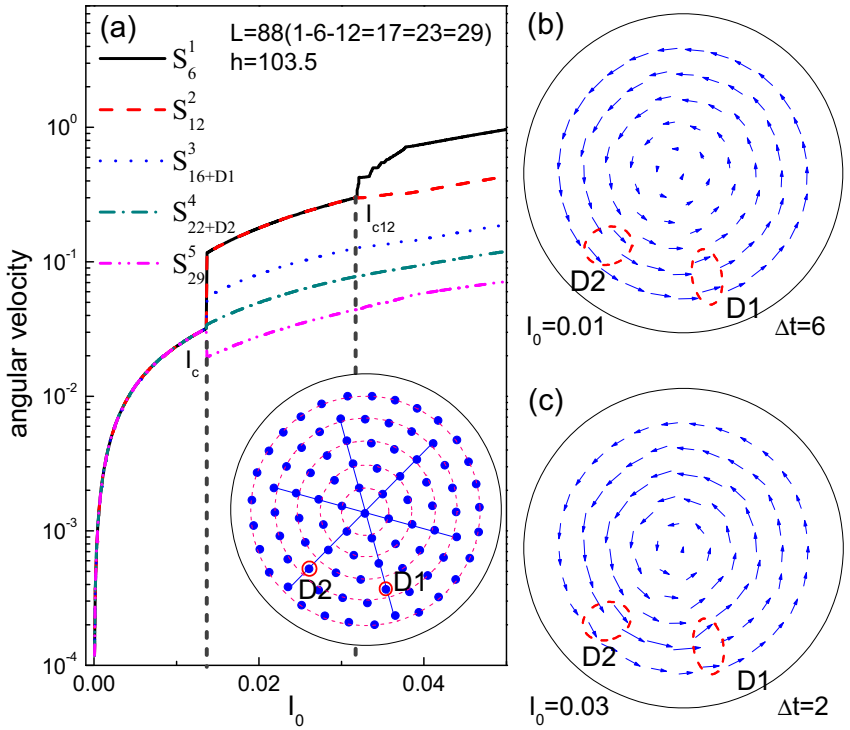

Figure 3.15: a) The configuration and the average angular velocities of the different shells versus driving current I_0; The vortex displacements with L = 88 for: b) driving current $I_0 = 0.01$, total time $\Delta t = 6$ (6000 MD steps) and c) driving current $I_0 = 0.03$, total time $\Delta t = 2$. The defects are marked by the small dashed rings. When $I_0 > I_c$, the inter-shell vortex 'D1' jumps to the middle shell S^3_{16} and the inter-shell vortex 'D2' jumps to the shell S^4_{22}.

the core (1-6-12), it is sufficient to overcome the friction among all of the locked shells S^3_{17+D}, S^4_{23}, and S^5_{29}.

For the configuration (1-6-12-17=23=29) with L = 88, we find that another inter-shell defect appears along another symmetric axis (the blue (dark gray) line in Fig. 3.15(a)). With increasing driving force, vortex 'D1' moves to the middle shell (S^3_{16}) while vortex 'D2' moves to the second outer shell (S^4_{22}) (Fig. 3.15(b)). Finally, the inter-shell defects disappear and all the vortices are arranged in the five-shell structure ($S^1_6, S^2_{12}, S^3_{17}, S^4_{23}, S^5_{29}$) when $I_0 > I_c$. The driving force then is large enough to unlock all the locked shells S^3_{17}, S^4_{23} and S^5_{29}, however, the core (1-6-12) is still stable and rotates as a rigid body.

For $I_0 < I_c$, the driving current is unable to destroy the radial vortex line(s) with defects. All the vortices rotate in the rigid-body mode. When the vortex system has transited from the static stable state to the dynamic steady state (with a well-defined shell structure), the system will not collapse into the static stable state immediately if we slightly decrease I_0 below I_c (see Fig. 3.16). However, with further decreasing I_0 (*i. e.*, $I_0 < I_c^-$), the dynamic state becomes unstable and the system returns to the static stable state, thus all the vortices have the same angular velocity. The critical current (I_c) to unlock S^3_{16+D1} and S^4_{22+D2} with increasing current is much larger than the critical current (I_c^-) when the system returns to the rigid body rotation with decreasing current. In this regime, for the same value of the applied current, we can have different distributions of angular velocities, *i. e.*, hysteresis in angular melting is found. The I_{c12} is the same for increased or decreased current (as shown in Fig. 3.16), therefore, there is no hysteresis behavior except for the shells which are locked by inter-shell defect(s). Namely, inter-shell defects are responsible for the hysteresis effect in the angular velocity.

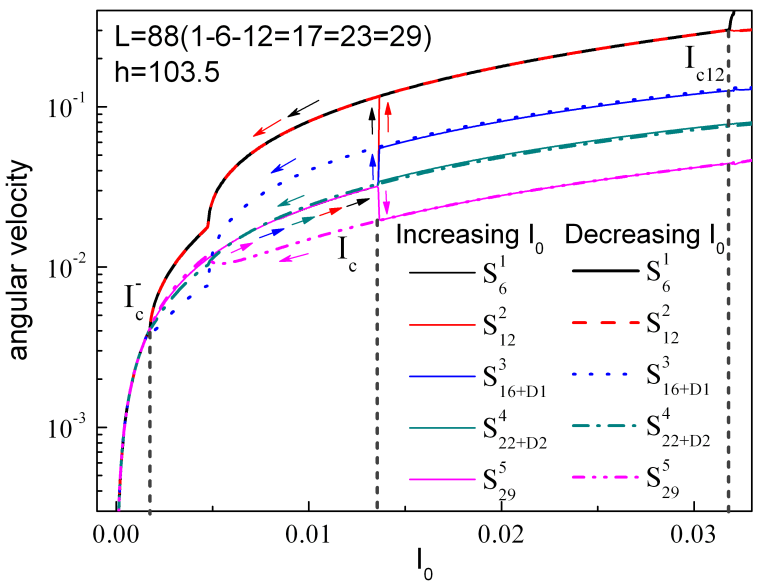

Figure 3.16: The angular velocities of the different shells when the driving current is increased (solid lines) or decreased (dashed lines of the same colors). I_c is the critical value for breaking the rigid body motion by increasing current while I_c^- is the critical current for returning to the rigid body motion when decreasing current. When the current is between I_c and I_c^-, the angular velocity of each shell is different when increasing and decreasing current (*i. e.*, the hysteresis effect of angular velocity).

4

RECTIFICATION OF VORTEX MOTION IN A CIRCULAR RATCHET CHANNEL

In this chapter, we study the dynamics of vortices in a circular channel formed by asymmetric triangular (funnel) cells (TCs) (see Fig. 4.1) [125, 126]. Due to the radially flowing current in a Corbino setup, the driving force is not uniform inside the cell which is different from linear ratchet channels. Such a geometry (*i. e.*, asymmetric in the azimuthal direction and in the radial direction), as will be shown, leads to a specific dynamical behavior, for example, a vortex located near the inner corner of a TC (which is closer to the center), experiences a stronger driving force and moves to the next TC while a vortex located near the outer corner of TC does not move. The circular geometry of the ratchet channel is convenient for studying commensurability and step-motor (phase locking) behavior [70, 73, 84]. We analyze in detail low and high density regimes of rectification, *i. e.*, "single-vortex" and "multi-vortex" regimes. We demonstrate that the mechanism of rectification are qualitatively different for these two cases. In addition, preliminary measurements were performed by the experimental group from Syracuse University [125] using a single nanofabricated weak-pinning ratchet channel of a-NbGe with strong-pinning NbN channel edges in a Corbino set-up. The measurements revealed a substantial asymmetric vortex response. Before discussing the results, let us first present the model of our systems.

Note that earlier this approach to form asymmetric channels in experiment (i. e., *using weak-pinning channels) was employed in a stripe geometry [63].*

4.1 MODEL AND SIMULATION

We consider a ring-like weak-pinning channel constructed of N partially overlapping TCs as shown in Fig. 4.1. In our simulations, the radius of the ring R is typically set as 6λ, where λ is the magnetic field penetration depth, the wider part of the channel (*i. e.*, the base of TCs) $w = 0.75\lambda$, and the width of the narrow part Δ (the neck)

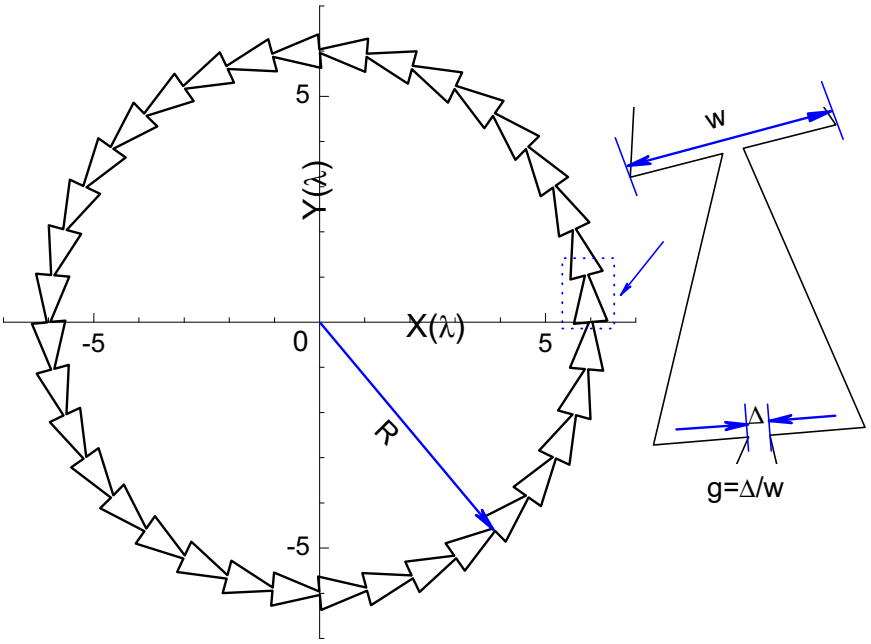

Figure 4.1: The geometry of the system. The widths of the wide part w and narrow part Δ are shown in the figure, where $g = \Delta/w$ is the ratio between the two parts. Here $g = 0.1$, the radius of the channel $R = 6\lambda$ and the channel is constructed by 36 TCs, *i. e.*, $N = 36$.

is typically 0.1 of the wider part (*i. e.*, the ratio $g = \Delta/w = 0.1$). We also performed simulations in a channel with a wider neck part, *e. g.*, $g = 0.15$, for comparison. The weak-pinning channel (where vortices can move freely) is surrounded by a strong-pinning superconducting material [130] which is modeled by a medium where vortices cannot move. An external current I radially flows from the center of the disk to the edge, resulting in the density of current $J(\rho) \sim I/\rho$. Therefore, the closer a vortex to the center of the disk, the stronger the Lorentz force that acts on it. We perform Langevin-type molecular dynamics (MD) simulations and numerically integrate the overdamped equations of motion:

Note that the viscosity coefficient varies in different superconductors, e. g., *in a-NbGe* $\eta \approx 10^{-8}$ *Ns/m*^{2} *[127]. Using this value of* η *in our calculations results in typical maximum values of vortex linear velocity* $v \approx 10^2$ *m/s (for a* 1μ*m-thick film) which is still below the Larkin-Ovchinnikov critical velocity [128, 129].*

$$\eta \frac{d\mathbf{r}_i}{dt} = \mathbf{f}_i \tag{4.1}$$

with

$$\mathbf{f}_i = \sum_j \mathbf{f}_{ij}^{vv} + \mathbf{f}_i^T + \mathbf{f}_i^d + \mathbf{f}_i^b, \tag{4.2}$$

where η is the dimensionless viscosity coefficient which is set here to unity. As mentioned in Chapter 3, the driving force due to the radial current is

$$\mathbf{f}_i^d = \frac{\Phi_0 I}{2\pi\rho_i d}\,\hat{\theta} = \frac{f_0 I_0}{r_i}\,\hat{\theta}, \tag{4.3}$$

and the thermal force obeys Eqs. 3.3 and 3.4 in Chapter 3 and the vortex interaction $\mathbf{f}_{ij}^{vv}$ is described as Eq. 3.10.

Comparing with 3.2, here we have the confining force due to the boundary $\mathbf{f}_i^b$ instead of the force due to the shielding currents and the edge $\mathbf{f}_i^s$, because the channel is far from the edge of the disk so that $\mathbf{f}_i^s$ is negligible. To model the vortex-boundary interaction, we assume an infinite potential wall at the boundary (*i.e.*, vortices cannot leave the channel) which decays inside the triangular cell with the same dependence on position as the vortex-vortex interaction potential. The total interaction of a vortex with the channel boundaries is calculated by integrating the vortex-wall interaction potential over the geometrical boundary of the channel. The resulting potential due to the boundary is shown in Fig. 4.2(b), and the vortex-boundary force $\mathbf{f}_i^b$ is directly calculated from the potential. Following the center line of the channel we can obtain a well-defined ratchet potential as shown in Fig. 4.2(a).

In order to get the ground state before we study the dynamical behavior of vortices, the temperature $T > 0$ is first set, when no current is applied, and then gradually decrease temperature to let the system to relax to the ground state as described in Chapter 3. Then we set $T = 0$ and apply an ac current with frequency ν and amplitude I_0 that results in oscillating Lorentz force and drives vortices, to study the dynamics of the system.

4.2 RECTIFICATION OF VORTEX MOTION

4.2.1 *Density of vortices*

The vortex density, *i.e.*, the number of vortices per TC, plays an important role in the dynamics of the system. For very low vortex density, the vortex-vortex interaction is small as compared to the interaction with the boundary, and therefore it can be neglected. With increasing the vortex density, the interaction between vortices becomes important. Therefore, we roughly distinguish two regimes,

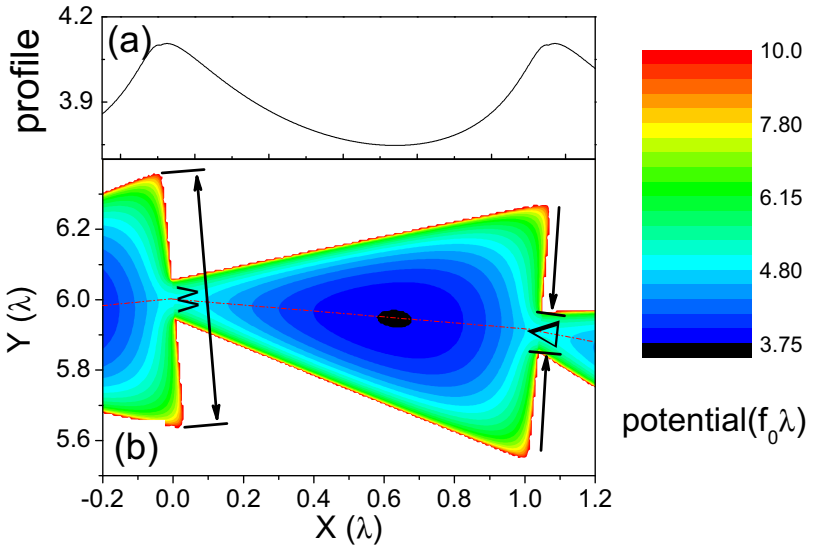

Figure 4.2: (a)The profile and (b) the contour map of the modeled potential. The lowest potential in a TC is close to the geometry center of the triangle and the potential near the boundary is high enough to prevent vortices from escaping the TC. The widths of the wide part w and narrow part Δ are shown in the figure (b), where the ratio between the two parts $\Delta/w = 0.15$. The radius of the channel $R = 6\lambda$ and the channel is constructed by 36 TCs.

i.e., a single-vortex regime and a multi-vortex regime, respectively, corresponding to low and high vortex density.

In order to characterize the dynamical behavior of the system of vortices, we calculate the net angular velocity of each vortex and take average over all the vortices for, *e.g.*, 100 ac periods. The resulting average angular velocity (called further "angular velocity") is denoted as ω which is analyzed for different parameters of the system and drivings. Note that angular velocity is related in a straightforward way to the flux-flow voltage [130, 37] which can be measured in experiment.

One system contains L vortices and N triangles in a circular chain, *e.g.*, in our simulations we take $N = 36$. If there is less than one vortex per cell, *i.e.*, $L < 36$ in our system (see Fig. 4.1), then the density of vortices is low enough and one can neglect the interaction between vortices. One can imagine that all the vortices are far away from each other and weakly interact with other vortices but they are strongly influenced by the ratchet potential induced by the boundary. Therefore, the dynamical behavior in the low density

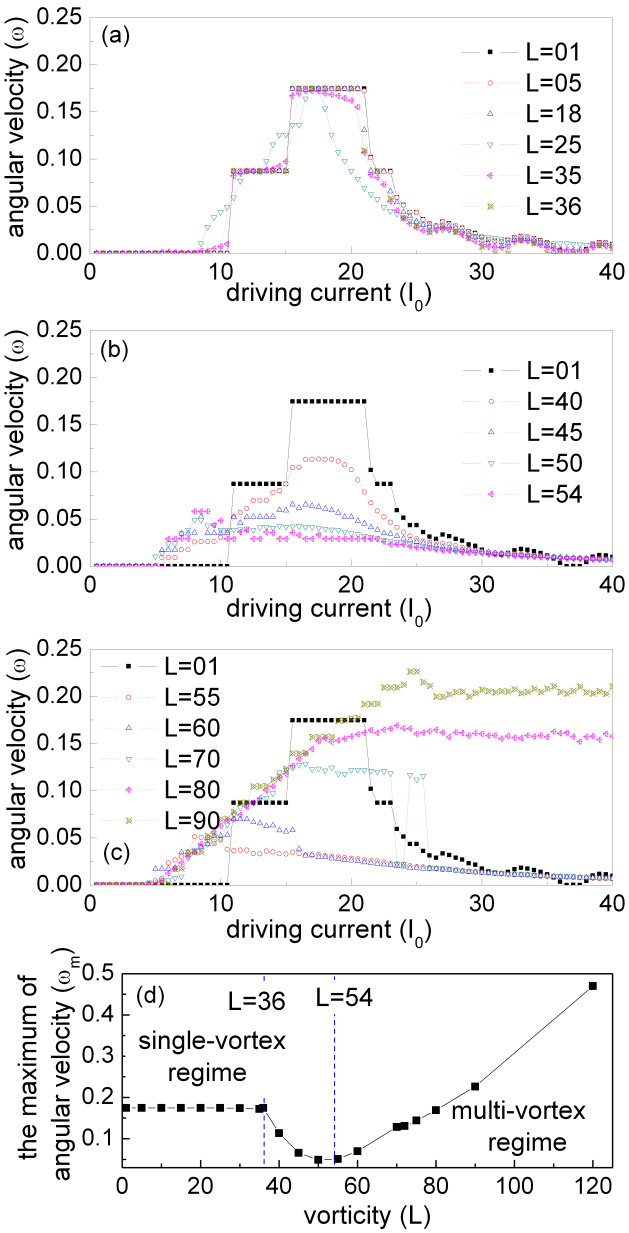

Figure 4.3: The $\omega - I_0$ curves for different density of vortices: (a) the density of vortices is low, $L = 1 - 36$ (in the single-vortex regime), the angular velocity reaches the same maximum; (b) the density increases, $L = 40 - 55$, the maximum of the angular velocity decreases; (c) for further increasing density, *i. e.*, high density of vortices, $L = 55 - 90$, the maximum starts to increase and the critical value of the driving current, when the angular velocity starts decreasing, becomes larger; (d) the maximum of the angular velocity ω_m first remains the same until the number of vortices $L > 36$. Then the maximum ω_m first decreases, but for $L > 55$ it starts to increase.

case is similar to that of the system with just one vortex [shown in Fig. 4.3 (a)], which is considered in the single-vortex regime. Thus, for $L = 1 - 36$, the maximum of the angular velocity is the same value [see Fig. 4.3 (a)]. When the density increases and therefore the interaction between the vortices becomes appreciable, the maximum of the angular velocity ω_m first decreases to 0.05 for $L = 55$ [see Fig. 4.3 (b)] and then starts to increase [see Fig. 4.3 (c)] when the system turns to the regime of high vortex density.

To understand this non-monotonic behavior of the maximum of the angular velocity ω_m [shown in Fig. 4.3(d)], we studied the trajectories of moving vortices. When the system is in the single-vortex regime, where $L \leqslant 36$, all the vortices move along a nearly circular trajectory no matter whether the applied current is small or large, which can be considered as a one-dimensional (1D) motion (shown in Fig. 4.4). For low driving currents, each vortex oscillates near its initial position inside a TC [*e. g.*, see Fig. 4.4 (a)], and when the driving force reaches some critical value, all the vortices move with a net angular velocity ω in the easy direction [*e. g.*, see Fig. 4.4 (b)]. However, in the multi-vortex regime, *i. e.*, the high density case (*e. g.*, $L = 80$), the motion of vortices is not 1D any more. The ac current drives vortices to pass through the narrow part (*i. e.*, neck) of the channel in the easy direction and when current is alternated, some of vortices are forced to move into the corner by the others and "freeze" thus blocking the motion in the hard direction [shown in Fig. 4.5]. Due to the asymmetry in the radial direction and radially decreasing current density in the Corbino setup, a vortex near the inner corner, which is closer to the center of the disk, moves faster than the one near the outer corner. Therefore, at a specific value of the current [*e. g.*, at $I_0 = 9$, as shown in Fig. 4.5(a)], the vortex near the inner corner has a larger angular velocity. When the current increases, more and more vortices move along the circular trajectory and the distribution of vortices becomes strongly inhomogeneous [shown in Fig. 4.5(b)]. With further increasing current, this 2D trajectory becomes narrow and all the vortices move along the circle, *i. e.*, the 2D motion becomes 1D [shown in Fig. 4.5(c)]. With increasing density, more and more vortices remain in the area near the corners of TCs and block other vortices moving in the hard direction. Therefore, the maximum of vortex angular velocity increases. Even in the descending-velocity region of the single-vortex regime [see *e. g.*, when $I_0 > 21$ in Fig. 4.3(c)], the angular velocity is still large.

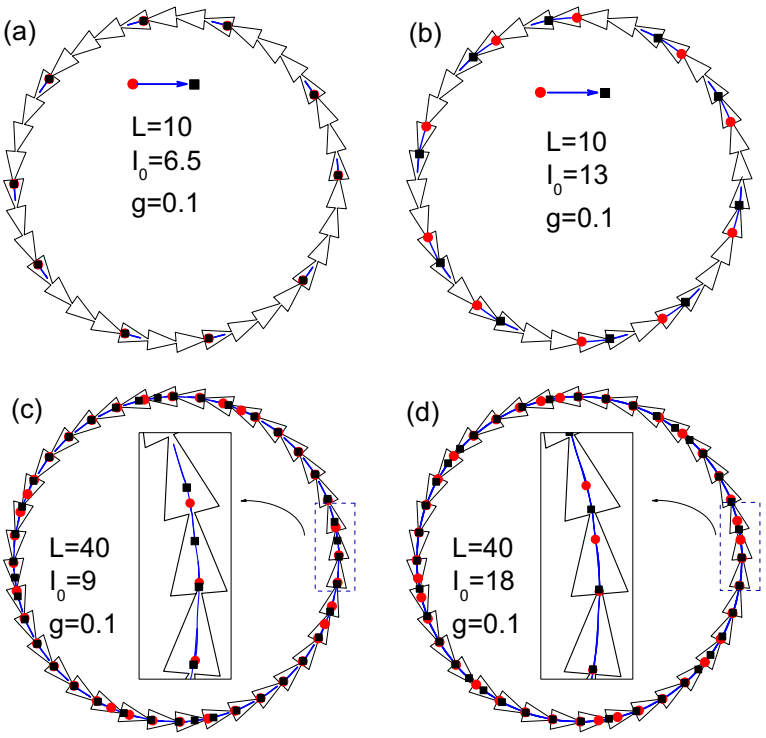

Figure 4.4: Trajectories of vortex motion, in the case of the low density of vortices ($L = 10$) (a), (b), and in the intermediate case ($L = 40$) (c), (d), for different values of driving current: $I_0 = 6.5$ (a), 13 (b), 9 (c), and 18 (d). The initial positions of the vortices are marked by gray circles and the final positions after one period of ac current are marked by black squares. The trajectories of vortices, which are plotted by solid lines, are nearly circular no matter that the current is large or small.

The maximum of the angular velocity ω_m for different vorticities L is shown in Fig. 4.3(d). In the single-vortex regime, where there is less than one vortex per TC, ω_m remains almost the same value because of the weak interaction between vortices. When L becomes larger, there are more than one vortex per TC and the repulsive vortex-vortex interaction in the same TC makes the motion in either easy or hard directions much easier. Therefore, ω_m first decreases when $L > 36$. However, for $L \geqslant 55$, the maximum ω_m starts to increase. The reason for this behavior is the transition from 1D motion to 2D motion. When vortices move along 2D trajectories (see Fig. 4.3), the repulsive interaction between vortices still "helps" a vortex to move to the next TC in the easy direction but blocks the

vortex motion in the hard direction until applying a large enough driving current.

The radial asymmetry facilitates the motion of vortices from inner/outer corners (driven by stronger/weaker force) one by one. This is different from the case of a linear ratchet channel where two vortices in the corners are driven by the same force and, as a result, arrive simultaneously at the neck region leading to jamming. In an asymmetric channel, the symmetry is broken, and jamming occurs only for rather large driving force.

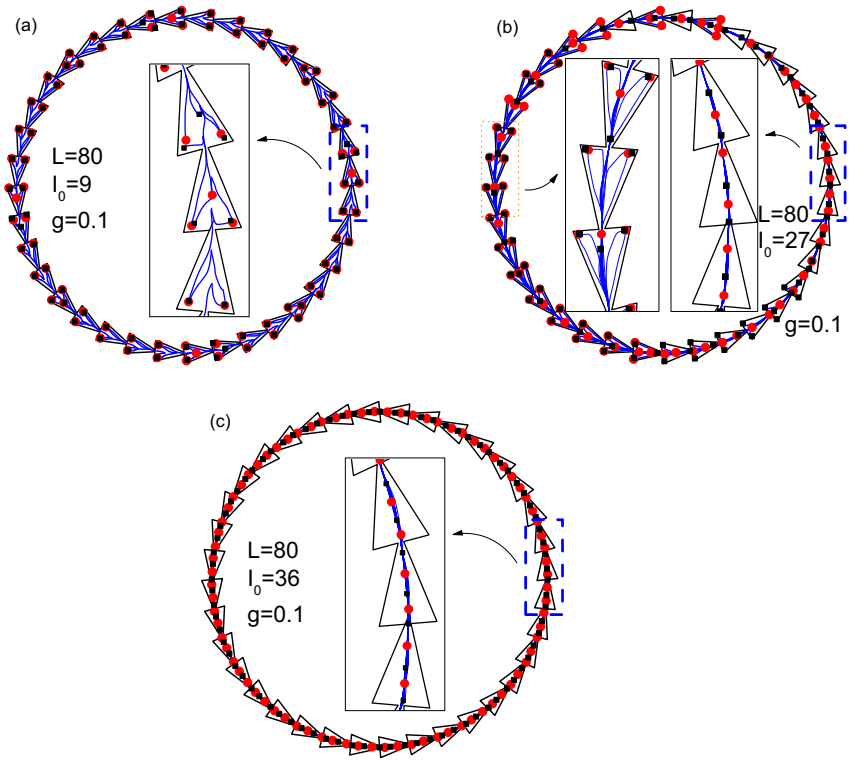

Figure 4.5: Trajectories of vortex motion during one ac period in the case of high density of vortices ($L = 80$), *i.e.*, the multi-vortex regime, for different values of the driving current, $I_0 = 9$ (a), 27 (b), and 36 (c). When the current is in a certain range $I_0 = 5 - 19$ [see Fig. 4.3 (c)], the vortices move along 2D trajectory [*e.g.*, $I_0 = 9$, shown in (a)] which is different from the circular 1D trajectories in the low density case. With increasing current, more vortices start to move along circular trajectories and thus 2D trajectories finally turns to a 1D circle [*e.g.*, see (c)]. During the transition from the 2D to 1D motion, the distribution of vortices becomes inhomogeneous [shown in (b)].

4.2.2 *Frequency dependence*

The dynamical behavior of vortices in the considered ratchet system is also strongly influenced by frequency of the ac current. In this subsection we study frequency dependence of the rectified vortex motion. For different frequencies ν, the $\omega - I_0$ curves are shown in Fig. 4.6.

When the frequency is low, the dynamical behavior is similar for different vortex densities. As the drive amplitude I_0 is increased, the angular velocity first increases, reaches a maximum, and then decreases to zero. The curves, especially for $L = 1$, in Fig. 4.6(a) are similar to the analytic result in a ratchet potential (*e. g.*, see Fig. 2 in Ref. [87]). In the case of $L = 1$, the first critical value of current I_{c1} [shown in Fig. 4.6(a)] corresponds to the maximum friction in the easy direction f_m^+ and the second one I_{c2} corresponds to the case when the driving force reaches the maximum friction in the hard direction f_m^-. When $L = 40$, the first critical value of current decreases to I'_{c1}, which means vortices are easier to move in the easy direction. If the density increases further, I'_{c1} decreases and I'_{c2} increases, for $L = 80$ [shown in Fig. 4.6(a)]. Therefore, the interaction between vortices allows vortices to move even easier in the easy direction and harder in the hard direction.

For an intermediate frequency [*e. g.*, $\nu = 1$ as shown in Fig. 4.6(c)], when the distance a vortex moves during one period is comparable to the size of a TC, the dynamical behavior of vortices will depend not only on the driving force but also on the vortex density. This is explained by the fact that the confinement force due to the boundary and the vortex-vortex interaction are also comparable. In this case we obtain different dynamical behavior in single-vortex and multi-vortex regimes which were discussed in the previous subsection. Due to the commensurability between the numbers of TCs and vortices, a step structure of the $\omega - I_0$ curve is revealed in the low density case (*e. g.*, $L = 1$ and $L = 10$), which will be discussed in more detail in Sec. IV.

As one can predict, the angular velocity becomes zero [see Fig. 4.6(e)] when the frequency is high enough because a vortex oscillates near its initial position inside a cell and thus its motion cannot be rectified. Therefore, the variation of the angular velocity is much smaller than that in the low/intermediate frequency case. Each vortex is localized in a specific TC, *i. e.*, the vortex is only influenced by a single potential well but not by the ratchet potential.

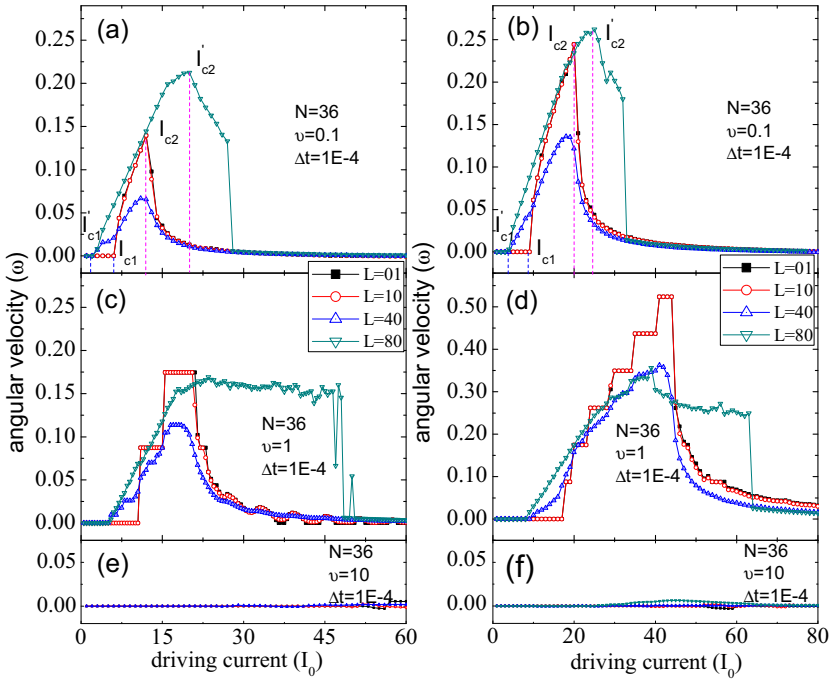

Figure 4.6: The $\omega - I_0$ curves for different frequencies: $\nu = 0.1$ (a), (b), $\nu = 1$ (c), (d), and $\nu = 10$ (e), (f). (a), (c), and (e) are in the system with a narrower neck, $g = 0.1$, and (b), (d), and (f) are in the system with a wider neck $g = 0.15$. The scale of ω in panel (d) is different from the others. For low frequency current (*e.g.*, $\nu = 0.1$) the ratchet effect is clearly seen [as shown in (a) and (b)]. In this case, the angular velocity first increases continuously to the maximum and then decreases to zero. For intermediate frequency $\nu = 1$, besides the ratchet effect, the effect of commensurability, *i.e.*, discontinuity in the angular velocity $\omega(I_0)$ (see Sec. IV), has a clear influence on the $\omega - I_0$ curve [*e.g.*, see (c) and (d) for $L = 1$ or $L = 10$]. For high frequency current (*e.g.*, $\nu = 10$), vortices are confined in their initial TCs and only oscillate in a single potential well. Therefore, the effect of the periodic ratchet potential disappears [shown in (e) and (f)].

For comparison, we also calculate $\omega - I_0$ curves for the case when a TC has a wider connection part ($g = 0.15$) [shown in Fig. 4.6(b), (d), (f)]. The function $\omega(I_0)$ in general shows a similar behavior as for $g = 0.1$. However, for the intermediate frequency ($\nu = 1$) of the applied current, we obtain more steps in $\omega - I_0$ curve in the case of $L = 1$ [shown in Fig. 4.6(d)] than that for $g = 0.1$ [shown in Fig. 4.6(c)]. This relates to the commensurability effect that will also be discussed in Sec. IV.

4.3 COMMENSURABILITY EFFECT

4.3.1 *Commensurability of vortex density*

As we defined above, the system contains L vortices and N triangles in a circular chain. If there is a common integer (except one) in terms of which two numbers L and N can both be measured, then they are commensurate. Otherwise, they are incommensurate. Fig. 4.7 shows the average angular velocity ω as a function of I_0 for different commensurate ratios. The ascending part of the $\omega(I_0)$ curves (*i. e.*, where ω versus I_0 increases) is stepwise. Besides the large steps of angular velocity in the $\omega - I_0$ curve for $L = 1$, which we refer to as "integer steps", we also found smaller steps for some specific vorticities L (shown in Fig. 4.7). If $L/N = k/m$ and $k \neq 1$, where k and m are incommensurate integers, the small steps can be found in the $\omega - I_0$ curves [in Fig. 4.7(b)-(d)]. When $k = 1$, we observe only integer steps of the angular velocity $\omega(I_0)$ [in Fig. 4.7(a)]. The difference in the angular velocity between two adjacent steps is always ω_0. If $k \neq 1$, then we can find a fractional step whose magnitude is ω_0/k. For example, for $k = 2$ [shown in Fig. 4.7(b)], the smallest step is $\omega_0/2$ in the system with 72 vortices (*i. e.*, $L = 72$), which is a half of that for $k = 1$ (*e. g.*, when $L = 36$). In the case of $k = 1$, a unit cell contains only one vortex. [The "unit cell" (UC) is a minimum repeatable set of TC(s) containing an integer number of vortices. For example, for $L = 1$ the UC is the entire channel with one vortex, and for $L = 36$ the UC is one TC with one vortex.] If one vortex can overcome the potential barrier and move in the easy direction, all the vortices can do so at the same time, *i. e.*, collectively. This results in integer steps of the average angular velocity ω_0 in the $\omega - I_0$ curve. However, fractional steps appear when there are more than one vortex in each UC. For instance, a UC contains one TC with two vortices when $L = 72$, and if $L = 24$, the UC is con-

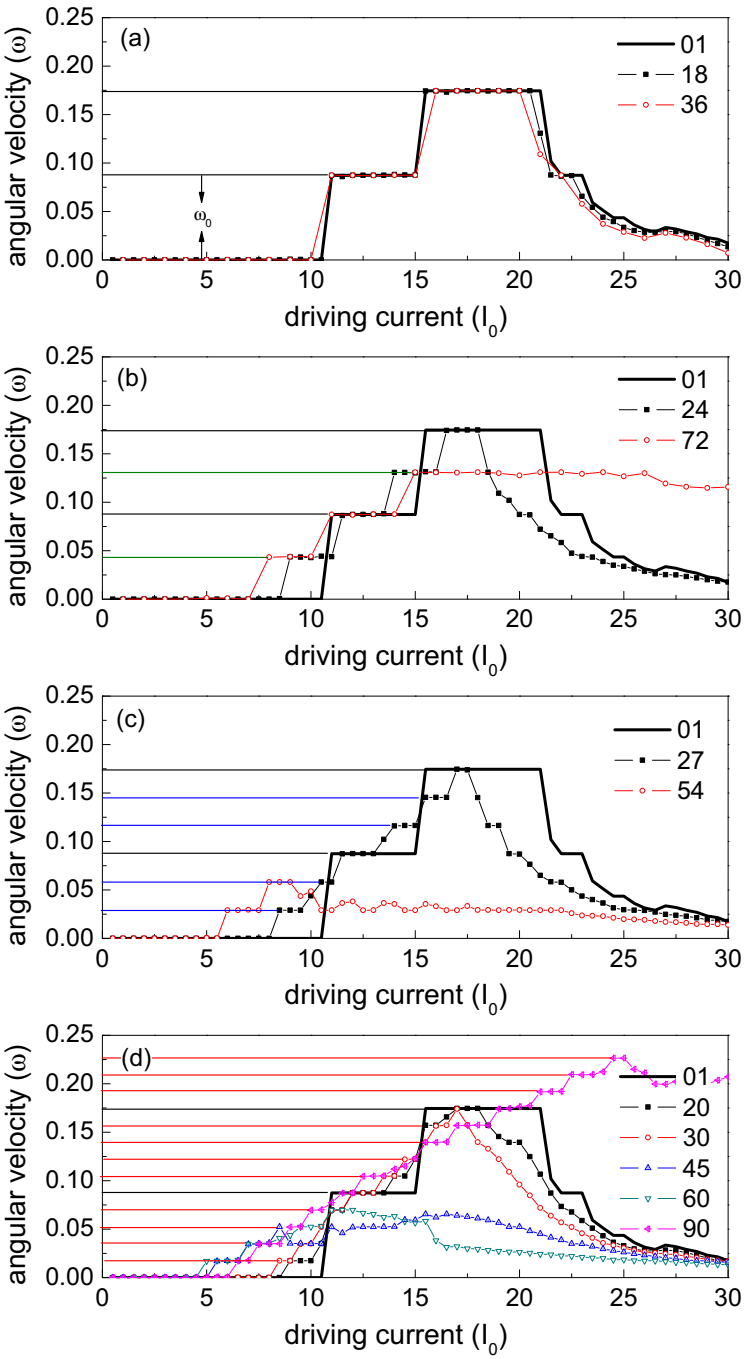

Figure 4.7: The $\omega - I_0$ curve for a channel with $g = 0.1$ and different k: $k = 1$ (a), 2 (b), 3 (c), and 5 (d). L is the vorticity, *i.e.*, the number of vortices. N is the number of cells in the circular chain. If $L/N = 1/m$, *e.g.*, $L = 1, 36$, the $\omega - I_0$ curve shows several steps and the height of each integer step is ω_0. When $L/N = k/m$ (k=2, 3, 5), the height of each fractional step is ω_0/k [*e.g.*, as shown in (b) (c) and (d)].

structed by three TCs with two vortices. In general case, the unit cell contains m TCs with k vortices inside. If $k > 1$, there are more than one vortex in the UC, and those vortices are not equivalent, *i. e.*, they are not located at the equivalent position in the TC and/or they experience different interactions with the boundary. Therefore, they move with different angular velocities in each period. Let us take $k = 2$, for example (see Fig. 4.8). As shown in Fig. 4.8(a), the vortices located in a TC that is followed by an empty TC in the easy direction (type-A) can overcome the potential barriers in a period of alternating current and move to its neighbor TC, while the others (type-B) are still localized in its original TC. When $I_0 = 10$ [shown in Fig. 4.8(b)], type-A vortices move from C2 to C3 but type-B vortices only oscillate in C1. In the view of the whole circular channel, only a half of vortices (*i. e.*, type-A vortices) move to another TC while the other half of vortices (*i. e.*, type-B vortices) do not move. After that, the type-B vortices are located at similar position as type-A vortices in the previous cycle, *i. e.*, the previous type-B vortices now become type-A vortices and they will move to next TC in the anticlockwise direction during the next period. Therefore, when we calculate the average angular velocity for all the vortices, the value is a half of the angular velocity of type-A vortices, *i. e.*, $\omega_0/2$. If the current increases, every vortex can overcome the barriers and move to the neighbor TC [*e. g.*, as shown in Fig. 4.8, type-A vortices move from C2 to C3 and type-B vortices move from C1 to C2 when $I_0 = 13$]. Then average angular velocity becomes ω_0 which is the same as that for $k = 1$ when all vortices move to the neighbor TC.

4.3.2 *Commensurability effect of frequency*

Further we analyze the angular velocity evolution while varying the ac drive frequency (shown in Fig. 4.9). For varying frequency ν, the $\omega - \nu$ curves are characterized by peaks and/or oscillations. Let us clarify this behavior. As discussed in Sec. III, if $f_m^- > f^d > f_m^+$, vortices can move in the easy direction and be frozen/blocked in the hard direction when the current alternates. Let us introduce a time scale, T_0, to characterize the motion of a vortex over the entire TC. One TC occupies an angle $\theta_0 = 2\pi/N$. If we assume that a vortex moves over the entire TC to the equivalent position in the next TC, then T_0 should satisfy the following condition:

$$\int_0^{T_0} \omega dt = \int_0^{T_0} [\mathbf{f}^d(I_0) + \mathbf{f}^b + \mathbf{f}^{vv}] \cdot \hat{\theta} dt/\eta r = \theta_0, \tag{4.4}$$

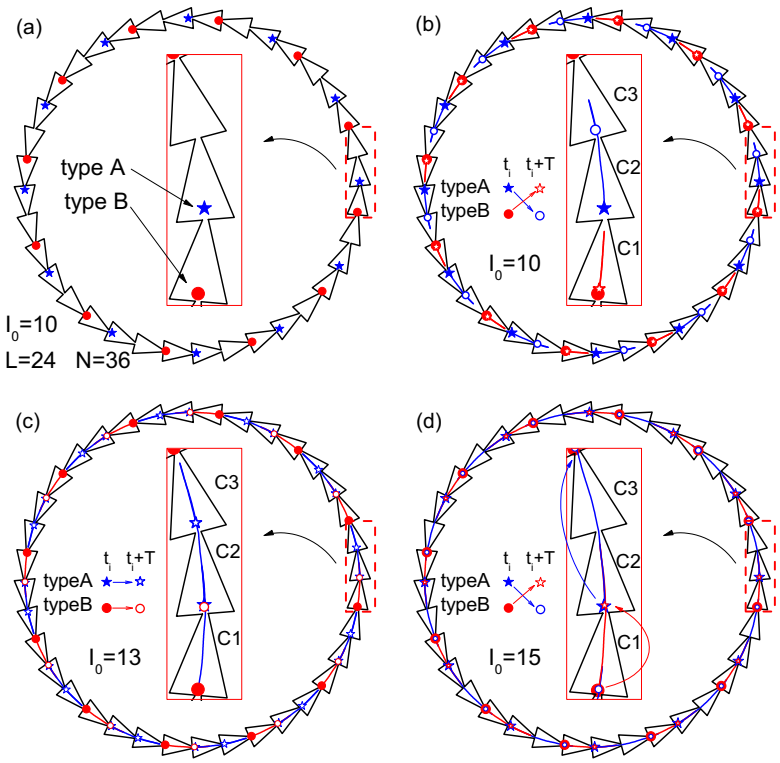

Figure 4.8: (a) The configuration of 24 vortices after 1000 periods of oscillations, $t = t_i$. The moving trajectories of vortices in one period of ac current, *i.e.*, from $t = t_i$ to $t = t_i + T$, is shown for $I_0 = 10$ (b), 13 (c), and 15 (d). The insets of (a)-(d) show the vortex distribution in a unit cell. For $L = 24$, a type-A vortex is the vortex in a triangular cell (TC) [*e.g.*, TC C2 in the inset of (a)] that has a neighbor empty TC in the easy direction [*e.g.*, TC C3 in the inset of (a)], *i.e.*, a TC without vortex, while a type-B vortex is in a TC [*e.g.*, TC C1 in the inset of (a)] that neighbors a TC with type-A vortex inside. When the current drives vortices in the easy direction (*e.g.*, $I_0 = 10$), two types of vortices move in different ways. Type-A vortices move from C2 to C3 but type-B vortices do not move to C2 due to a larger repulsive interaction in the easy direction (b). When $I_0 = 13$ (c), $\omega = \omega_0$ is the same as the integer step in $\omega - I_0$ curve [see Fig. 4.7(b)]. The type-A (type-B) vortex moves over one TC and remains type-A (type-B) in the end of the period. If the current increases further, *e.g.*, $I_0 = 15$, type-A and type-B vortices move with different net angular velocities and after every period they switch their type [shown in (d)].

where $\hat{\theta}$ is the unit vector in the azimuthal direction. In the single vortex case ($L = 1$), we set $f^{vv} = 0$, and θ_0 is a constant. Considering the circular trajectory of the moving vortex, the integral of f^b is also a constant. Therefore, T_0 only depends on the current I_0 and we use the notation $T_0(I_0)$ instead of T_0 in order to show the dependence on the driving current.

If $f_m^- > f^d(I_0) > f_m^+$ and the ac period $t = 2T_0(I_0) = t_0(I_0)$, then the rectified signal will be maximum since all the vortices coherently move over the entire TC in the easy direction during the first half period and do not move backwards in the next half period. Then we can obtain the principal period $t_0(I_0) = 2T_0(I_0)$ for each value of the current and roughly estimate forces f_m^- and f_m^+ from the $\omega - \nu$ or $\omega - t$ curves [as shown in Fig. 4.9]. The maximum angular velocity ω_m for different current and vorticities L is shown in the insets of Fig. 4.9. For example, in the case of $L = 1$ [see Fig. 4.9(a)], the angular velocity is always zero when $I_0 \leqslant 8$ and becomes nonzero for $I_0 = 10$, *i. e.*, the vortex starts to move in the easy direction. Therefore, $f^d(I_0 = 8) < f_m^+ < f^d(I_0 = 10)$. However, for $I_0 \geqslant 22$, the maximum angular velocity ω_m decreases as compared to the case for $I_0 = 20$, which means $f^d(I_0 = 20) < f_m^- < f^d(I_0 = 22)$. For $f^d(I_0) > f_m^-$ when driving current increases, vortices move backwards (*i. e.*, the motion in the hard direction) therefore resulting in the decreasing net angular velocity. For example, when $I_0 = 22$ [shown in Fig. 4.9(a)], the maximum ω_m becomes smaller and the jumps in the $\omega - t$ curves become smoother, which means the effect of boundary becomes weaker under a strong driving force. Therefore, the angular velocity should be zero when the driving force goes to infinity. It explains why the angular velocity decreases and goes to zero when the driving current increases above some critical value.

For the single-vortex case, the frequency dependence of the first local maximum ω'_m in the $\omega - \nu$ curves versus the corresponding drive frequencies, $\nu_0 = 1/t_0$, is plotted in Fig. 4.10 which shows a linear behavior. When the density is increased up to one vortex per cell ($L/N \leqslant 1$), the $\omega - t$ curve is similar to the one for $L = 1$ for both incommensurate [*e. g.*, see Fig. 4.9(b)] and commensurate cases [see Fig. 4.9(c)] because the interaction between vortices is weak. For a higher density, the (in-)commensurability effect becomes pronounced. The sharp jumps of the angular velocity are obtained only in the commensurate case [*e. g.*, $L = 72$ shown in Fig. 4.9(e)] but not in the incommensurate case [*e. g.*, $L = 80$ shown in Fig. 4.9(f)]. Comparing the high density cases with the low den-

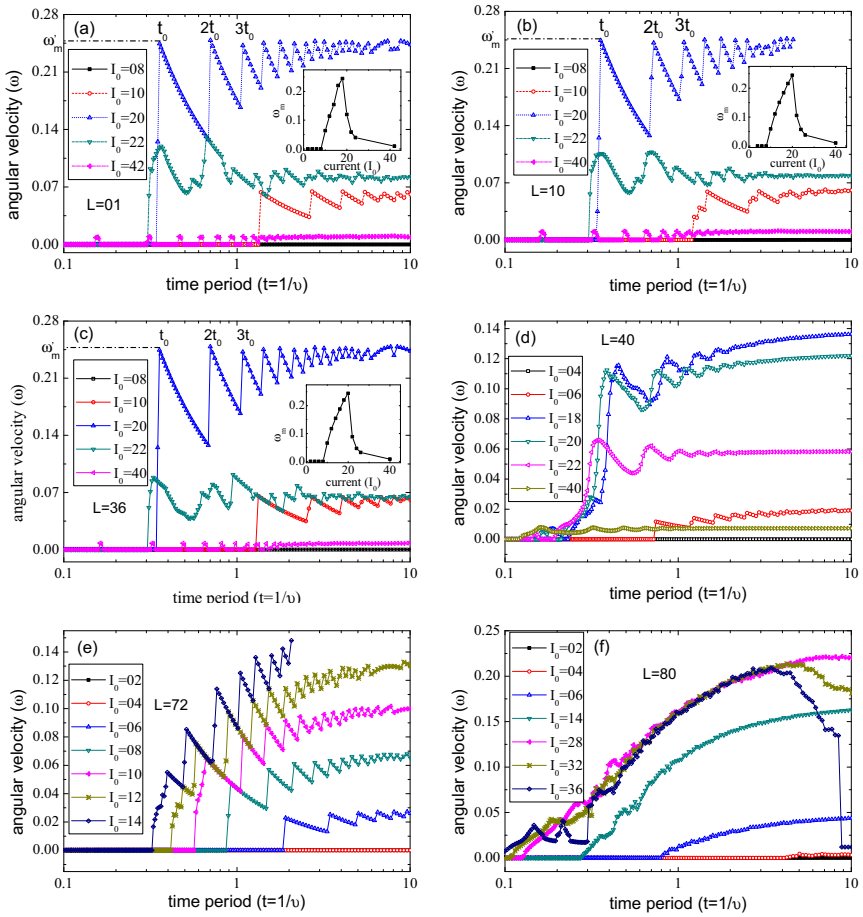

Figure 4.9: The $\omega - t$ curves in a channel with $g = 0.1$ for different density of vortices: $L/N \ll 1$ (a), $L/N < 1$ (b), $L/N = 1$ (c) (commensurate), $2 > L/N > 1$ (d), $L/N = 2$ (e) (commensurate), and $L/N > 2$ (f). When the density $L/N \leqslant 1$, *i.e.*, in the single-vortex regime, the angular velocity $\omega(t)$ first reaches the maximum and then oscillates [see (a), (b) and (c)]. With increasing current, the maximum velocity increases until the driving force reaches the value larger than f_m^-. For high density, the angular velocity $\omega(t)$ does not reach the maximum because the vortex motion in the easy direction is compensated by that in the hard direction. $\omega(t)$ increases when the frequency decreases. In commensurate cases [(c) and (e)] $\omega(t)$ oscillates with sharp jumps which are not observed in incommensurate cases for high vortex density (f).

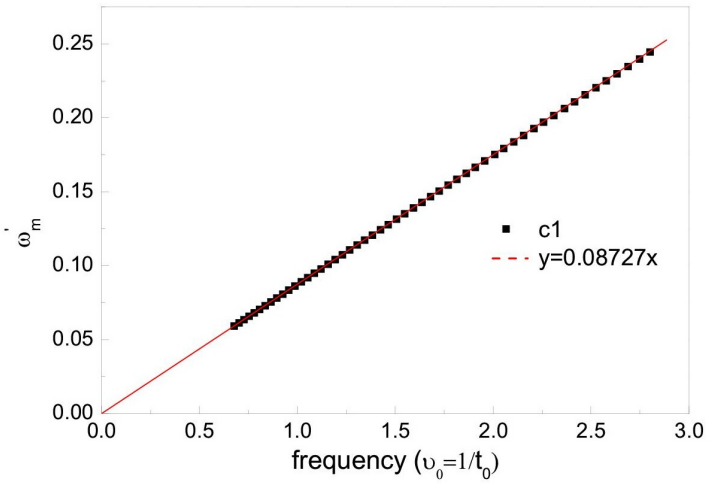

Figure 4.10: The frequency dependence of the first local maximum ω'_m of the $\omega - t$ curves for vortices in the single-vortex regime when the driving force is smaller than f_m^-. The magnitude of the first peak shows a linear dependence on the principal frequency ν_0.

sity cases, we can conclude that sharp jumps in $\omega - t$ curve, which are both found in single-vortex and multi-vortex regimes, are due to the effect of periodically repeated boundaries of the ratchet potential and the increasing local maximum of the angular velocity when t increases in the multi-vortex regime. This is different from the single-vortex regime, because of the strong interaction between vortices induced by the high vortex density. If the principal period (*i. e.*, the time period for the first jump) is denoted by t_0, the others will be harmonics of t_0, kt_0 $(k = 2, 3, ...)$.

4.4 Experimental detection of vortex ratchet effect in a Corbino geometry

Our coauthors from Syracuse University in USA [125] have performed preliminary measurements on a device containing a single weak-pinning circular channel for guiding vortex motion in a Corbino geometry. This is based on a technique for using weak-pinning channels with tailored edges to produce asymmetric vortex confining potentials. Such an arrangement resulted in substantial asymmetric vortex response for linear channels on a strip geometry [63]. The Corbino sample consists of a Si substrate with a 200-nm thick film of weak-pinning a-NbGe and a 50-nm thick

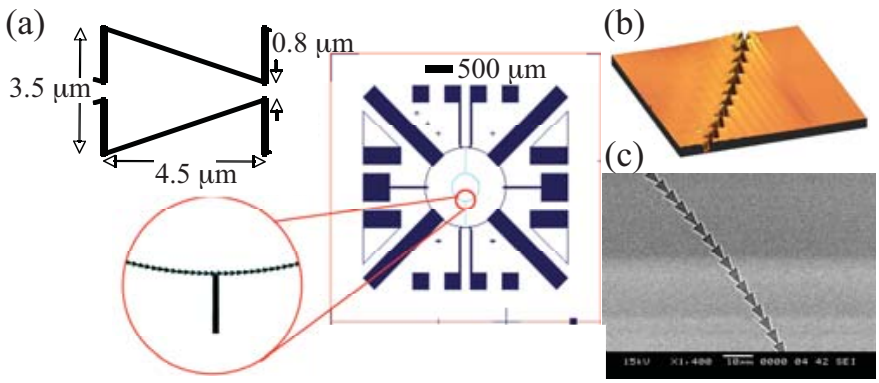

Figure 4.11: (a) Detail of single ratchet cell of channel and schematic of Corbino ratchet chip layout; extra pads and leads beyond disk were not used for the measurements presented here. (b) Atomic force microscope image of portion of Corbino ratchet channel. (c) Scanning electron micrograph of portion of Corbino ratchet channel.

film of strong-pinning NbN on top. The fabrication followed the scheme of previous weak-pinning channel devices [63, 130], with the 1.5-mm diameter Corbino disk pattern etched through the entire superconducting bilayer. The 500-μm diameter circular chain of triangular cells was etched through the NbN layer (Fig. 4.11), thus defining the weak-pinning a-NbGe channel region for vortex flow.

Wirebonds were attached between the center and perimeter of the Corbino disk for injecting a bias current with a radial flow. Because of the rather small flux-flow voltages for vortex motion in a single channel, it was necessary to use a custom picovoltmeter based on a dc SQUID operated in a flux-locked loop [130]. Measurements of the noise power at different temperatures were used to calibrate the value for the series resistance at the SQUID input, thus allowing for a measurement of the system gain, as described in Ref. [130]. During the measurements, the sample and SQUID were immersed in a pumped liquid helium bath. Shielding of external magnetic fields was achieved with a μ-metal shield surrounding the dewar and a superconducting Pb shield around the sample and SQUID on the bottom of the cryogenic insert. Vortices were introduced into the channel by temporarily raising the sample above the helium bath, heating to ~6 K – between T_c^{NbGe} = 2.88 K and $T_c^{NbN} \approx$ 10 K – while applying a small magnetic field with a Helmholtz coil on the insert, then cooling back down below T_c^{NbGe}.

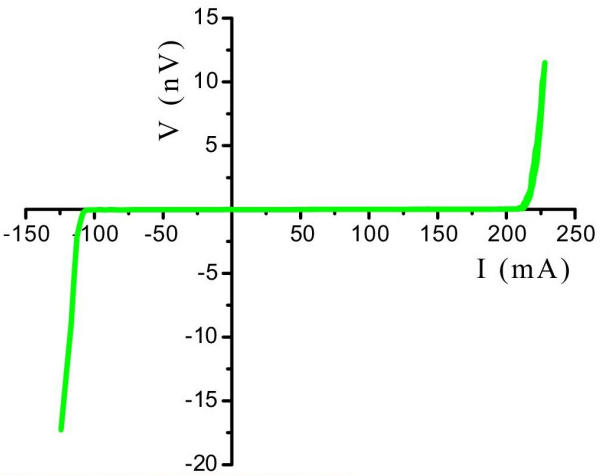

Figure 4.12: Current-voltage characteristic of Corbino ratchet channel cooled to 1.60 K in an external magnetic field of 0.26 Oe as described in text.

Upon reaching the desired measurement temperature, the bias current was varied incrementally and the flux-flow voltage sensed by the SQUID was recorded for each current value. Such current-voltage characteristics (IVC) exhibited substantial asymmetries between the critical current for vortices to begin to move through the channel for the two directions. This asymmetry persisted down to the lowest measurement temperature, 1.60 K, well below the onset of superconductivity in the channel at T_c^{NbGe} (Fig. 4.12). The larger critical current corresponded to the sense of vortex motion in the hard direction through the ratchet cells. Due to experimental wiring limitations on these preliminary measurements of a Corbino ratchet channel, it was not possible to sweep the bias current with an oscillatory drive to study the average flux-flow voltage over a cycle. Nonetheless, the large asymmetry between the two senses of critical current demonstrates the potential for a weak-pinning ratchet channel in a Corbino geometry to rectify vortex motion.

5

SOLUTIONS OF RICHARDSON EQUATIONS AND ELECTRON-HOLE SYMMETRY OF PAIRING HAMILTONIAN

5.1 INTRODUCTION

It was shown by Richardson in 1960's that the "reduced" Hamiltonian of the Bardeen-Cooper-Schrieffer (BCS) theory of superconductivity is exactly solvable [17]. Richardson approach is based on the canonical ensemble, *i.e.*, the number of particles is fixed, while BCS theory corresponds to the grand canonical description, which becomes correct in the large-particle limit. In addition, BCS theory corresponds to the mean-field approximation, which turns out to be exact [26, 27] in the large-sample limit. However, grand canonical BCS theory is not applicable for small-sized systems accommodating small clusters containing only a few pairs. Serious improvements, nevertheless, are possible if one incorporates canonical approach into the BCS model (particle number projected BCS), but still a rather heavy numerics is needed to proceed with computations [14, 15].

In contrast to the BCS theory, Richardson treatment yields an exact solution to the many-body problem. The energy of the system of N correlated pairs is expressed through the sum of N energy-like quantities, which satisfy the system of N coupled nonlinear equations, called Richardson equations. It is remarkable that they can be also derived through the algebraic Bethe-ansatz approach [131]. However, solving Richardson equations is a formidable task. Up to now, they have been solved analytically in few cases only. In particular, no analytical solution exists for the important regime corresponding to the crossover between the superconducting state and the pairing fluctuation regime, which is relevant for small-sized systems. For this case, Richardson equations are tackled numerically, when studying nanosized superconducting grains [13, 132, 133] and

nuclei [134] (for studies of correlation functions, see Ref. [135, 136, 137]).

5.2 ELECTRON-HOLE SYMMETRY

We consider a system of fermions of two sorts, for instance, with up and down spins. The number of particles is fixed, *i.e.*, we stay within the canonical-ensemble approach [138]. Particles attract each other through the BCS "reduced" potential, coupling only fermions of different sorts and with zero total momenta as

$$\mathcal{V} = -V \sum_{\mathbf{k},\mathbf{k}'} a^{\dagger}_{\mathbf{k}'\uparrow} a^{\dagger}_{-\mathbf{k}'\downarrow} a_{-\mathbf{k}\downarrow} a_{\mathbf{k}\uparrow}. \tag{5.1}$$

The total Hamiltonian is $H = H_0 + \mathcal{V}$, where

$$H_0 = \sum_{\mathbf{k}} \varepsilon_{\mathbf{k}} \left(a^{\dagger}_{\mathbf{k}\uparrow} a_{\mathbf{k}\uparrow} + a^{\dagger}_{\mathbf{k}\downarrow} a_{\mathbf{k}\downarrow} \right). \tag{5.2}$$

The summation in the right-hand side (RHS) of Eq. 5.1 runs only over the states with kinetic energies $\varepsilon_{\mathbf{k}}$ and $\varepsilon_{\mathbf{k}'}$ located in the energy range between ε_{F_0} and $\varepsilon_{F_0} + \Omega$ (Debye window). These energies are distributed equidistantly (equally-spaced model), so that the difference between two nearest values of $\varepsilon_{\mathbf{k}}$ is $1/\rho$. The density of states ρ increases with the system volume, while the interaction constant V decreases, so that the dimensionless interaction constant $\nu = \rho V$ is finite and, in the large-sample limit, it can be treated as a material characteristics. In BCS theory, the energy interval between ε_{F_0} and $\varepsilon_{F_0} + \Omega$ is assumed to be always half-filled, while $\Omega/2$ is the Debye frequency. Thus, the total number of available states with up or down spins in the Debye window is $N_\Omega \equiv \rho\Omega$, while $N = N_\Omega/2$; $\varepsilon_{\mathbf{k}}$ runs from ε_{F_0} to $\varepsilon_{F_0} + (N_\Omega - 1)/\rho$ taking N_Ω values in total.

While it is believed that the half-filling configuration only is physically meaningful, one can consider other fillings and at least treat the problem from the purely mathematical perspective. Introduction of this extra degree of freedom is an important ingredient of our analysis. By considering the energy of the system formally as a function of N (with all other input parameters fixed), we are going to obtain a valuable information on the half-filling situation. Numerical results will be presented for $N = N_\Omega/2$ only. For the sake of simplicity, we will focus on even values of N_Ω.

The Hamiltonian, defined in Eqs. 5.1 and 5.2, is exactly solvable [27]. The energy of N pairs is given by the sum of N rapidities R_j ($j = 1,..., N$)

$$E_N = \sum_{j=1}^{N} R_j. \tag{5.3}$$

The Richardson equation for each rapidity R_j reads as

$$1 = \sum_{\mathbf{k}} \frac{V}{2\varepsilon_{\mathbf{k}} - R_j} + \sum_{l,l\neq j} \frac{2V}{R_j - R_l}, \tag{5.4}$$

where the summation in the first term is performed for $\varepsilon_{\mathbf{k}}$ located in the Debye window.

Now we discuss the internal electron-hole symmetry contained in the Hamiltonian, from which we try to deduce an information on the solutions of Richardson equations without really solving them.

Let us introduce creation operators for holes as $b^{\dagger}_{\mathbf{k}\uparrow} = a_{\mathbf{k}\uparrow}$ and $b^{\dagger}_{\mathbf{k}\downarrow} = a_{\mathbf{k}\downarrow}$. By using commutation relations for fermionic operators, it is easy to rewrite the Hamiltonian in terms of holes as

$$H = -VN_\Omega + 2\sum_{\mathbf{k}} \varepsilon_{\mathbf{k}} - \sum_{\mathbf{k}} (\varepsilon_{\mathbf{k}} - V)\left(b^{\dagger}_{\mathbf{k}\uparrow} b_{\mathbf{k}\uparrow} + b^{\dagger}_{\mathbf{k}\downarrow} b_{\mathbf{k}\downarrow}\right) - V\sum_{\mathbf{k},\mathbf{k}'} b^{\dagger}_{\mathbf{k}'\uparrow} b^{\dagger}_{-\mathbf{k}'\downarrow} b_{-\mathbf{k}\downarrow} b_{\mathbf{k}\uparrow}. \tag{5.5}$$

The first two terms of the RHS of Eq. 5.5 are numbers. They give the potential energy and the kinetic energy of the Debye window completely filled by electron pairs. The fourth term is fully identical to the interaction potential in terms of electrons, given by Eq. 5.1. To analyze the third term, we introduce $\xi'_{\mathbf{k}}$, defined as $\xi'_{\mathbf{k}} = \varepsilon_{F_0} + (N_\Omega - 1)/\rho - \varepsilon_{\mathbf{k}}$, which takes values 0, $1/\rho$, $2/\rho$, ..., $(N_\Omega - 1)/\rho$, so that $\xi'_{\mathbf{k}}$ just runs over all states starting from the top of the Debye window towards its bottom, *i. e.*, in the inverse order. Then, $-(\varepsilon_{\mathbf{k}} - V)$ can be represented as $\xi'_{\mathbf{k}} + (V - \varepsilon_{F_0} - (N_\Omega - 1)/\rho)$. A similar term in the Hamiltonian for electrons, given by Eq. 5.2, contains factor $\xi_{\mathbf{k}} + \varepsilon_{F_0}$, where $\xi_{\mathbf{k}}$ takes values 0, $1/\rho$, $2/\rho$, ..., $(N_\Omega - 1)/\rho$, so that it just runs over all states starting from the bottom to the top of the same energy interval.

Thus, there exists a symmetry between electrons and holes in the Hamiltonian. Namely, the ground state of N electron pairs is equivalent to the ground state of $N_\Omega - N$ hole pairs, while the en-

ergy of the latter state is expressed through the energy of $N_\Omega - N$ electron pairs, with ε_{F_0} changed into $(V - \varepsilon_{F_0} - (N_\Omega - 1)/\rho)$. We therefore treat the ground state energy $E_N(\varepsilon_{F_0})$ as a function of ε_{F_0}, which is an arbitrary nonzero number, and a discrete variable N, which runs over the set $1, 2, ..., N_\Omega$. Since the kinetic energy of the whole Debye window filled is given by the sum of terms of the arithmetic progression, $2N_\Omega\varepsilon_{F_0} + N_\Omega(N_\Omega - 1)/\rho$, we arrive to the identity

$$E_N(\varepsilon_{F_0}) = E_{N_\Omega - N}\left(V - \varepsilon_{F_0} - \frac{N_\Omega - 1}{\rho}\right) - VN_\Omega + 2N_\Omega\varepsilon_{F_0} + \frac{N_\Omega(N_\Omega - 1)}{\rho}. \quad (5.6)$$

Next, we split $E_N(\varepsilon_{F_0})$ into the additive contribution $2N\varepsilon_{F_0}$ and E'_N, the latter being independent on ε_{F_0}

$$E_N(\varepsilon_{F_0}) = 2N\varepsilon_{F_0} + E'_N. \quad (5.7)$$

By substituting Eq. 5.7 to Eq. 5.6, we arrive to the functional equation

$$E'_N = E'_{N_\Omega - N} + (N_\Omega - 2N)\left(V - \frac{N_\Omega - 1}{\rho}\right), \quad (5.8)$$

which is still exact. This equation will enable us to relate the condensation energy of N pairs to the condensation energy of $N_\Omega - N$ pairs. Note that it is automatically fulfilled for the half-filling, $N = N_\Omega/2$.

Since E'_N is a function of the discrete variable N, which runs over N_Ω values, it can always be represented as a polynomial of N of power N_Ω. Alternatively, instead of expanding in elementary monomials N^n, one may use Pochhammer symbols defined as

$$(N)_n = N(N-1)...(N-n+1), \quad (5.9)$$

while $(N)_0 \equiv 1$; so that $(N)_n$ may be treated as a polynomial of N of power n. Then,

$$E'_N = \sum_{n=1}^{N_\Omega} \alpha_n (N)_n, \quad (5.10)$$

where α_n is a set of unknown numbers.

Actually, E'_N can be also split into a condensation energy $E_N^{(cond)}$ and the contribution coming from the kinetic energy. The latter is given universally by $N(N-1)/\rho$, which is obviously described by the second term of the RHS of Eq. 5.10.

Up to now, all the results were exact. At this step, we make a rather strong conjecture that a dominant contribution to E'_N is due to the first two terms in the sum of the RHS of Eq. 5.10 that is

$$E'_N \simeq \alpha_1 N + \alpha_2 N(N-1). \tag{5.11}$$

This assumption is not controllable, but it is fully reasonable, since such a form of E'_N does emerge in three important limits, which are solvable analytically. Let's discuss the condensation energy in these three limits, since the contribution from the kinetic energy is always in agreement with Eq. 5.11, as discussed above. The first limit is a regime of the very weak coupling realized for finite N_Ω ($v \ll \ln(N_\Omega)$), for which all the rapidities are located in real axis and approach the energy levels of noninteracting electrons. In this case, $E_N^{(cond)} = -VN$, so that Eq. 5.11 is satisfied. Another limit is the strong-coupling regime ($v \gg 1$), when all the rapidities are located far away from the line of one-electron levels on the complex plane. In this case, $E_N^{(cond)}$ contains terms proportional to N and $N(N-1)$ [17]. At last, there is a limit of infinite N at finite nonzero v; here also $E_N^{(cond)}$ has a similar form [27, 26, 116, 139].

These three limits are quite different from each other, but the dependence of E'_N on N has a similar structure. It is actually the reason why we conjecture that this structure must stay robust in the intermediate region, which is characterized by finite N_Ω and arbitrary v.

Now we consider α_1 and α_2 as unknown numbers and substitute Eq. 5.11 into Eq. 5.8. We then equate coefficients of $(N)_0$, $(N)_1$ and $(N)_2$ in both sides of this equation and obtain a system of three linear equations for α_1 and α_2. These three equations turn out to be dependent, so they yield only a single condition as

$$\alpha_2 = -\frac{\alpha_1}{N_\Omega - 1} + \left(\frac{N_\Omega - 1}{\rho} - V\right)\frac{1}{N_\Omega - 1}. \tag{5.12}$$

We are now left with the only one unknown number, α_1. It can be easily determined by considering a one-pair problem (as a "bound-

ary condition"). In this case, $E_1' = \alpha_1$, while α_1 is given by the solution of the single Richardson equation

$$V = \sum_{n=0}^{N_\Omega - 1} \frac{1}{2n/\rho - \alpha_1}, \tag{5.13}$$

under the condition $\alpha_1 < 0$, which ensures that we select the lowest-energy solution; then, $-\alpha_1$ is a binding energy of a single pair. In general case, α_1 has to be determined numerically, while exact analytical results can be obtained in certain limits, as discussed below.

The expression of E_N' is obtained by substituting Eq. 5.12 to Eq. 5.11 as

$$E_N' = \frac{N(N-1)}{\rho} + N\alpha_1 \left(1 - \frac{N-1}{N_\Omega - 1}\right) - VN\frac{N-1}{N_\Omega - 1}, \tag{5.14}$$

where the first term comes the bare kinetic energy, while two others give the condensation energy. The condensation energy per pair then reads

$$E_N^{(cond)}/N = \alpha_1 \left(1 - \frac{N-1}{N_\Omega - 1}\right) - V\frac{N-1}{N_\Omega - 1}. \tag{5.15}$$

5.3 NUMERICAL APPROACH

In order to compare the analytical result with the exact result, we have to solve the Richardson equations, which give the exact solutions. Except in extreme cases of zero or infinite coupling, no analytical solution to the Richardson equations is found [140]. Therefore, in order to study such a system, we need to use numerical techniques. The Richardson equations can be solved numerically through an appropriate change of variables [141]. By transforming the Richardson equations into the cluster equations [141], it can be applied as well to more general exactly solvable Hamiltonians associated with a coupled set of nonlinear equations of the Richardson type. Although many efforts have been made to construct efficient algorithms for solving Richardson's equation [141, 142, 143, 21, 144], it still remains a difficult task to achieve stable and fast computation of the various solutions. The systems that we are considering consist of $N = N_\Omega/2$ pairs of particles which occur N_Ω equispaced single-particle levels. Therefore, it is not necessary to solve the cluster equations. As other cases within non-linear systems, the con-

vergence of any algorithm towards a given solution highly depends on the capacity one has to generate an appropriate initial approximation of it. In general case, the Richardson equations can be numerically solved by Newton-Raphson method with a good initial guess. An exact solution $R_n = \epsilon_n = 2\varepsilon_{F_0} + 2n/\rho$ $(n = 0, 1, .., N-1)$ is known when $\nu = 0$. Since we do not know exact solutions in the intermediate regime (between the zero coupling regime and infinite coupling regime) analytically, it is natural to start from the known solution when $\nu = 0$ and increasing the coupling ν in small steps. Therefore, we can find solutions at a given value of ν. This guarantees a good enough, initial trial solution for an iterative procedure. We first rewrite equations in a more nice form of the Richardson equations for the constant density of states. Let us define

$$\begin{aligned} \varepsilon_k &= \varepsilon_{F_0} + \xi_k \qquad (5.16) \\ R_i &= 2\varepsilon_{F_0} + r_i, \qquad (5.17) \end{aligned}$$

and considering the constant density of states, *i. e.*,

$$\xi_n = 2n/\rho \ (n = 0, 1, \cdots, N_\Omega - 1), \qquad (5.18)$$

the Richardson equations can be rewritten as following:

$$\frac{2}{\rho V} = \sum_{n=0}^{N_\Omega - 1} \frac{1}{n + \rho r_j/2} + 4 \sum_{i \neq j} \frac{1}{\rho r_i - \rho r_j}. \qquad (5.19)$$

Now, new notations are introduced,

$$X_i = \frac{\rho r_i}{2}. \qquad (5.20)$$

Then, Eq. 5.21 becomes

$$\frac{2}{\nu} = \sum_{n=0}^{N_\Omega - 1} \frac{1}{n + X_j} + 4 \sum_{i \neq j} \frac{1}{X_i - X_j}. \qquad (5.21)$$

ν is independent on the system size and only depends on material. The typical value of ν is ~ 0.1

where $\nu = \rho V$ is a dimensionless interaction constant as mentioned previously. The total energy can be calculated by

$$E_N = \sum_j R_j = 2\varepsilon_{F_0} N - \sum_j r_j = 2\varepsilon_{F_0} N - \sum_{n=1}^{N} \frac{2}{\rho} X_n. \qquad (5.22)$$

In order to avoid the singularity, if $X_k, X_j \to n_0$ when $\nu \to \nu_c$, we introduced new variables λ_+ and λ_- [140]:

$$\lambda_+ = 2n_0 + X_k + X_j \tag{5.23}$$
$$\lambda_- = (X_k - X_j)^2, \tag{5.24}$$
$$\tag{5.25}$$

which are always real when X_k, X_j transit from real numbers to a complex conjugate pair (or vice-versa), *e. g.*, for $N = 50$ as shown in Fig. 5.1. Instead of the equations

$$\frac{2}{\nu} = \sum_{n=0}^{N_\Omega - 1} \frac{1}{n + X_k} + 4 \sum_{i \neq k} \frac{1}{X_i - X_k} \tag{5.26}$$
$$\frac{2}{\nu} = \sum_{n=0}^{N_\Omega - 1} \frac{1}{n + X_j} + 4 \sum_{i \neq j} \frac{1}{X_i - X_j}, \tag{5.27}$$

we transform them to the following two equations:

$$(\lambda_+^2 - \lambda_-) G1 + 4\lambda_+ = 0 \tag{5.28}$$
$$(\lambda_+^2 - \lambda_-) \lambda_- G2 - 4\lambda_- = 0 \tag{5.29}$$

Please note G1, G2 *are not divergent since the sum does not include divergent terms* $1/(X_k - X_j)$ *and* $1/(n + X_{k(j)})$.

with

$$G1 = -4/\nu + \sum_{n \neq n_0}^{N_\Omega - 1} \left(\frac{1}{n + X_k} + \frac{1}{n + X_j} \right) + 2 \sum_{i \neq k,j}^{N} \left(\frac{1}{X_i - X_k} + \frac{1}{X_i - X_j} \right) \tag{5.30}$$

$$G2 = - \sum_{n \neq n_0}^{N_\Omega - 1} \frac{1}{(n + X_k)(n + X_j)} + 2 \sum_{i \neq k,j}^{N} \frac{1}{(X_i - X_k)(X_i - X_j)}. \tag{5.31}$$

Then we solve the new equations and with the new set of variables λ_+, λ_-, $X_i (i \neq k, j)$. However, when ν is very close to ν_c, the Newton-Raphson result does not converge to the solution if it starts from the other side of the singularity [141]. Therefore, an ex-

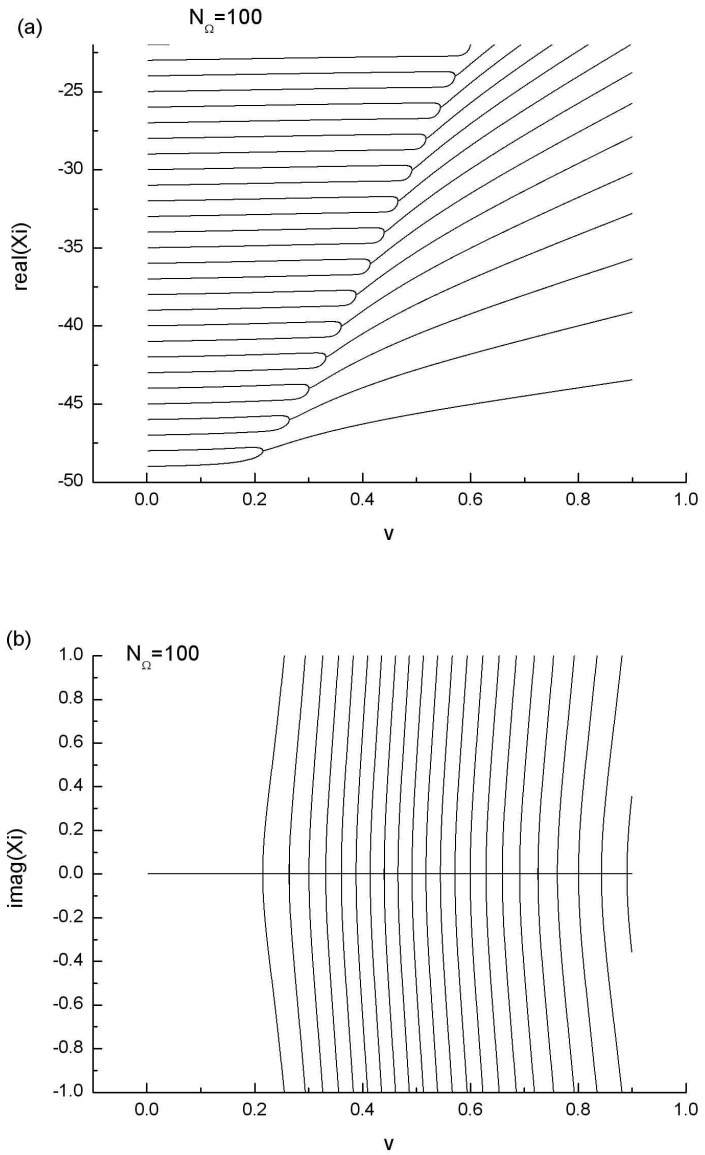

Figure 5.1: Real and imaginary parts of the solutions X_i when $N_\Omega = 2N = 100$.

trapolation step is taken for the new ν (close to ν_c), as proposed in Ref. [141]:

$$\lambda_{\pm} = \frac{(\nu - \nu')\lambda''_{\pm} - (\nu - \nu'')\lambda'_{\pm}}{\nu'' - \nu'} \tag{5.32}$$

where $\lambda'_{\pm}$, $\lambda''_{\pm}$ were obtained for the value ν', ν'', respectively.

After finding solutions of X_i $(i = 1, \cdots, N)$, we can calculate the energy E_N by Eq. 5.22 and compare the numerical result with the analytical results (Eqs. 5.14 and 5.15).

5.4 DISCUSSION

Let us now consider limits, for which Eq. 5.13 can be solved analytically, in order to see whether Eq. 5.15 gives reasonable results.

We start with the limit of the very weak coupling, in which the solution of Eq. 5.13 approaches the lowest level so closely that the mutual separation gets much smaller than $1/\rho$ and, moreover, contributions from other levels can be neglected. Then, we obtain a simple solution $\alpha_1 = -V$. By estimating dropped contributions of other levels, we get a criterion of applicability for this result as $\nu \ll 1/\ln(N_\Omega)$. In this case, $E_N^{(cond)}/N$ reduces to $-V$, as it must be, due to the cancellation in the RHS of Eq. 5.15. Note that the condensation energy per pair in this limit is independent on filling.

Next, we consider an opposite limit, when the separation between the single rapidity and the lowest level is much larger than $1/\rho$ and the number of levels N_Ω is also large. This enables us to replace the sum in the RHS of Eq. 5.13 by the integral, which gives

$$\alpha_1 = -2\Omega \frac{\exp(-2/\nu)}{1 - \exp(-2/\nu)}. \tag{5.33}$$

The condition of applicability for this result is thus twofold: $N_\Omega \gg 1$ and $N_\Omega \exp(-2/\nu)/(1 - \exp(-2/\nu)) \gg 1$. The infinite-sample limit, for which ν is fixed and finite, thus always satisfies these criteria. It is also easy to see that $|\alpha_1|$ given by Eq. 5.13 is much larger than V in the large-sample limit, $N_\Omega \longrightarrow \infty$, so that $V \sim |\alpha_1|/N_\Omega$. This means that in this limit V can be neglected in Eq. 5.15. Then,

$$E_N^{(cond)}/N \simeq -2\left(\Omega - \frac{N}{\rho}\right)\frac{exp(-2/\nu)}{1 - exp(-2/\nu)}, \tag{5.34}$$

which, for the half-filling, coincides with the BCS expression for the condensation energy per N (and with Richardson large-N result for the same filling [27, 26]). For arbitrary filling, it also coincides both with the mean-field treatment and with the results of the solution of Richardson equations [145, 146, 139].

We would like to stress that the obtained results are far from being trivial. Indeed, the condensation energy given by Eq. 5.15 consists of two terms. In the limit of a very weak coupling, both of them are of the same order, while their combination gives the exact result within all numerical prefactors. In contrast, in the large-sample limit $N_\Omega \longrightarrow \infty$, when interaction constant ν stays finite and nonzero, one of the terms becomes of the order of $1/N_\Omega$ compared to another one, so that it can be dropped as an underextensive contribution, while the remaining term again gives a correct answer within all numerical prefactors. Such a very subtle interplay between the two terms seems to indicate that the suggested formula for the condensation energy must stay accurate not only in the limits we consider.

Another nontrivial feature is that we actually obtain the information about the solution of the many-body problem without really solving it. Namely, we rely on the internal e-h symmetry of the Hamiltonian, make a conjecture on the general structure of the solution, and then reduce the task to the one-body problem. By doing this, we arrive to the correct results in known solvable limits.

In order to explore the applicability range of the obtained expression of the condensation energy, we perform a systematic numerical solution of the full set of Richardson equations, as given by Eq. 5.4, for various values of N (from 1 to 50) and ν at the half-filling. The numerical details has been discussed in Section 5.3. Then we compare the obtained numerical results with the prediction of Eq. 5.15. We also calculate condensation energy by using the standard grand-canonical BCS theory and make a comparison. The only one difference from the common version of this theory is in the fact that we do not replace sums by integrals when solving the gap equation and also when calculating the condensation energy itself, which is of importance for systems with relatively small number of pairs, since these replacements are responsible for additional errors.

α_1 is obtained from the numerical solution of Eq. 5.13.

The results are presented in Fig. 5.2 for two particular values of N. Condensation energies are measured in terms of $2/\rho$. Fig. 5.2(a) gives the dependence of the condensation energy per pair for $N = 5$, as a function of ν, while Fig. 5.2 (b) and (c) corresponds to $N = 25$ and $N = 50$, respectively. Solid curves represent results of numeri-

cal solution of Richardson equations, dashed curves yield our prediction, and dotted lines are grand-canonical BCS results. We see that there is a quite good agreement between the numerical results and our formula. The similar agreement has been found for other values of N. Although there is still some deviation for intermediate values of ν at given N, this discrepancy turns out to be small, so that our conjecture on the general structure of the solution is justified. Thus, our formula can be applied to the general (N, ν). In contrast, BCS results become accurate in the large-N limit only, as can be also seen by comparison of Fig. 5.2. In addition, as it is known, there is a range of small ν for any N, at which grand-canonical BCS theory is qualitatively incorrect, since it predicts a disappearance of superconducting correlations: In other words, the gap equation has no solution, so that the condensation energy is zero, see Fig. 5.2. In this fluctuation-dominated regime, our approach works fairly well. Note that there exists a number-projected BCS approach, which is able to significantly improve mean-field predictions, but it is based on a rather heavy numerics. We also would would like to stress that the equally-spaced model can be treated as a toy model only for the real finite-N systems.

Our analytical formula contains one parameter to be found numerically by solving a single Richardson equation. Such a task is definitely far simpler than the solution of the whole set of Richardson equations. The procedure we suggest is definitely not a naive fitting, since we do not impose any specific dependencies of the energy as a function of V in known limiting cases. Instead, we somehow derive them, including a nonanalytic dependence of Eq. 5.34, based on our conjecture on the N-dependence of the solution.

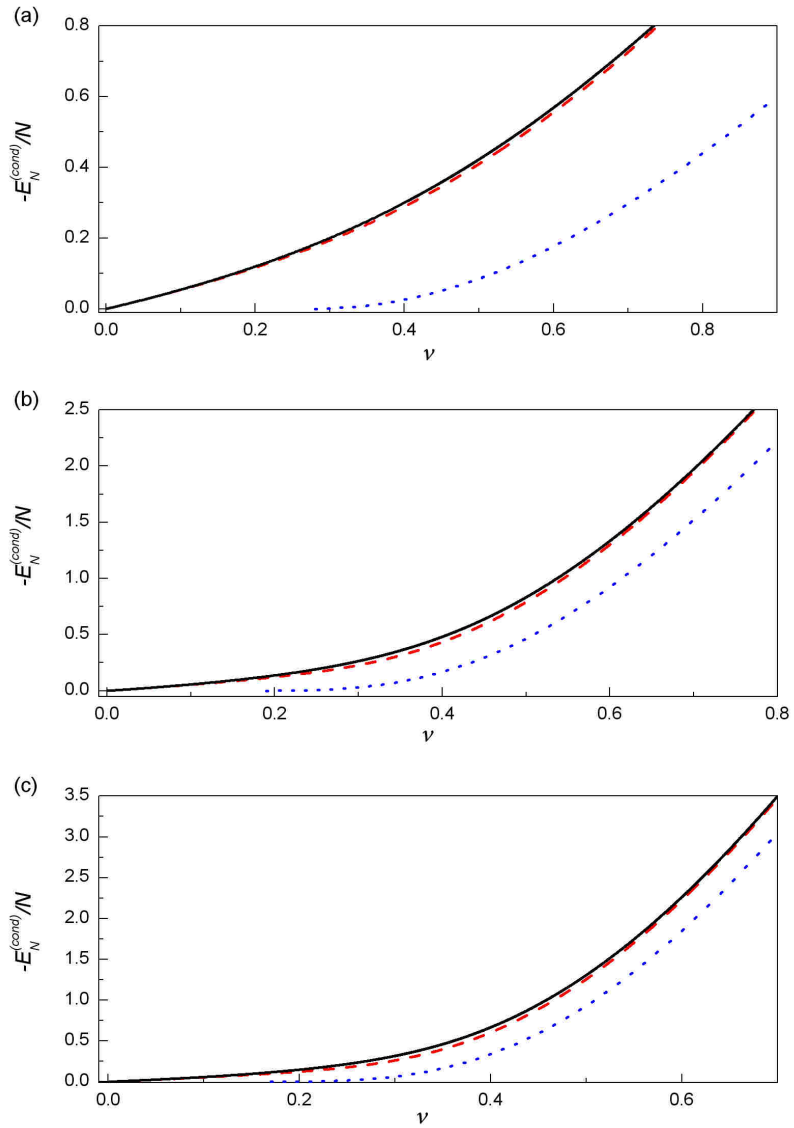

Figure 5.2: The dependence of the condensation energy per pair as a function of the interaction constant. (a) corresponds to the system with 5 pairs, while (b) - to the system of 25 pairs and (c) - to the system of 50 pairs. Solid line represents the results of the numerical resolution of the whole system of Richardson equations, dashed line gives the prediction according to our analytical formula, dotted line corresponds to the grand-canonical BCS result.

6

SUMMARY AND OUTLOOK

In this thesis, we studied the dynamics of clusters of various constituents - either vortices or electron/hole pairs - in low-dimensional superconductors. The interplay between the interaction in clusters, the confinement and driving forces results in a complex dynamical behavior.

In Chapter 3, the process of angular melting was investigated in a system with multi-shell (typically, three to five shells) vortex configurations. By analysing the dynamical process, we have found following interesting behaviors. First, different scenarios of angular melting were found for different configurations. By analyzing the average angular velocity of the vortices in each shell, we found that either an inner shell or an outer shell can first unlock (*i. e.*, the shell starts to rotate with different angular velocity with respect to the other shells); the former represents an usual ("classical") scenario of angular melting, the latter is referred to as "unconventional" angular melting. Because of a larger friction between two commensurate shells than between incommensurate shells, the commensurability plays an important role in the angular melting process. Then, besides all-commensurate-shell configurations (*i. e.*, the magic-number configurations), we investigated two kinds of imperfect-six-fold systems, which include intra-shell defect(s) and inter-shell defect(s), respectively. An intra-shell defect can cause an inversion of the angular velocities of the shells, i.e., when a shell which is closer to the center and thus experiences a larger Lorentz force moves slower than the adjacent shell with larger radius. To understand this unusual behavior, we distinguished three phases in the angular melting process. The above unconventional dynamics is observed only in one of those phases, namely, during the "compression-decompression motion". When an extra (defect) vortex is present that shifts the other vortices from their triangular-lattice positions, a part of the shell becomes nearly

circle-like whereas another part keeps the hexagonal shape. In this case, the local shear modulus becomes angle-dependent. Therefore, when the shear stress is not large enough to unlock the whole defect shell, the shell is partly melted and induces a very particular dynamical behavior, i.e., the motion in the form of a propagating compression-decompression wave. An inter-shell defect always locks several shells which rotate together up to some critical current. When the shear stress finally breaks the radial vortex line(s) containing defect(s), all shells that were locked by the defect release and start rotating “individually" with different angular velocities. Furthermore, such a lock-unlock process causes a hysteresis effect in the angular velocities of the shells. Therefore, different angular velocities of vortex shells have been found depending on the history, *i. e.*, whether the applied current is increased or decreased.

In Chapter 4, we have investigated the motion of vortices in an asymmetric circular channel. A vortex moving in such an channel in a Corbino setup experiences the confinement of the boundary, the repulsive interaction due to other vortices and the gradient (*i. e.*, radially decreasing) driving force when an external current is applied. The combination of these factors determines the vortex motion. Different dynamical behavior is observed in low and high density systems, which are referred to as “single-vortex" and “multi-vortex" regimes, respectively. For low density, *i. e.*, in the single-vortex regime, there is no more than one vortex per triangular cell so that the vortex-vortex interaction is negligible. Therefore, the ratchet potential due to the boundary dominates and all the vortices follow circular 1D trajectories. Since all the vortices still move in 1D when there is more than one vortex per cell (*i. e.*., a higher density), a vortex can escape even easier either in the easy or in the hard direction due to the interaction between vortices in the same cell. This results in decrease of the rectified net current. However, when the number of vortices increases further (*i. e.*, in the“multi-vortex" regime of rectification when the rectified net current increases with the vortex density), the trajectories of vortex motion for low driving currents are 2D while these trajectories squeeze and turn to 1D circle with increasing driving current. Because of the circular geometry of the channel, the density of vortices first becomes inhomogeneous [*i. e.*, see Fig. 4.5(b)] during the transition from 2D motion to 1D motion in the multi-vortex regime and then becomes homogeneous again when all the vortices move in a circular trajectory.

Considering the asymmetry in the radial direction, vortices near the inner/outer corner of the triangular cells (TCs) (*i. e.*, closer/fur-

ther to the center of the disk) are driven by different Lorentz forces and for some specific value of driving current the vortex in the outer corner moves to the inner corner while the one in the inner corner moves to the next TC [*e. g.*, see Fig. 4.5(a)]. This kind of motion prevents vortices from arriving simultaneously at the narrow part that would lead to jamming which occurs in case of a linear channel. When the density increases, the maximum net angular velocity ω_m remains the same in the single-vortex regime and then decreases until reaching the multi-vortex regime, and then ω_m increases.

The frequency of driving current also strongly influences the vortex dynamical behavior. The ac frequency determines the possible distance a vortex moves during an ac period. For high frequency, a nearly zero net angular velocity is obtained for different values of driving current I_0. Each vortex is unable to overcome the energy barrier and is confined by a single potential well instead of the periodic ratchet potential. When the frequency is low, the ratchet effect is clearly observed in the $\omega - I_0$ curve but the commensurability effect is not present. For an intermediate frequency of driving current under which the distance of moving vortex in a period is comparable to the size of the TC, both the ratchet effect and the commensurability effect have been observed.

Besides the vortex density and the frequency of current, the commensurability between the numbers of vortices and TCs also plays an important role in the dynamical behavior of vortices, which leads to jumps in the angular velocity ω with increasing driving current I_0 (i.e., steps in the $\omega - I_0$ curve). Therefore, under some specific conditions, the average angular velocity of vortices is not a continuous function of the driving current. The commensurability also influences the minimum difference of the angular velocity for different steps in the $\omega - I_0$ curve, and results in integer steps (*i. e.*, the large steps which are found, *e. g.*, for vorticity $L = 1$) and fractional steps (*i. e.*, the smaller steps whose magnitude are fractions of the magnitude of the integer steps, *e. g.*, for vorticity $L = 24$) in a certain range of the current. We also obtained several peaks (sharp jumps) in the $\omega - t$ curve, which correspond to the principal period t_0 (during which the vortex can move over one TC in the easy direction), and harmonics periods $k\nu_0$ $(k = 2, 3, ...)$ (during which vortices move over k TCs in the easy direction). The net flow of vortices is enhanced when the ac period is one of the harmonics periods, *i. e.*, the average angular velocity reaches a local maximum.

In Chapter 5, we suggested an analytical expression of the ground state energy of the BCS Hamiltonian for the case of the equally-

spaced model at the arbitrary number of pairs and interaction constant, *i.e.*, along the whole crossover from the superconducting regime to the pairing fluctuation regime. This expression is derived from the electron-hole symmetry of the Hamiltonian and relies on a certain conjecture on the N-dependence of the dominant part of the ground state energy. The expression of the ground state energy depends on the binding energy of a single pair, which, in general case, must be determined numerically. The latter problem is definitely far simpler than the solution of the whole set of Richardson equations.

The whole set of Richardson equations have been solved by numerical approach, while the results by the usual grand-canonical BCS approach is also calculated. The comparison the expression with the results of the full numerical resolution of Richardson equations demonstrated a high accuracy of the suggested formula, while the usual grand-canonical BCS approach fails in fluctuation-dominated regime.

There are several interesting tasks to accomplish related to our works on superconducting Corbino disks. In particular, we can introduce random and/or regular pinning sites in order to study the dynamical behavior. This is motivated by the fact that pinning is always present in real systems in experiment. Partially, this issue has been addressed in Ref. [44], where a random pinning was introduced to study the melting of vortex solid. Thus, the idea is to focus on regular pinning arrays which can also be relevant to recent experimental attempts with large Corbino disks. In addition, considering large disks can be potentially useful for understanding of the observed structure transition in large Corbino disks in the mode-locking experiments. Another promising direction will be to study artificially created shells in rather large Corbino disks which are believed to bridge small mesoscopic disks, where we found vortex shell structure, and macroscopic disks which can be measured in experiments.

A

APPENDIX: THE FREE ENERGY IN THE LONDON LIMIT

To study the free energy of vortex configuration in the London limit, we followed the approach of Refs. [33] and [35]. The Gibbs free energy in a superconductor is given by

$$\mathscr{F} = \frac{1}{8\pi}\int[(\mathbf{H}-\mathbf{H}_0)^2 + \lambda^2(\nabla\times\mathbf{H})^2]d^3r \tag{A.1}$$

In the thin-film limit, *i. e.*, $d \ll R$,

d *is the thickness of the disk and* R *is the radius.* J *is the sheet current inside the film.*

$$\mathbf{A}_0 = \mathbf{H}_0\times\boldsymbol{\rho}/2 \tag{A.2}$$

$$\Lambda_{eff} = \lambda^2/d \tag{A.3}$$

$$\mathbf{J} = \int_0^d(\nabla\times\mathbf{H})dz = \int_0^d \mathbf{j}dz \approx \mathbf{j}d, \tag{A.4}$$

and using $\mathbf{H}-\mathbf{H}_0 = \nabla\times(\mathbf{A}-\mathbf{A}_0)$, we rewrite Eq. A.1 as

$\mathbf{A}$ *is the vector potential.*

$$\mathscr{F} = \frac{1}{8\pi}\int\left[(\frac{4\pi}{c}\mathbf{J})(\mathbf{A}-\mathbf{A}_0) + \frac{4\pi\Lambda_{eff}}{c}\mathbf{J}\right]d^2\rho. \tag{A.5}$$

For an extreme type-II superconducting thin disk ($\Lambda_{eff} \gg R$), we may consider the magnetic field to be homogeneous, *i. e.*, $\mathbf{A} \approx \mathbf{A}_0$. Thus, neglecting demagnetization effects, we can rewrite the London equation with N vortices (in the London gauge $\nabla\cdot\mathbf{A} = 0$) as

ρ_i *is the position of vortex* i.

$$\mathbf{J} = \frac{c}{4\pi\Lambda_{eff}}\left(\sum_{i=1}^{N}\boldsymbol{\Phi}(|\boldsymbol{\rho}-\boldsymbol{\rho}_i|) - \mathbf{A}\right), \tag{A.6}$$

with the boundary condition

$$\mathbf{J}(R)\cdot\boldsymbol{\rho} = 0. \tag{A.7}$$

In order to satisfy the zero normal current flow to the disk boundary as Eq. A.7, vortex images located at $(R/\rho_i)^2\boldsymbol{\rho_i}$ outside of the disk are introduced, so we have

$$\boldsymbol{\Phi} = \sum_{i=1} N[\Phi(|\boldsymbol{\rho} - \boldsymbol{\rho}_i|) - \Phi(|\boldsymbol{\rho} - (R/\rho_i)^2\boldsymbol{\rho}_i|)]. \tag{A.8}$$

By substituting Eq. A.5 into Eq. A.6, we can find

$$\mathscr{F} = \frac{1}{8\pi\Lambda_{eff}} \int (\boldsymbol{\Phi} - \mathbf{A}_0)^2 d^2\rho = \frac{2\pi\Lambda_{eff}}{c^2} \int \mathbf{J}^2 d^2\rho. \tag{A.9}$$

It is useful to rewrite the free energy in terms of the function $g(\boldsymbol{\rho})$ (that can be regarded as a local magnetization in a thin film) with

$$\begin{aligned} \mathbf{J} &= \nabla \times (g\hat{z}) \\ g(R, \Phi) &= 0. \end{aligned}$$

Thus,

$$\mathscr{F} = \frac{2\pi\Lambda_{eff}}{c^2} \int g(\rho)\hat{z} \cdot \nabla \times \mathbf{J} d^2\rho = \frac{1}{2c} \left[\Phi_0 \sum_{i=1}^{N} g(\rho) - H_0 \int g(\rho) d^2\rho \right]. \tag{A.10}$$

By substituting Eqs. A.6 and A.8, we can find that

$$g(\rho_i) = \frac{c}{4\pi\Lambda_{eff}} \left[\frac{\Phi_0}{2\pi} \sum_{i=1}^{N} \ln \left(\frac{|\boldsymbol{\rho}_i - (R/\rho_j)^2\boldsymbol{\rho}_j|}{|\boldsymbol{\rho}_i - \boldsymbol{\rho}_j|} \cdot \frac{\boldsymbol{\rho}_j}{R} \right) - \frac{H_0}{4}(R^2 - \rho^2) \right]. \tag{A.11}$$

Substituting Eq. A.11 in Eq. A.10 and using the following relation,

$$\int \ln \left(\frac{|\boldsymbol{\rho}_i - (R/\rho_j)^2\boldsymbol{\rho}_j|}{|\boldsymbol{\rho}_i - \boldsymbol{\rho}_j|} \right) = \frac{\pi}{2}(R^2 - \rho_j^2) + \pi R^2 \ln(R/\rho_j), \tag{A.12}$$

we can rewrite $\mathscr{F}$ as

In Eq. A.13 and the following equations, the energy is in units of $\Phi_0^2/16\pi\Lambda_{eff}$.

$$\mathscr{F} = \sum_{i=1}^{N} \sum_{j=1}^{N} \ln \left(\frac{|\boldsymbol{\rho}_i - (R/\rho_j)^2\boldsymbol{\rho}_j|}{|\boldsymbol{\rho}_i - \boldsymbol{\rho}_j|} \cdot \frac{\boldsymbol{\rho}_j}{R} \right) - \frac{1}{2} H_0 \sum_{i=1}^{N} (R^2 - \rho_i^2) + \left(\frac{R^2 H_0}{4} \right)^2. \tag{A.13}$$

When $i = j$ in Eq. A.13, $|\rho_i - \rho_j| \to 0$ which results in a divergent term. In order to remove the divergence, a cutoff procedure is employed: $|\rho_i - \rho_j| = \xi$ when $i = j$. Thus,

$$\mathscr{F} = \sum_{i=1}^{N} \sum_{j=1, i\neq j}^{N} \ln\left(\frac{|\boldsymbol{\rho}_i - (R/\rho_j)^2 \boldsymbol{\rho}_j|}{|\boldsymbol{\rho}_i - \boldsymbol{\rho}_j|} \cdot \frac{\boldsymbol{\rho}_j}{R}\right) + \sum_{i=1}^{N} \left[\ln(1 - (\rho_i/R)^2) - \frac{1}{2} H_0 (R^2 - \rho_i^2)\right] + \left(\frac{R^2 H_0}{4}\right)^2 + N \ln(R/a). \tag{A.14}$$

One can rewrite Eq. A.14 with dimensionless positions $r_{i(j)} = \rho_{i(j)}/R$,

$$\mathscr{F} = \sum_{i=1}^{N} \sum_{j=1, i\neq j}^{N} \ln\left(\frac{(r_i r_j)^2 - 2\mathbf{r}_i \cdot \mathbf{r}_j + 1}{r_i^2 - 2\mathbf{r}_i \cdot \mathbf{r}_j + r_j^2|} \cdot \frac{\boldsymbol{\rho}_j}{R}\right) + \sum_{i=1}^{N} \left[\ln(1 - r_i^2) - \frac{R^2 H_0}{2}(1 - r_i^2)\right] + \left(\frac{R^2 H_0}{4}\right)^2 + N \ln(R/a). \tag{A.15}$$

In the above expression, the first term is due to the vortex-vortex interaction; the second and third terms are due to the shielding current and the edges; the external magnetic-field energy interaction is calculated by the forth term, and the last term corresponds to the energy of the vortex cores. Therefore, we can model the interaction force between vortices, which is derived from the first term of Eq. A.15, as

$$\mathbf{f}_{ik}^{vv} = f_0 \left(\frac{\mathbf{r}_i - \mathbf{r}_k}{|\mathbf{r}_i - \mathbf{r}_k|^2} - r_k^2 \frac{r_k^2 \mathbf{r}_i - \mathbf{r}_k}{|r_k^2 \mathbf{r}_i - \mathbf{r}_k|^2}\right), \tag{A.16}$$

where f_0 is the unit of force as described in Chapter. 3.

BIBLIOGRAPHY

[1] Z. L. Wang, *Nanowires and nanobelts materials, properties and devices metal and semiconductor nanowires*, vol. I. Kluwer Academic Publishers, 2003.

[2] R. Prozorov, R. W. Giannetta, A. Carrington, P. Fournier, R. L. Greene, P. Guptasarma, D. G. Hinks, and A. R. Banks, "Measurements of the absolute value of the penetration depth in high-T_c superconductors using a low-T_c superconductive coating," *Applied Physics Letters*, vol. 77, pp. 4202 –4204, Dec. 2000.

[3] L. D. Landau, "Theory of phase transformations. I," *Zh. Eksp. Teor. Fiz*, vol. 7, p. 19, 1937.

[4] L. D. Landau, "Theory of phase transformations. II," *Zh. Eksp. Teor. Fiz*, vol. 627, p. 1973, 1937.

[5] L. D. Landau, "Theory of supraconductivity," *Zh. Eksp. Teor. Fiz.*, vol. 7, p. 371, 1937.

[6] V. L. Ginzburg and L. D. Landau, "On the theory of superconductivity," *Zh. Eksp. Teor. Fiz.*, vol. 20, p. 1064, 1950.

[7] M. Tinkham, *Introduction to superconductivity*. McGraw-Hill, Inc., 1996.

[8] A. A. Abrikosov, "On the magnetic properties of superconductors of the second group," *Sov Phys JETP*, vol. 5, no. 6, p. 1174, 1957.

[9] J. Bardeen, L. N. Cooper, and J. R. Schrieffer, "Microscopic theory of superconductivity," *Physical Review*, vol. 106, pp. 162–164, Apr 1957.

[10] L. P. Gor'kov, "Microscopic derivation of the Ginzburg-Landau equations in the theory of superconductivity," *Sov.-Phys. JETP*, vol. 36, pp. 1918–1923, Jun. 1959.

[11] L. N. Cooper, "Bound electron pairs in a degenerate Fermi gas," *Physical Review*, vol. 104, pp. 1189–1190, Nov 1956.

[12] J. B. Ketterson and S. N. Song, *Superconductivity*. Cambridge University Press, 1999.

[13] J. Dukelsky, S. Pittel, and G. Sierra, "Colloquium: Exactly solvable Richardson-Gaudin models for many-body quantum systems," *Reviews of Modern Physics*, vol. 76, pp. 643–662, Aug. 2004.

[14] K. Dietrich, H. J. Mang, and J. H. Pradal, "Conservation of particle number in the nuclear pairing model," *Physical Review*, vol. 135, pp. B22–B34, Jul 1964.

[15] F. Braun and J. von Delft, "Fixed-N superconductivity: The crossover from the bulk to the few-electron limit," *Physical Review Letters*, vol. 81, pp. 4712–4715, Nov 1998.

[16] J. Dukelsky and G. Sierra, "Density matrix renormalization group study of ultrasmall superconducting grains," *Physical Review Letters*, vol. 83, pp. 172–175, July 1999.

[17] R. Richardson, "A restricted class of exact eigenstates of the pairing-force Hamiltonian," *Physics Letters*, vol. 3, pp. 277–279, Feb. 1963.

[18] R. Richardson, "Application to the exact theory of the pairing model to some even isotopes of lead," *Physics Letters*, vol. 5, pp. 82–84, June 1963.

[19] R. Richardson and N. Sherman, "Exact eigenstates of the pairing-force Hamiltonian," *Nuclear Physics*, vol. 52, pp. 221–238, Mar. 1964.

[20] R. W. Richardson, "Exact eigenstates of the pairing-force Hamiltonian II," *Journal of Mathematical Physics*, vol. 6, pp. 1034–1051, July 1965.

[21] R. W. Richardson, "Numerical study of the 8-32-particle eigenstates of the pairing Hamiltonian," *Physical Review*, vol. 141, pp. 949–956, Jan 1966.

[22] R. W. Richardson, "Exactly solvable many-Boson model," *Journal of Mathematical Physics*, vol. 9, pp. 1327–1343, Sept. 1968.

[23] G. Sierra, "Conformal field theory and the exact solution of the BCS Hamiltonian," *Nuclear Physics B*, vol. 572, pp. 517–534, Apr. 2000.

[24] V. N. Gladilin, J. Tempere, I. F. Silvera, J. T. Devreese, and V. V. Moshchalkov, "Vortices on a superconducting nanoshell: Phase diagram and dynamics," *Phys. Rev. B*, vol. 77, p. 024512, Jan 2008.

[25] V. Gladilin, J. Tempere, J. Devreese, and V. Moshchalkov, "Negative-μ regime in the ac magnetic response of superconductor nanoshells," *Solid State Communications*, vol. 152, pp. 1781–1785, Sept. 2012.

[26] M. Gaudin, "Diagonalisation d'une classe d'Hamiltoniens de spin," *Journal de Physique*, vol. 37, no. 10, pp. 1087–1098, 1976.

[27] R. W. Richardson, "Pairing in the limit of a large number of particles," *Journal of Mathematical Physics*, vol. 18, pp. 1802–1811, Sept. 1977.

[28] M. Schechter, Y. Imry, Y. Levinson, and J. v. Delft, "Thermodynamic properties of a small superconducting grain," *Physical Review B*, vol. 63, p. 214518, May 2001.

[29] J. Dukelsky and S. Pittel, "New mechanism for the enhancement of *sd* dominance in interacting Boson models," *Physical Review Letters*, vol. 86, pp. 4791–4794, May 2001.

[30] J. Dukelsky, C. Esebbag, and P. Schuck, "Class of exactly solvable pairing models," *Physical Review Letters*, vol. 87, p. 066403, July 2001.

[31] J. Dukelsky and P. Schuck, "Condensate fragmentation in a new exactly solvable model for confined Bosons," *Physical Review Letters*, vol. 86, pp. 4207–4210, May 2001.

[32] J. Tempere, V. N. Gladilin, I. F. Silvera, and J. T. Devreese, "Cooper pairing and superconductivity on a spherical surface: Applying the Richardson model to a multielectron bubble in liquid helium," *Physical Review B*, vol. 72, p. 094506, Sept. 2005.

[33] A. Buzdin and J. Brison, "Vortex structures in small superconducting disks," *Physics Letters A*, vol. 196, pp. 267–271, Dec. 1994.

[34] B. J. Baelus, L. R. E. Cabral, and F. M. Peeters, "Vortex shells in mesoscopic superconducting disks," *Physical Review B*, vol. 69, p. 064506, Feb. 2004.

[35] L. R. E. Cabral, B. J. Baelus, and F. M. Peeters, "From vortex molecules to the Abrikosov lattice in thin mesoscopic superconducting disks," *Physical Review B*, vol. 70, p. 144523, Oct. 2004.

[36] V. R. Misko, B. Xu, and F. M. Peeters, "Formation and size dependence of vortex shells in mesoscopic superconducting niobium disks," *Physical Review B*, vol. 76, p. 024516, July 2007.

[37] D. López, W. K. Kwok, H. Safar, R. J. Olsson, A. M. Petrean, L. Paulius, and G. W. Crabtree, "Spatially resolved dynamic correlation in the vortex state of high temperature superconductors," *Physical Review Letters*, vol. 82, pp. 1277–1280, Feb. 1999.

[38] G. W. Crabtree, D. Lopez, W. K. Kwok, H. Safar, and L. M. Paulius, "Dynamic correlation in driven vortex phases," *Journal of Low Temperature Physics*, vol. 117, pp. 1313–1322, 1999.

[39] S. F. W. R. Rycroft, R. A. Doyle, D. T. Fuchs, E. Zeldov, R. J. Drost, P. H. Kes, T. Tamegai, S. Ooi, and D. T. Foord, "Bulk transport properties of $Bi_2Sr_2CaCu_2O_8$ crystals in the Corbino disk geometry," *Physical Review B*, vol. 60, pp. R757–R760, July 1999.

[40] Y. Paltiel, E. Zeldov, Y. Myasoedov, M. L. Rappaport, G. Jung, S. Bhattacharya, M. J. Higgins, Z. L. Xiao, E. Y. Andrei, P. L. Gammel, and D. J. Bishop, "Instabilities and disorder-driven first-order transition of the vortex lattice," *Physical review letters*, vol. 85, pp. 3712–3715, Oct. 2000.

[41] A. A. Babaei Brojeny and J. R. Clem, "Magnetization of a current-carrying superconducting Corbino disk," *Physical Review B*, vol. 64, p. 184507, Oct. 2001.

[42] P. Benetatos and M. C. Marchetti, "Plasticity in current-driven vortex lattices," *Physical Review B*, vol. 65, p. 134517, Mar. 2002.

[43] M.-C. Miguel and S. Zapperi, "Tearing transition and plastic flow in superconducting thin films," *Nature materials*, vol. 2, pp. 477–81, July 2003.

[44] V. R. Misko and F. M. Peeters, "Dynamics of vortex shells in mesoscopic superconducting Corbino disks," *Physical Review B*, vol. 74, p. 174507, Nov. 2006.

[45] J. Yan and M. S. Fuhrer, "Charge transport in dual gated bilayer graphene with Corbino geometry," *Nano Letters*, vol. 10, pp. 4521–4525, 2010.

[46] S. Okuma, S. Morishima, and M. Kamada, "Dynamic transition and metastability in the nonlinear $I-V$ regime in a Corbinodisk superconductor," *Physical Review B*, vol. 76, p. 224521, Dec. 2007.

[47] V. R. Misko, S. Savel'ev, A. L. Rakhmanov, and F. Nori, "Negative differential resistivity in superconductors with periodic arrays of pinning sites," *Physical Review B*, vol. 75, p. 024509, Jan. 2007.

[48] I. V. Grigorieva, W. Escoffier, J. Richardson, L. Y. Vinnikov, S. Dubonos, and V. Oboznov, "Direct observation of vortex shells and magic numbers in mesoscopic superconducting disks," *Physical Review Letters*, vol. 96, p. 077005, Feb. 2006.

[49] I. V. Grigorieva, W. Escoffier, V. R. Misko, B. J. Baelus, F. M. Peeters, L. Y. Vinnikov, and S. V. Dubonos, "Pinning-induced formation of vortex clusters and giant vortices in mesoscopic superconducting disks," *Physical Review Letters*, vol. 99, p. 147003, Oct. 2007.

[50] M.-C. Miguel, A. Mughal, and S. Zapperi, "Laminar flow of a sheared vortex crystal: Scars in flat geometry," *Physical Review Letters*, vol. 106, p. 245501, June 2011.

[51] S. Okuma, Y. Yamazaki, and N. Kokubo, "Dynamic response and ordering of rotating vortices in superconducting Corbino disks," *Physical Review B*, vol. 80, p. 220501(R), Dec. 2009.

[52] V. M. Bedanov and F. M. Peeters, "Ordering and phase transitions of charged particles in a classical finite two-dimensional system," *Physical Review B*, vol. 49, pp. 2667–2676, Jan. 1994.

[53] S. W. S. Apolinario, B. Partoens, and F. M. Peeters, "Inhomogeneous melting in anisotropically confined two-dimensional clusters," *Physical Review E*, vol. 74, p. 031107, Sept. 2006.

[54] K. Nelissen, B. Partoens, I. Schweigert, and F. M. Peeters, "Induced order and re-entrant melting in classical two-dimensional binary clusters," *Europhysics Letters (EPL)*, vol. 74, pp. 1046–1052, June 2006.

[55] N. Lin, V. Misko, and F. Peeters, "Unconventional vortex dynamics in mesoscopic superconducting Corbino disks," *Physical Review Letters*, vol. 102, p. 197003, May 2009.

[56] J. Limburg, J. Das, S. Schippers, R. Hoekstra, and R. Morgenstern, "Coster-Kronig transitions in hollow atoms created during highly charged ion-surface interactions," *Physical Review Letters*, vol. 73, pp. 786–789, Aug. 1994.

[57] E. R. Dufresne, D. Altman, and D. G. Grier, "Brownian dynamics of a sphere between parallel walls," *Europhysics Letters (EPL)*, vol. 53, pp. 264–270, Jan. 2001.

[58] E. R. Dufresne, T. M. Squires, M. P. Brenner, and D. G. Grier, "Hydrodynamic coupling of two Brownian spheres to a planar surface," *Physical Review Letters*, vol. 85, pp. 3317–3320, Oct. 2000.

[59] R. D. Astumian, "Adiabatic pumping mechanism for ion motive ATPases," *Physical Review Letters*, vol. 91, p. 118102, Sept. 2003.

[60] D. Y. Vodolazov and F. M. Peeters, "Superconducting rectifier based on the asymmetric surface barrier effect," *Physical Review B*, vol. 72, p. 172508, Nov. 2005.

[61] P. Hänggi and F. Marchesoni, "Artificial Brownian motors: Controlling transport on the nanoscale," *Reviews of Modern Physics*, vol. 81, pp. 387–442, Mar. 2009.

[62] S. Savel'ev, V. Misko, F. Marchesoni, and F. Nori, "Separating particles according to their physical properties: Transverse drift of underdamped and overdamped interacting particles diffusing through two-dimensional ratchets," *Physical Review B*, vol. 71, p. 214303, June 2005.

[63] K. Yu, T. W. Heitmann, C. Song, M. P. DeFeo, B. L. T. Plourde, M. B. S. Hesselberth, and P. H. Kes, "Asymmetric weak-pinning superconducting channels: Vortex ratchets," *Physical Review B*, vol. 76, p. 220507, Dec. 2007.

[64] J. F. Wambaugh, C. Reichhardt, C. J. Olson, F. Marchesoni, and F. Nori, "Superconducting fluxon pumps and lenses," *Physical Review Letters*, vol. 83, pp. 5106–5109, Dec. 1999.

[65] B. Plourde, "Nanostructured superconductors with asymmetric pinning potentials: Vortex ratchets," *IEEE Transactions on Applied Superconductivity*, vol. 19, pp. 3698 –3714, Oct. 2009.

[66] C. C. de Souza Silva, J. V. d. Vondel, M. Morelle, and V. V. Moshchalkov, "Controlled multiple reversals of a ratchet effect," *Nature*, vol. 440, pp. 651–654, Mar. 2006.

[67] J. E. Villegas, S. Savel'ev, F. Nori, E. M. Gonzalez, J. V. Anguita, R. García, and J. L. Vicent, "A superconducting reversible rectifier that controls the motion of magnetic flux quanta," *Science*, vol. 302, pp. 1188–1191, Nov. 2003.

[68] J. E. Villegas, E. M. Gonzalez, M. P. Gonzalez, J. V. Anguita, and J. L. Vicent, "Experimental ratchet effect in superconducting films with periodic arrays of asymmetric potentials," *Physical Review B*, vol. 71, p. 024519, Jan. 2005.

[69] J. Van de Vondel, C. C. de Souza Silva, B. Y. Zhu, M. Morelle, and V. V. Moshchalkov, "Vortex-rectification effects in films with periodic asymmetric pinning," *Physical Review Letters*, vol. 94, p. 057003, Feb. 2005.

[70] B. B. Jin, B. Y. Zhu, R. Wördenweber, C. C. de Souza Silva, P. H. Wu, and V. V. Moshchalkov, "High-frequency vortex ratchet effect in a superconducting film with a nanoengineered array of asymmetric pinning sites," *Physical Review B*, vol. 81, p. 174505, May 2010.

[71] K. Yu, M. B. S. Hesselberth, P. H. Kes, and B. L. T. Plourde, "Vortex dynamics in superconducting channels with periodic constrictions," *Physical Review B*, vol. 81, p. 184503, May 2010.

[72] R. Wördenweber, P. Dymashevski, and V. R. Misko, "Guidance of vortices and the vortex ratchet effect in high-T_c superconducting thin films obtained by arrangement of antidots," *Physical Review B*, vol. 69, p. 184504, May 2004.

[73] J. Van de Vondel, V. N. Gladilin, A. V. Silhanek, W. Gillijns, J. Tempere, J. T. Devreese, and V. V. Moshchalkov, "Vortex core deformation and stepper-motor ratchet behavior in a superconducting aluminum film containing an array of holes," *Physical Review Letters*, vol. 106, p. 137003, Mar. 2011.

[74] Y. Togawa, K. Harada, T. Akashi, H. Kasai, T. Matsuda, F. Nori, A. Maeda, and A. Tonomura, "Direct observation of rectified motion of vortices in a niobium superconductor," *Physical Review Letters*, vol. 95, p. 087002, Aug. 2005.

[75] C. J. Olson, C. Reichhardt, B. Jankó, and F. Nori, "Collective interaction-driven ratchet for transporting flux quanta," *Physical Review Letters*, vol. 87, p. 177002, Oct. 2001.

[76] W. Gillijns, A. V. Silhanek, V. V. Moshchalkov, C. J. O. Reichhardt, and C. Reichhardt, "Origin of reversed vortex ratchet motion," *Physical Review Letters*, vol. 99, p. 247002, Dec. 2007.

[77] P. Hänggi and F. Marchesoni, "Introduction: 100 years of Brownian motion," *Chaos: An Interdisciplinary Journal of Nonlinear Science*, vol. 15, pp. 026101–026101–5, June 2005.

[78] P. Hänggi, F. Marchesoni, and F. Nori, "Brownian motors," *Annalen der Physik*, vol. 14, no. 1-3, pp. 51–70, 2005.

[79] D. Cole, S. Bending, S. Savel'ev, A. Grigorenko, T. Tamegai, and F. Nori, "Ratchet without spatial asymmetry for controlling the motion of magnetic flux quanta using time-asymmetric drives," *Nature Materials*, vol. 5, no. 4, pp. 305–311, 2006.

[80] C. Reichhardt, C. J. Olson, and F. Nori, "Dynamic phases of vortices in superconductors with periodic pinning," *Physical Review Letters*, vol. 78, p. 2648, Mar. 1997.

[81] C. Reichhardt, C. J. Olson, and F. Nori, "Commensurate and incommensurate vortex states in superconductors with periodic pinning arrays," *Physical Review B*, vol. 57, p. 7937, 1998.

[82] C. Reichhardt, C. J. Olson, and F. Nori, "Nonequilibrium dynamic phases and plastic flow of driven vortex lattices in superconductors

with periodic arrays of pinning sites," *Physical Review B*, vol. 58, pp. 6534–6564, Apr. 1998.

[83] V. R. Misko, S. Savel'ev, A. L. Rakhmanov, and F. Nori, "Nonuniform self-organized dynamical states in superconductors with periodic pinning," *Physical Review Letters*, vol. 96, p. 127004, Mar. 2006.

[84] C. J. Olson Reichhardt and C. Reichhardt, "Commensurability, jamming, and dynamics for vortices in funnel geometries," *Physical Review B*, vol. 81, p. 224516, Jun 2010.

[85] C. Reichhardt and C. O. Reichhardt, "Jamming and diode effects for vortices in nanostructured superconductors," *Physica C: Superconductivity*, vol. 470, no. 19, pp. 722 – 725, 2010.

[86] Q. Lu, C. J. O. Reichhardt, and C. Reichhardt, "Reversible vortex ratchet effects and ordering in superconductors with simple asymmetric potential arrays," *Physical Review B*, vol. 75, p. 054502, Feb 2007.

[87] C.-S. Lee, B. Janko, I. Derenyi, and A.-L. Barabasi, "Reducing vortex density in superconductors using the 'ratchet effect'," *Nature*, vol. 400, pp. 337–340, July 1999.

[88] C. Reichhardt and C. J. Olson Reichhardt, "Absolute transverse mobility and ratchet effect on periodic two-dimensional symmetric substrates," *Physical Review E*, vol. 68, p. 046102, Oct 2003.

[89] C. Olson Reichhardt and C. Reichhardt, "Rectification and flux reversals for vortices interacting with triangular traps," *Physica C: Superconductivity*, vol. 432, p. 125, 2005.

[90] E. M. Gonzalez, N. O. Nunez, J. V. Anguita, and J. L. Vicent, "Transverse rectification in superconducting thin films with arrays of asymmetric defects," *Applied Physics Letters*, vol. 91, p. 062505, Aug. 2007.

[91] A. V. Silhanek, J. Van de Vondel, V. V. Moshchalkov, A. Leo, V. Metlushko, B. Ilic, V. R. Misko, and F. M. Peeters, "Comment on "Transverse rectification in superconducting thin films with arrays of asymmetric defects" [Appl. Phys. Lett. 91, 062505 (2007)]," *Applied Physics Letters*, vol. 92, p. 176101, May 2008.

[92] R. Besseling, N. Kokubo, and P. H. Kes, "Dynamic melting of confined vortex matter," *Physical Review Letters*, vol. 91, p. 177002, Oct 2003.

[93] A. Pruymboom, P. H. Kes, E. van der Drift, and S. Radelaar, "Flux-line shear through narrow constraints in superconducting films," *Physical Review Letters*, vol. 60, pp. 1430–1433, Apr 1988.

[94] N. Kokubo, R. Besseling, V. M. Vinokur, and P. H. Kes, "Mode locking of vortex matter driven through mesoscopic channels," *Physical Review Letters*, vol. 88, p. 247004, Jun 2002.

[95] H. Träuble and U. Essmann, "Ein hochauflösendes verfahren zur untersuchung magnetischer strukturen von supraleitern," *physica status solidi (b)*, vol. 18, no. 2, p. 813, 1966.

[96] U. Essmann and H. Träuble, "The direct observation of individual flux lines in type II superconductors," *Physics Letters A*, vol. 24, no. 10, pp. 526 – 527, 1967.

[97] K. Harada, T. Matsuda, J. Bonevich, M. Igarashi, S. Kondo, G. Pozzi, U. Kawabe, and A. Tonomura, "Real-time observation of vortex lattices in a superconductor by electron microscopy," *Nature*, vol. 360, pp. 51–53, Nov. 1992.

[98] I. V. Grigorieva, "Magnetic flux decoration of type-II superconductors," *Superconductor Science and Technology*, vol. 7, pp. 161–176, Apr. 1994.

[99] A. K. Geim, I. V. Grigorieva, and S. V. Dubonos, "Collective effects in vortex movements in type-II superconductors observed by a method for the registration of individual vortices," *Physical Review B*, vol. 46, pp. 324–330, Jul 1992.

[100] M. Machida and H. Kaburaki, "Direct simulation of the time-dependent Ginzburg-Landau equation for type-II superconducting thin film: Vortex dynamics and v - i characteristics," *Physical Review Letters*, vol. 71, pp. 3206–3209, Nov 1993.

[101] J. M. Haile, *Molecular dynamics simulation, elementary methods*. John Wiley & Sons, 1992.

[102] M. P. Allen, "Introduction to molecular dynamics simulation," *NIC Series Volume 23:Computational Soft Matter: From Synthetic Polymers to Proteins*, vol. 23, p. 1, 2004.

[103] E. M. Purcell, "Life at low Reynolds number," *American Journal of Physics*, vol. 45, no. 1, pp. 3–11, 1977.

[104] D. W. Braun, G. W. Crabtree, H. G. Kaper, A. E. Koshelev, G. K. Leaf, D. M. Levine, and V. M. Vinokur, "Structure of a moving vortex lattice," *Physical Review Letters*, vol. 76, pp. 831–834, Jan. 1996.

[105] W. D. Gropp, H. G. Kaper, G. K. Leaf, D. M. Levine, M. Palumbo, and V. M. Vinokur, "Numerical simulation of vortex fynamics in type-II

superconductors," *Journal of Computational Physics*, vol. 123, pp. 254–266, Feb. 1996.

[106] I. S. Aranson, S. Scheidl, and V. M. Vinokur, "Nonequilibrium dislocation dynamics and instability of driven vortex lattices in two dimensions," *Physical Review B*, vol. 58, pp. 14541–14547, Dec. 1998.

[107] J. R. Clem, "Two-dimensional vortices in a stack of thin superconducting films: A model for high-temperature superconducting multilayers," *Physical Review B*, vol. 43, pp. 7837–7846, Apr. 1991.

[108] S. Ryu and D. Stroud, "First-order melting and dynamics of flux lines in a model for $YBa_2Cu_3O_{7-\delta}$," *Physical Review B*, vol. 54, pp. 1320–1333, July 1996.

[109] C. J. Olson, C. Reichhardt, and F. Nori, "Fractal networks, braiding channels, and voltage noise in intermittently flowing rivers of quantized magnetic flux," *Physical Review Letters*, vol. 80, pp. 2197–2200, Mar. 1998.

[110] J. Bardeen and M. J. Stephen, "Theory of the motion of mortices in superconductors," *Physical Review*, vol. 140, pp. A1197–A1207, Nov. 1965.

[111] M. N. Kunchur, D. K. Christen, and J. M. Phillips, "Observation of free flux flow at high dissipation levels in $YBa_2Cu_3O_{7-\delta}$ epitaxial films," *Physical Review Letters*, vol. 70, pp. 998–1001, Feb. 1993.

[112] V. Misko, N. Lin, and F. Peeters, "Unconventional dynamics of vortex shells in mesoscopic superconducting corbino disks," *Physica C: Superconductivity*, vol. 470, pp. 939 – 941, Mar 2010.

[113] N. S. Lin, V. R. Misko, and F. M. Peeters, "Dynamics of multishell vortex structures in mesoscopic superconducting Corbino disks," *Physical Review B*, vol. 81, p. 134504, Apr. 2010.

[114] D. E. Fujibayashi and M. Kato, "Vortex dynamics in Corbino disks: Molecular dynamics simulation with thermal effect," *Physica C: Superconductivity*, Mar. 2012. http://dx.doi.org/10.1016/j.physc.2012.03.022.

[115] W. V. Pogosov, V. R. Misko, H. J. Zhao, and F. M. Peeters, "Collective vortex phases in periodic plus random pinning potential," *Physical Review B*, vol. 79, p. 014504, Jan. 2009.

[116] W. V. Pogosov, H. J. Zhao, V. R. Misko, and F. M. Peeters, "Kink-antikink vortex transfer in periodic-plus-random pinning potential: Theoretical analysis and numerical experiments," *Physical Review B*, vol. 81, p. 024513, Jan. 2010.

[117] P. A. Venegas and E. Sardella, "Vortex lattice and matching fields for a long superconducting wire," *Physical Review B*, vol. 58, pp. 5789–5794, Sept. 1998.

[118] V. A. Schweigert, F. M. Peeters, and P. Singha Deo, "Vortex phase diagram for mesoscopic superconducting disks," *Physical Review Letters*, vol. 81, pp. 2783–2786, Sept. 1998.

[119] K. Harada, O. Kamimura, H. Kasai, T. Matsuda, A. Tonomura, and V. V. Moshchalkov, "Direct observation of vortex dynamics in superconducting films with regular arrays of defects," *Science*, vol. 274, pp. 1167–1170, Nov. 1996.

[120] T. Sasagawa, Y. Togawa, J. Shimoyama, A. Kapitulnik, K. Kitazawa, and K. Kishio, "Magnetization and resistivity measurements of the first-order vortex phase transition in $(La_{1-x}Sr_x)_2CuO_4$," *Physical Review B*, vol. 61, pp. 1610–1617, Jan. 2000.

[121] M. Kong, B. Partoens, and F. M. Peeters, "Transition between ground state and metastable states in classical two-dimensional atoms," *Physical Review E*, vol. 65, p. 046602, Mar. 2002.

[122] V. A. Schweigert and F. M. Peeters, "Spectral properties of classical two-dimensional clusters," *Physical Review B*, vol. 51, pp. 7700–7713, Mar. 1995.

[123] M. Kong, B. Partoens, and F. M. Peeters, "Topological defects and nonhomogeneous melting of large two-dimensional Coulomb clusters," *Physical Review E*, vol. 67, p. 021608, Feb. 2003.

[124] L. J. Campbell and R. M. Ziff, "Vortex patterns and energies in a rotating superfluid," *Physical Review B*, vol. 20, pp. 1886–1902, Sept. 1979.

[125] N. S. Lin, T. W. Heitmann, K. Yu, B. L. T. Plourde, and V. R. Misko, "Rectification of vortex motion in a circular ratchet channel," *Phys. Rev. B*, vol. 84, p. 144511, Oct 2011.

[126] N. Lin, V. Misko, T. Heitmann, K. Yu, and B. Plourde, "Density dependence of the rectification of vortex motion in a circular asymmetric channel," *Physica C: Superconductivity*, vol. 479, p. 137, Dec 2012. http://dx.doi.org/10.1016/j.physc.2011.12.028.

[127] D. Babić, J. Bentner, C. Sürgers, and C. Strunk, "Flux-flow instabilities in amorphous $Nb_{0.7}Ge_{0.3}$ microbridges," *Physical Review B*, vol. 69, p. 092510, Mar 2004.

[128] A. I. Larkin and Y. N. Ovchinnikov, "Nonlinear conductivity of superconductors in the mixed state," *Zh. Eksp. Teor. Fiz.*, vol. 68, p. 1915, 1975.

[129] W. Klein, R. P. Huebener, S. Gauss, and J. Parisi, "Nonlinearity in the flux-flow behavior of thin-film superconductors," *Journal of Low Temperature Physics*, vol. 61, no. 5, pp. 413–432, 1985.

[130] T. W. Heitmann, K. Yu, C. Song, M. P. DeFeo, B. L. T. Plourde, M. B. S. Hesselberth, and P. H. Kes, "Picovoltmeter for probing vortex dynamics in a single weak-pinning Corbino channel," *The Review of scientific instruments*, vol. 79, p. 103906, Oct. 2008.

[131] J. von Delft and R. Poghossian, "Algebraic Bethe ansatz for a discrete-state BCS pairing model," *Physical Review B*, vol. 66, p. 134502, Oct 2002.

[132] V. N. Gladilin, J. Tempere, I. F. Silvera, and J. T. Devreese, "Critical temperature and specific heat for Cooper pairing on a spherical surface," *Physical Review B*, vol. 74, p. 104512, Sep 2006.

[133] E. A. Yuzbashyan, A. A. Baytin, and B. L. Altshuler, "Finite-size corrections for the pairing hamiltonian," *Physical Review B*, vol. 71, p. 094505, Mar 2005.

[134] N. Sandulescu, B. Errea, and J. Dukelsky, "Isovector neutron-proton pairing with particle number projected BCS," *Physical Review C*, vol. 80, p. 044335, Oct 2009.

[135] L. Amico and A. Osterloh, "Exact correlation functions of the BCS model in the canonical ensemble," *Physical Review Letters*, vol. 88, p. 127003, Mar 2002.

[136] H.-Q. Zhou, J. Links, R. H. McKenzie, and M. D. Gould, "Superconducting correlations in metallic nanoparticles: exact solution of the BCS model by the algebraic Bethe ansatz," *Physical Review B*, vol. 65, p. 060502(R), Jan 2002.

[137] G. Gorohovsky and E. Bettelheim, "Exact expectation values within Richardson's approach for the pairing Hamiltonian in a macroscopic system," *Physical Review B*, vol. 84, p. 224503, Dec. 2011.

[138] W. V. Pogosov, N. S. Lin, and V. R. Misko, "Analytical approach to the Richardson model using the electron-hole symmetry of paring Hamiltonian," *Phys. Rev. B*, 2012. Submitted.

[139] W. V. Pogosov, "'probabilistic' approach to Richardson equations," *Journal of physics. Condensed matter : an Institute of Physics journal*, vol. 24, p. 075701, Feb. 2012.

[140] A. Faribault, P. Calabrese, and J.-S. Caux, "Bethe ansatz approach to quench dynamics in the Richardson model," *Journal of Mathematical Physics*, vol. 50, no. 9, p. 095212, 2009.

[141] S. Rombouts, D. Van Neck, and J. Dukelsky, "Solving the Richardson equations for fermions," *Physical Review C*, vol. 69, p. 061303, Jun 2004.

[142] F. Domínguez, C. Esebbag, and J. Dukelsky, "Solving the Richardson equations close to the critical points," *Journal of Physics A: Mathematical and General*, vol. 39, pp. 11349–11360, Sept. 2006.

[143] M. Sambataro, "Pair condensation in a finite Fermi system," *Physical Review C*, vol. 75, p. 054314, May 2007.

[144] J. M. Román, G. Sierra, and J. Dukelsky, "Elementary excitations of the BCS model in the canonical ensemble," *Physical Review B*, vol. 67, p. 064510, Feb 2003.

[145] W. Pogosov and M. Combescot, ""Moth-eaten effect" driven by Pauli blocking, revealed for Cooper pairs," *JETP Letters*, vol. 92, p. 534, 2010.

[146] M. Crouzeix and M. Combescot, "Energy of N Cooper pairs by analytically solving the Richardson-Gaudin equations for conventional superconductors," *Physical Review Letters*, vol. 107, p. 267001, Dec 2011.

Nansheng Lin

Curriculum Vitae

✉ Email: phy.nslin@gmail.com
Born in Rui'an,
Zhejiang Prov., China
on Feb. 21*th*, 1983

Education

Universiteit Antwerpen — **Antwerpen, Belgium**
Ph. Doctor, Research area: Superconductors — *2008–2012*

Universiteit Antwerpen — **Antwerpen, Belgium**
Advanced Master, Major: Nanophysics (Great distribution) — *2007–2008*

Zhejiang University — **Hangzhou, China**
Bachelor of Science, Major: Physics — *2003–2007*

Skills

- Numerical Approaches: Molecular Dynamics, Monte Carlo
- Computing Environments: Windows, Linux/Unix
- Programming Languages: Fortran, C/C++, CUDA
- Graphic Softwares: Origin, Gnuplot, CorelDraw, Photoshop
- Miscellaneous: Bash, Make, Expect

Awards

Apr. 2010: The Belgian Physical Society (BPS) Prize for One of the Best Three Physics Master's Thesis

Proceedings & Activities

Sep. 2008: Joint ESF and JSPS workshop on Nanostructured Superconductors: From Fundamentals to Applications.

Dynamics of Vortex Shells in Mesoscopic Superconducting Corbino Disks (Invited talk).

V.R. Misko, N.S. Lin, and F.M. Peeters. Freudenstadt-Lauterbad,Germany

Mar. 2009: The 2009 March Meeting of the American Physical Society (APS).

Unconventional Vortex Dynamics in Mesoscopic Superconducting Corbino Disks (Talk).

V.R. Misko, N.S. Lin, and F.M. Peeters. Pittsburgh, Pennsylvania, USA

Apr. 2009*: The General Scientific Meeting of the Belgian Physical Society & Belgian Biophysical

Society.

The dynamics of vortex shells in mesoscopic superconducting Corbino disks (Poster).

N.S. Lin, V.R. Misko, and F.M. Peeters. Hasselt, Belgium

Sep. 2009*: The 32nd International Symposium on Dynamical Properties of Solids (DyProSo XXXII).

The dynamics of vortex shells in mesoscopic superconducting Corbino disks (Poster).

N.S. Lin, V.R. Misko, and F.M. Peeters. Antwerpen, Belgium

Sep. 2009: The 12th International Workshop on Vortex Matter in Superconductors.

Unconventional vortex dynamics in mesoscopic superconducting Corbino disks(Invited presentation[Talk & Poster]).

V.R. Misko, N.S. Lin, and F.M. Peeters. Lake Yamanaka, Yamanashi, Japan

Sep. 2009: The 6th International Conference in School Format on "Vortex Matter in Nanostructured Superconductors".

Unconventional vortex dynamics in mesoscopic superconducting Corbino disks (Poster).

V.R. Misko, N.S. Lin, and F.M. Peeters. Rhodes, Greece

Mar. 2010: The 2010 March Meeting of the American Physical Society (APS).

The Dynamics of Multi-Shell Vortex Matter in Mesoscopic Superconducting Corbino Disks (Talk).

V.R. Misko, N.S. Lin, and F.M. Peeters. Portland, Oregon, USA

Apr. 2010*: The Belgian Physical Society & Nederlandse Natuurkendige Vereniging joint conference "Fysica 2010".

Commensurability effects and compression-decompression wave motion of vortices in mesocscopic superconducting Corbino disks (Poster).

N.S. Lin, V.R. Misko, and F.M. Peeter Utrecht, Netherlands

Aug. 2011: The 13th International Workshop on Vortex Matter in Superconductors (Vortex 2011).

Rectification of vortex motion in a circular ratchet channel (Invited Poster).

V.R. Misko, N.S. Lin, T.W. Heitman, K. Yu, and B.L.T. Plourde Chicago, Illinois, USA

Sep. 2011*: Seventh International Conference on Vortex Matter in Nanostructured Superconductors (Vortex VII).

The dynamics of vortex "shells" in circular channels in macroscopic Corbino disks (Poster).

N.S. Lin and V.R. Misko Rhodes, Greece

* Indicated the conferences that I attended and also gave the poster presentation.

Publications

N. S. Lin, V. R. Misko, and F. M. Peeters. Unconventional vortex dynamics in mesoscopic superconducting Corbino disks. *Phys. Rev. Lett.*, 102:197003, May 2009.

V.R. Misko, N.S. Lin, and F.M. Peeters. Unconventional dynamics of vortex shells in mesoscopic superconducting Corbino disks. *Physica C: Superconductivity*, 470:939, Mar 2010.

N. S. Lin, V. R. Misko, and F. M. Peeters. Dynamics of multishell vortex structures in mesoscopic superconducting Corbino disks. *Phys. Rev. B*, 81:134504, Apr 2010.

N. S. Lin, V. R. Misko, and F. M. Peeters. Dynamics of vortex shells in mesoscopic superconducting Corbino disks. *BPhy*, 2-2010:23, 2010.

N. S. Lin, T. W. Heitmann, K. Yu, B. L. T. Plourde, and V. R. Misko. Rectification of vortex motion in a circular ratchet channel. *Phys. Rev. B*, 84:144511, Oct 2011.

N.S. Lin, V.R. Misko, T.W. Heitmann, K. Yu, and B.L.T. Plourde. Density dependence of the rectification of vortex motion in a circular asymmetric channel. *Physica C: Superconductivity*, 479:137, Sep 2012.

W. V. Pogosov, N. S. Lin, and V. R. Misko. Analytical approach to the Richardson model using the electron-hole symmetry of paring Hamiltonian. *Submitted to Phys. Rev. B*, 2012.